

University of Windsor

Scholarship at UWindor

Electronic Theses and Dissertations

Theses, Dissertations, and Major Papers

11-7-2015

Development of a Tensile Split Hopkinson Pressure Bar Testing Facility

Kevin Young
University of Windsor

Follow this and additional works at: <https://scholar.uwindsor.ca/etd>

Recommended Citation

Young, Kevin, "Development of a Tensile Split Hopkinson Pressure Bar Testing Facility" (2015). *Electronic Theses and Dissertations*. 5513.

<https://scholar.uwindsor.ca/etd/5513>

This online database contains the full-text of PhD dissertations and Masters' theses of University of Windsor students from 1954 forward. These documents are made available for personal study and research purposes only, in accordance with the Canadian Copyright Act and the Creative Commons license—CC BY-NC-ND (Attribution, Non-Commercial, No Derivative Works). Under this license, works must always be attributed to the copyright holder (original author), cannot be used for any commercial purposes, and may not be altered. Any other use would require the permission of the copyright holder. Students may inquire about withdrawing their dissertation and/or thesis from this database. For additional inquiries, please contact the repository administrator via email (scholarship@uwindsor.ca) or by telephone at 519-253-3000ext. 3208.

Development of a Tensile Split Hopkinson Pressure Bar Testing Facility

By

Kevin Young

A Thesis

Submitted to the Faculty of Graduate Studies

through the Department of Mechanical, Automotive and Materials Engineering

in Partial Fulfillment of the Requirements for

the Degree of Master of Applied Science

at the University of Windsor

Windsor, Ontario, Canada

2015

© 2015 Kevin Young

Development of a Tensile Split Hopkinson Pressure Bar Testing Facility

by

Kevin Young

APPROVED BY:

A. Alpas
Mechanical, Automotive, & Materials Engineering

W. Altenhof
Mechanical, Automotive, & Materials Engineering

D. Green, Advisor
Mechanical, Automotive, & Materials Engineering

August 4, 2015

Declaration of Originality

I hereby certify that I am the sole author of this thesis and that no part of this thesis has been published or submitted for publication.

I certify that, to the best of my knowledge, my thesis does not infringe upon anyone's copyright nor violate any proprietary rights and that any ideas, techniques, quotations, or any other material from the work of other people included in my thesis, published or otherwise, are fully acknowledged in accordance with the standard referencing practices. Furthermore, to the extent that I have included copyrighted material that surpasses the bounds of fair dealing within the meaning of the Canada Copyright Act, I certify that I have obtained a written permission from the copyright owner(s) to include such material(s) in my thesis and have included copies of such copyright clearances to my appendix.

I declare that this is a true copy of my thesis, including any final revisions, as approved by my thesis committee and the Graduate Studies office, and that this thesis has not been submitted for a higher degree to any other University or Institution.

Abstract

This project consisted of designing and developing a split Hopkinson pressure bar (SHPB) apparatus to perform tensile tests on metallic sheet materials at strain rates from 500 s^{-1} to 2000 s^{-1} .

The mechanical components that were designed and built are: a gas gun, incident/transmission bars and a momentum trap. A data acquisition system with two data acquisition cards with a maximum sampling rate of up to 60 MS/s was used. This apparatus was successfully assembled, calibrated and tested. A software code was developed to post-process the experimental strain data and determine the corresponding flow curves.

The accuracy of this tensile SHPB apparatus was demonstrated by testing DP600 sheet steel specimens in the rolling, diagonal and transverse directions. When compared to published data for the same sheet material tested in a different laboratory, the overall errors were found to be 3.20%, 4.05%, and 3.87% for the rolling, diagonal and transverse directions, respectively.

Acknowledgements

I would like to thank Dr. Daniel Green for his continued support and guidance in completing this project. He is a great professor to have as an advisor and mentor throughout my education at the University of Windsor.

I would like to thank the members of my committee Dr. Ahmet Alpas and Dr. William Altenhof for their suggestions and feedback throughout this project. Dr. William Altenhof was helpful throughout the programming of the data acquisition system.

This project would not have been possible without the help and expertise of the technicians Andy Jenner and Patrick Seguin. Both technicians were very accommodating and generous with helping me when I was stuck. Andy was very helpful to discuss ideas about design and manufacturability of the components for this projects tensile SHPB apparatus. His time involved in manufacturing most of the pieces for this project is numerous and greatly appreciated. Without Patrick the instrumentation would be much more costly and would have taken much more time to implement. His vast knowledge in instrumentation is an invaluable resource to the Engineering department.

The previous work of Luigi Zanettin from our capstone project was greatly appreciated in helping this project move along to a successful completion.

Table of Contents

Declaration of Originality	iii
Abstract.....	iv
Acknowledgements.....	v
List of Tables	viii
List of Figures	ix
List of Symbols	xii
Chapter 1: Introduction	1
1.1 Background	1
1.2 Objectives of Project.....	2
1.3 Outline of the thesis.....	3
Chapter 2: Literature Review	4
2.1 Overview of high strain rate testing	4
2.2 SHPB Apparatus	4
2.2.1 History of the Hopkinson Pressure Bar	4
2.2.2 Compression SHPB.....	7
2.2.3 Types of Tensile SHPB	8
2.2.4 The development of direct acting tensile SHBP apparatus.	10
2.2.5 Exploring Other Tensile SHPB Apparatus Facilities	12
2.3 SHPB Theory.....	12
2.3.1 Stress waves in cylindrical bars.....	13
2.3.2 SHPB equations.....	13
2.3.3 SHPB Theory using Conservation of Energy.....	17
2.3.4 Striker Velocity.....	20
Chapter 3: Design, Construction, and Assembly of SHPB	23
3.1 Overview of a Tensile Split Hopkinson Pressure Bar Apparatus.....	23
3.2 Mechanical Components	24
3.2.1 Support Frame	24
3.2.2 Bar Holders.....	26
3.2.3 Striker and Bars.....	28

3.2.4 Gas gun.....	33
3.2.5 Momentum trap	39
3.2.6 Specimen design	40
3.2.7 Assembly and set-up mechanical components	42
3.3 Instrumentation	44
3.3.1 Strain gauges.....	44
3.3.2 Pressure Transducer	45
3.3.3 Striker Velocity.....	46
3.3.4 Start data acquisition signal.....	46
3.3.5 Data acquisition	47
3.3.6 Assembly and set-up electrical components	49
Chapter 4: Calibration, Operation and Data Analysis of a SHPB.....	53
4.1 Calibration of the gas guns velocity versus pressure.....	53
4.2 Calibration of the strain gauge output	56
4.3 Operating Procedure.....	61
4.4 Signal processing.....	65
Chapter 5: Experimental testing of DP600 Sheet Steel	71
5.1 High strain Rate flow behaviour of DP600 sheet steel	71
5.1.1 Properties of DP600 sheet steel	71
5.1.2 SHPB tests on DP600 sheet steel	72
5.2 Comparison of experimental data to known data.....	82
Chapter 6: Conclusions and Recommendations	87
6.1 Conclusions	87
6.2 Recommendations for further improvement of the SHPB	88
References	90
Appendix A – Durability Calculation of Threads on the Bars	95
Appendix B – Technical Drawings	101
Appendix C – MATLAB Data Processing Program	120
Vita Auctoris.....	127

List of Tables

Table 1: AISI 4140 / ASTM A29 (4140) Elements (ASTM , 2012).....	29
Table 2: Physical Properties of AISI 4140 (MatWeb, 2015)	29
Table 3: Physical Properties of C350 maraging steel (Cardarelli, 2008)	35
Table 4: Physical properties of AISI 304 stainless steel (Cardarelli, 2008)	35
Table 5: Information about the data acquisition cards (National Instruments, 2015).....	48
Table 6: Range and accuracy of the two data acquisition cards (National Instruments, 2015)	49
Table 7: Average striker velocity and firing pressure of the gas gun.....	53
Table 8: Experimental data for calibration of strain gauges.....	59
Table 9: Error and Validation Results.....	61
Table 10: Chemical composition of DP600 steel in weight percent	71
Table 11: Mechanical properties of DP600 steel	72
Table 12: Gas gun pressure and striker velocity data for the RD specimens	76
Table 13: Strain rate for RD specimens.....	76
Table 14: Gas gun pressure and striker velocity data for the DD specimens	78
Table 15: Strain rate for DD specimens	79
Table 16: Gas gun pressure and striker velocity data for the TD specimens.....	81
Table 17: Strain rate for TD specimens.....	81
Table 18: Error and Validation metric for comparing project data to known data	84
Table 19: Error and Validation metric for comparing ArcelorMittal data to project data	86

List of Figures

Figure 1: Global formability diagram (WorldAutoSteel, 2014).....	2
Figure 2: Bertram Hopkinson’s experiment to measure pressure waves (Chen & Song, 2011)	5
Figure 3: General arrangement of Davies’ apparatus (Davies R. M., 1948).	6
Figure 4: Typical layout and major components of a compression SHPB apparatus (Chen & Song, 2011)	7
Figure 5: Direct acting tension loading (Hauser, 1966)	8
Figure 6: Top hat specimen configuration (Lindholm & Yeakley, 1968).....	9
Figure 7: Nicholas experimental setup. (Nicholas, 1981)	10
Figure 8: Static loading tensile SHPB (Ohio State University).....	11
Figure 9: Layout of a dynamic loading tensile SHPB apparatus (Hasenpouth, 2010).....	11
Figure 10: X-t diagram of stress wave propagation in a tensile SHPB apparatus.....	14
Figure 11: Variables at the specimen.....	15
Figure 12: Mechanical components of tensile SHPB	23
Figure 13: Support frame for SHPB apparatus.....	24
Figure 14: Vertical support (Zanettin, Young, & Hussain, 2012)	25
Figure 15: Horizontal support bar (Zanettin, Young, & Hussain, 2012).....	25
Figure 16: Exploded view of SHPB bar holder (Zanettin, Young, & Hussain, 2012).....	26
Figure 17: Bar holder showing adjustability (Zanettin, Young, & Hussain, 2012)	27
Figure 18: Bar holder clamped to support frame.	28
Figure 19: Striker.....	29
Figure 20: Close up view of the bar and anvil attached.....	30
Figure 21: Close up view of the threads on the bar.....	31
Figure 22: Slot in bars to hold test specimen	31
Figure 23: Specimen showing serrations from specimen slot in bars	32
Figure 24: Anvil showing threading	33
Figure 25: Velocity of striker for various barrel lengths	34
Figure 26: Gas gun pressure chamber	36
Figure 27: Gas gun cross section.....	36
Figure 28: Valve assembly for gas gun.....	38
Figure 29: Momentum trap assembly	39

Figure 30: V groove in momentum trap base.....	40
Figure 31: University of Waterloo specimen design (Smerd, Winkler, Salisbury, Worswick, Lloyd, & Finn, 2005).....	41
Figure 32: University of Waterloo specimen design modified to fit the new SHPB apparatus	41
Figure 33: Gas gun showing which mount is attached with shoulder bolts to I-beam	42
Figure 34: Aligning incident bar to gun barrel centre axis by measuring at different points	43
Figure 35: Strain gauges wired into the Wheatstone bridge (Kyowa, 2015).....	45
Figure 36: Micro-switch location on SHPB apparatus.....	47
Figure 37: National Instruments data acquisition system	48
Figure 38: Computer cabinet for storing DAQ system.....	50
Figure 39: Strain gauge wrapped with electrical tape	50
Figure 40: Valve configuration on gas gun.....	51
Figure 41: Optical gate to measure striker velocity.....	51
Figure 42: Velocity of striker vs. firing pressure of gas gun	54
Figure 43: Pressure of gas gun vs. velocity of striker.....	55
Figure 44: Path for strain gauge signal	56
Figure 45: MTS tester applying a load on the LC305 load cell	57
Figure 46: Load cell placement for calibrating strain gauges	58
Figure 47: Set up of jack screw used to apply a compressive load on the bars for calibration of strain gauges	58
Figure 48: Voltage out of Wheatstone bridge vs. applied load for load cell #3	60
Figure 49: Alignment of incident anvil and optical gate housing	62
Figure 50: Valve actuator connection and fill selection valves.....	63
Figure 51: Valve pneumatic actuator controller	64
Figure 52: Example of initial strain vs. count graph for the incident and transmission bars	65
Figure 53: 250 kHz, 2nd order lowpass filter	66
Figure 54: 250 kHz, 6th order lowpass filter	67
Figure 55: Unfiltered and filtered transmission bar strain gauge output.....	67
Figure 56: alignment of the incident and reflected pulses	68
Figure 57: Engineering stress versus strain for uniform and average strain	69
Figure 58: Example of the true stress-strain versus engineering stress-strain.....	70
Figure 59: Uniaxial tension test data for DP600 steel	72

Figure 60: Mounted specimen with black marker at bar/specimen interface to show if slipping occurs.....	73
Figure 61: Fractured SHPB specimen with marker at bar/specimen interface showing no slipping	74
Figure 62: RD fracture location	75
Figure 63: Bent test specimen from transmission bar collision.....	75
Figure 64: True Stress vs. True Strain curves for all SHPB specimen tested in the RD	77
Figure 65: Central fracture location for DD specimens	78
Figure 66: Sample specimen showing evidence of slipping in bar specimen slot	80
Figure 67: Central fracture location for TD specimens	80
Figure 68: Comparison of the true stress vs. true strain data in the RD obtained from two different laboratories.....	83
Figure 69: Comparison of the true stress vs. true strain data in the DD obtained from two different laboratories.....	83
Figure 70: Comparison of the true stress vs. true strain data in the TD obtained from two different laboratories.....	84
Figure 71: Comparison of ArcelorMittal and project data.....	85
Figure 72: Yield Strength versus Hardness Rockwell C	96
Figure 73: Unified Thread Standard profile dimensions.....	97
Figure 74: Triangle Used to calculate X, the half-distance through the thread.....	98
Figure 75: S-N Curve for 4140 steel (Boyer, 2006)	100

List of Symbols

A_B	Cross-sectional area of the bar
A_S	Cross-sectional area of the specimen
A_{st}	Cross-sectional area of the striker
A_{thread}	Area of the threads experiencing a shearing force
C	Factor depending on method of attachment for ASME pressure vessel
C_B	Speed of sound in the bar material
C_{st}	Speed of sound in the striker material
C_t	Circumference of the minor diameter of the thread
D	Distance between optical sensors
D_p	Diameter of projectile
D_{maj}	Major diameter of the thread
D_{min}	Minor diameter of the thread
E_B	Young's modulus of the bar
EM	Average Error
F_i	Force on incident bar
F_{st}	Force on striker
GF	Gauge factor of the strain gauges
H	Height between the theoretical peaks of the internal and external threads
J	Joint efficiency
KE_i	Kinetic energy, from incident pulse
KE_R	Kinetic energy, from reflected pulse
KE_T	Kinetic energy, from transmitted pulse

L_{bar}	Length of gun barrel
L_s	Gauge length of the specimen
L_{st}	Length of the striker
P	Pressure of the gas reservoir
R	Inside radius of cylinder
S	Allowable stress from ASME boiler and pressure vessel code
U_i	Elastic strain energy, incident pulse
U_r	Elastic strain energy, reflected pulse
U_t	Elastic strain energy, transmitted pulse
U_s	Elastic strain energy, specimen
V_i	Deformed volume in the incident bar
V_{out}	Output voltage of the Wheatstone bridge
V_{ex}	Excitation voltage of the Wheatstone bridge
VM	Validation Metric
d	Bolt circle diameter
m	Mass
t	Time
t_c	Thickness of thick-wall cylinder of gas gun
t_{ec}	Thickness of the end cap of gas gun
v_1	Velocity of the incident bar specimen face
v_2	Velocity of the transmission bar specimen face
v_i	Velocity of the incident bar
v_{st}	Velocity of the striker

ε	Strain
$\bar{\varepsilon}$	Average engineering strain
$\dot{\bar{\varepsilon}}$	Average engineering strain rate
$\dot{\varepsilon}_u$	Uniform engineering strain rate
ε_u	Uniform engineering strain
ε_i	Incident strain pulse
ε_R	Reflected strain pulse
ε_T	Transmitted strain pulse
ε_{ps}	Plastic strain in the specimen
ε_{true}	True strain
ρ_B	Density of the bar material
ρ_{st}	Density of the striker
ρ_P	Density of the projectile
σ	Normal stress
σ_1	Stress at the incident bar specimen face
σ_2	Stress at the transmission bar specimen face
σ_i	Stress in incident bar
σ_u	Uniform engineering stress
$\bar{\sigma}$	Average engineering stress
σ_s	Yield strength of the specimen
σ_{st}	Stress in the striker
σ_{true}	True stress
δ_{es}	Deformation of the specimen by elastic strain energy
δ_{KES}	Deformation of the specimen by kinetic energy

τ_{thread}

Shear stress in the thread

Chapter 1: Introduction

1.1 Background

Advanced high strength steels have become a material of choice for the body-in-white and structure of vehicles as the automotive industry endeavours to reduce weight and increase vehicle safety. The use of advanced high strength steels (AHSS) sheets allows the automotive industry to produce thinner body components, which lowers the vehicle weight. To further reduce automobile weight computer simulations are carried out to predict the outcome of automobile crash events, and simulation results can be used to either reduce the thickness of stamped components, select stronger materials or optimize the design of the structure.

In these numerical simulation codes, the constitutive models for the materials that make up the body and structure of the vehicle must take into account how the materials behave at different strain rates. A “nominal strain rate of 100/s is often used to characterize overall automobile crash events, whereas strain rates on the order of 1000/s can occur locally” (Salisbury, Worswick, & Mayer, 2006). The constitutive models must be able to accurately predict how steel “becomes stronger on impact, allowing the steel to absorb more energy” (WorldAutoSteel, 2015).

Automotive vehicle structures are “commonly manufactured by stamping operations and experience much lower rates of strain prior to in-service crash events” (Rahmaan, Bardelcik, Imbert, Butcher, & Worswick, 2014). Figure 1 shows the global formability diagram; with the increase in strength of the material the percent elongation tends to decrease, which means the ductility of the material decreases. Therefore “AHSS products have significantly different forming characteristics and these challenge conventional mechanical and hydraulic press forming” (WorldAutoSteel, 2014).

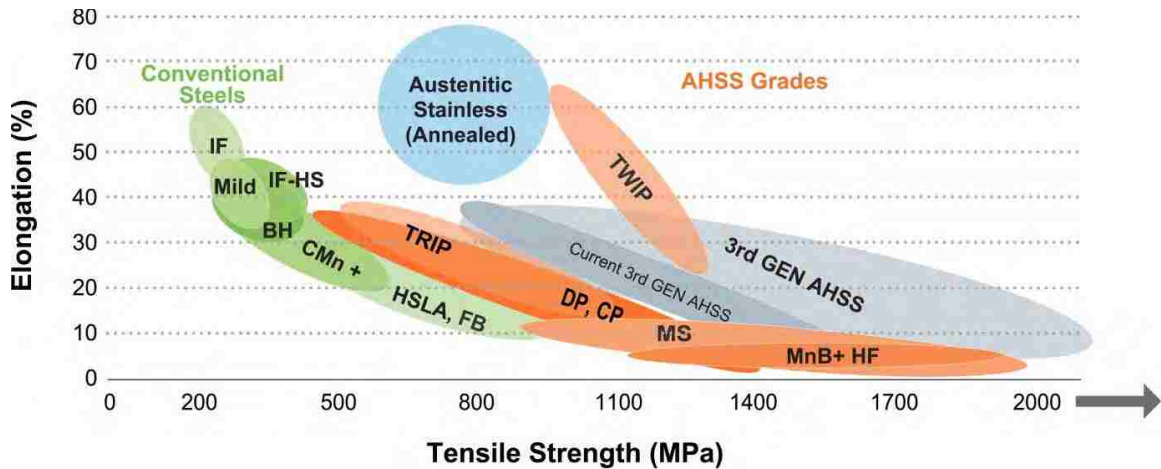


Figure 1: Global formability diagram (WorldAutoSteel, 2014)

In view of the need to compromise between strength and ductility for sheet materials shaped by conventional forming processes, the pursuit of vehicle weight reduction poses a challenge to designers seeking to create complex part shapes. This challenge has spurred researchers to develop novel forming processes, such as high temperature forming or high strain rate forming. One of the most promising of these new technologies is electrohydraulic forming, which is a “pulsed forming process that uses the discharge of electrical energy across electrodes submerged in a fluid to generate a pressure pulse that forms the work piece” (Maris, 2014).

In order to obtain the mechanical properties and work hardening behaviour of these AHSS materials at different strain rates various types of tests can be performed.

1.2 Objectives of Project

The main objective of this project is to develop a tensile SHPB apparatus to perform high strain rate testing of sheet materials. This development work includes the following tasks:

- Design and fabricate the mechanical components of the tensile SHPB apparatus,
- Assemble the SHPB apparatus hardware with the required instrumentation and data acquisition system,

- Develop a LabVIEW virtual instrument to communicate with the various data acquisition cards,
- Develop a MATLAB code to post-process the experimental data and determine the stress-strain curve for a given test,
- Demonstrate the functionality and accuracy of the tensile SHPB apparatus by performing tests for a particular DP600 sheet steel and compare the stress-strain results with those obtained for the same sheet material from the tensile SHPB in a different laboratory.

1.3 Outline of the thesis

Before designing and constructing specialized testing equipment such as a SHPB apparatus, it is essential to review the existing literature on the subject; this literature review will be presented in chapter 2 of the thesis. An in depth description of the SHPB apparatus mechanical components and instrumentation, along with how these components are all assembled into a functional SHPB apparatus will be presented in chapter 3 of the thesis. In order for the SHPB apparatus to be useful, calibration of the gas gun pressure to striker velocity and calibration of the strain gauges are required along with the procedures for operating the SHPB apparatus and processing the data from it. These topics are presented in chapter 4 of the thesis. To demonstrate the functionality of the tensile SHPB apparatus, SHPB specimens were tested and the stress-strain curves were obtained. These flow curves were compared to published results obtained from world-class laboratories for the same material. These comparisons are presented in chapter 5 of the thesis. Finally, the conclusions and future recommendations are presented in chapter 6 of the thesis.

Chapter 2: Literature Review

2.1 Overview of high strain rate testing

Engineers often need to know how materials will react to loading applied at different strain rates and therefore different testing devices have been developed to measure the material response at high strain rates. Servo-hydraulic testing frames can be used to apply strain rates up to about 100 s^{-1} . The Split Hopkinson Pressure Bar (SHPB) apparatus is generally used for material testing at strain rates between 100 s^{-1} and $10,000 \text{ s}^{-1}$. The SHPB “allows the deformation of a sample of a ductile material at a high strain rate, while maintaining a uniform uniaxial state of stress within the sample” (ASM Handbook , 2000). For strain rate testing above 1000 s^{-1} compression and tension tests differ. The Taylor impact test (ASM Handbook , 2000) is typically used for loading in compression at strain rates up to $100,000 \text{ s}^{-1}$. Expanding ring tests (ASM Handbook , 2000) are used for loading in tension at strain rates up to $10,000 \text{ s}^{-1}$ and the flyer plate test is used for strain rates $>100,000 \text{ s}^{-1}$ (ASM Handbook , 2000).

2.2 SHPB Apparatus

2.2.1 History of the Hopkinson Pressure Bar

In 1914, Bertram Hopkinson designed an experiment to measure the pressure wave along a steel rod, when the rod was struck by a bullet or by the detonation of explosives. Hopkinson’s experiment, shown in Figure 2, consisted of a steel rod (rod B) suspended on wires “as a ballistic pendulum” (Hopkinson, 1914), with a small rod (rod C) magnetically attached to the suspended rod with a joint that is perfectly matched.

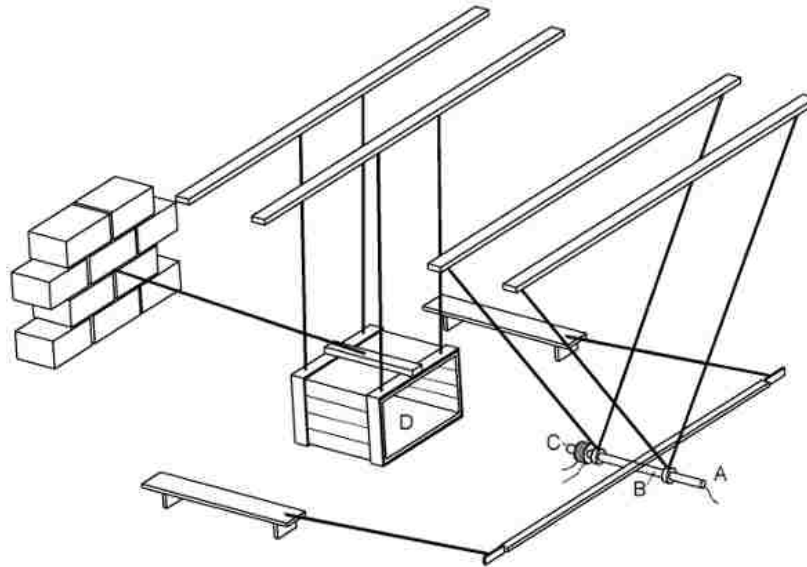


Figure 2: Bertram Hopkinson's experiment to measure pressure waves (Chen & Song, 2011)

Rod B would be struck at point A with a lead bullet or by the pressure wave caused by the detonation of an explosive. When the length of rod C is shorter than half the length of the pressure wave, both rod C and rod B will move apart. When the length of rod C is increased to cause rod B to remain at rest, rod C will be “half the length of the pressure wave” (Hopkinson, 1914). By measuring the momentum of rod C in ballistic pendulum D, “it is possible to measure both the duration of the blow and the maximum pressure developed by it” (Hopkinson, 1914).

Landon and Quinney (1923) continued Hopkinson's work, “in an attempt to interpret the results accumulated before the War, and also some results obtained by Prof. Hopkinson's assistant at Cambridge early in 1919”. Landon and Quinney, investigated how the change in the rod length has an effect on the distortion of the pressure wave and how the mean pressure varied when the bar diameter changed. Hopkinson's apparatus allowed “a fairly close estimate...of the maximum pressure and the time during which the pressure is applicable, but this method gives no indication of the instant during the blow when the maximum pressure occurs” (Landon & Quinney, 1923).

Davies' (1948) apparatus, shown in Figure 3, further improved upon Hopkinson's apparatus by using parallel plates and cylindrical condenser microphones to electrically measure the axial and radial movements of the loaded bar.

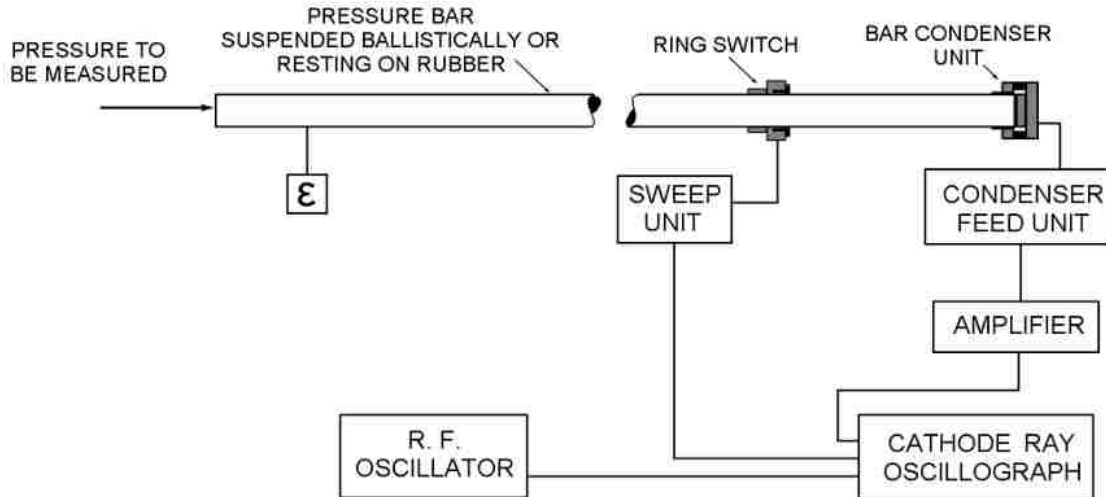


Figure 3: General arrangement of Davies' apparatus (Davies R. M., 1948).

Davies was able to measure lower pressures by eliminating the detachable end piece and to measure the time more accurately, and this enabled him to plot the "relation between pressure and time" (Davies R. M., 1948).

Kolsky (1949) also further developed a Hopkinson pressure bar apparatus to measure the stress-strain response of materials under impact loading conditions. There are two major problems encountered when investigating the behaviour of materials at very high rates of loading: these problems "are associated with inertia effects in the apparatus and with the recording of transient stresses and strains" (Kolsky H. , 1949). Kolsky (1949) added a second bar to the Hopkinson pressure bar apparatus placing the test specimen between the two pressure bars. From these experiments Kolsky was able to determine that the specimen must be significantly thin to neglect the axial inertia in the specimen, and due to the fact that the radial inertia is proportional to the square of the radius of the specimen, a smaller specimen should be used to minimize the radial inertia. The effects of friction between the specimen and bar ends and the radial inertia in the specimen may bring uncertainties to the measured stress-strain response of the material being tested. However Kolsky found that "the use of different lubricants did not

affect the results; and where permanent deformations were obtained, they were fairly uniform with no evidence of barrelling, therefore friction effects would not appear to be large” (Kolsky H. , 1949).

Krafft et al. (1954) used strain gauges on the Kolsky bar to measure the stress waves instead of the microphones used previously. The use of strain gauges has now become the standard measurement technique for Kolsky-bar experiments. Before Krafft et al. (1954), explosives were used to generate the impact stress pulse. The repeatability of explosives to generate the stress pulse is very low, and generating repeatable results with explosives was very difficult. The use of a gas gun as the loading device instead of explosives enabled Krafft et al. to generate repeatable experiments with less difficulty. The launching of the striker into the incident bar generated a trapezoidal incident pulse, which has “been traditionally recognized as an ideal for Kolsky bar experiments” (Chen & Song, 2011).

2.2.2 Compression SHPB

A compression Split Hopkinson Pressure Bar (SHPB) is composed of three major components, shown in Figure 4: a loading device, the bar components, and the data acquisition system.

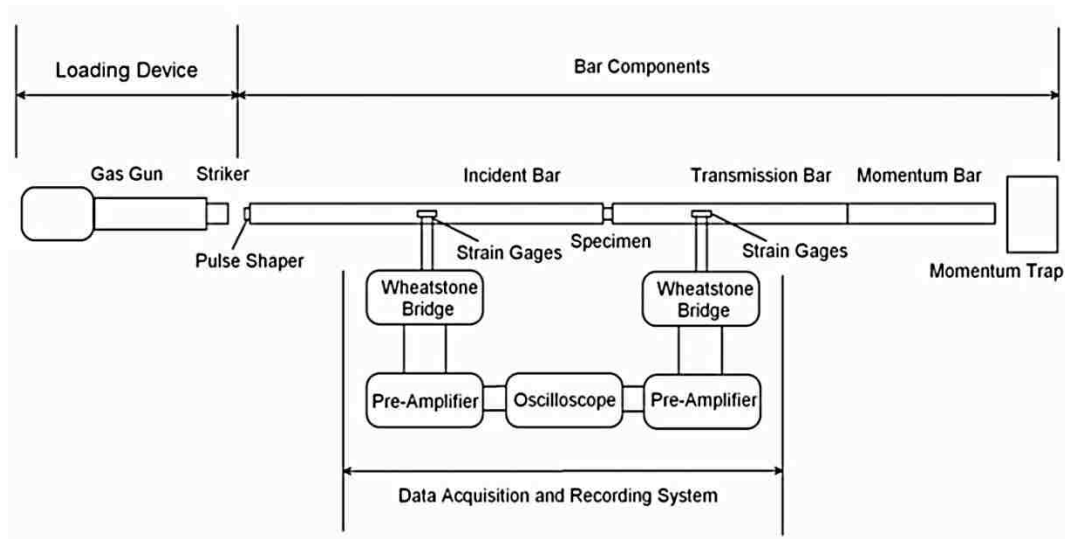


Figure 4: Typical layout and major components of a compression SHPB apparatus (Chen & Song, 2011)

The loading device is composed of a gun and striker, used to generate the stress wave in the bar components. The gun either uses explosives or compressed gas to launch the striker bar into the incident bar. Compressed-gas guns are the preferred method for launching the striker, due to the repeatability of gas guns, the ability to control the speed of the striker by changing the gas pressure and the increased safety of not having to handle explosives. The bar components are comprised of an incident bar, a transmission bar and a momentum trap. It is desirable for both the incident and transmission bars to have a high yield strength and for them to be linearly elastic. The momentum trap is used to catch the bars and dissipate the energy safely from the SHPB apparatus. Data acquisition and recording requires equipment with high sampling rates due to the small time interval over which the stress wave propagates through the bars. It is also desirable for the amplifiers to have low latency, so that the amplifiers are able to respond quickly for signal measurement and not introduce errors.

2.2.3 Types of Tensile SHPB

There are three basic versions of the tensile SHPB apparatus which have been developed over the years.

The first type of tensile test is the direct acting tensile SHPB apparatus developed by Hauser in 1966. A direct acting tensile SHPB uses a pair of concentric cylinders, with the inner cylinder being made up of two solid bars called the incident and transmission bar and with a specimen threaded between the incident and transmission bars. A hollow outer cylinder is attached to the incident bar via a transfer connection as shown in Figure 5.

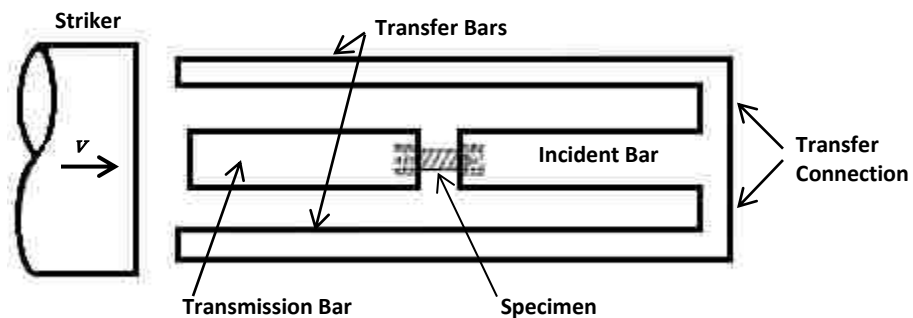


Figure 5: Direct acting tension loading (Hauser, 1966)

To impart a stress wave into the incident bar, the striker hits the transmitter bars, which sends a tension wave into the incident bar. The drawback to this arrangement is the covering of the sample by the outside cylinder which makes instrumentation difficult and use of optical measurement techniques impossible.

The second type of tensile test, developed by Lindholm and Yeakley in 1968, is the top hat specimen. This tensile test uses a modified compression SHPB apparatus, by replacing the solid transmission bar with a hollow transmission bar of the same cross-sectional area as the incident bar. The top hat-type specimen seen in Figure 6, is machined to have the tensile test areas on the side of the hat shape.

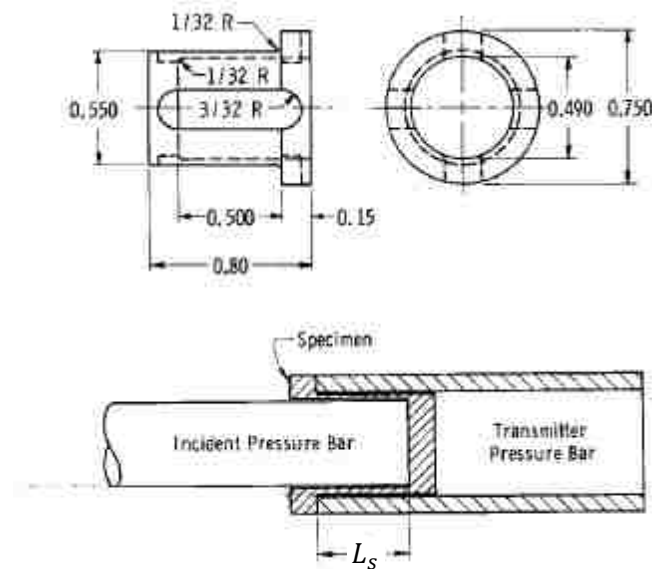


Figure 6: Top hat specimen configuration (Lindholm & Yeakley, 1968)

This specimen hat shape leads to a complex geometry that is not suitable for testing samples that cannot be machined into the required geometry. The benefit of this tension test is that very few modifications of a compression SHPB apparatus are required.

The third type of tensile test involves a compression split Hopkinson pressure bar apparatus, with a “shoulder or collar placed over the threaded specimen” (Nicholas, 1981), shown in Figure 7.

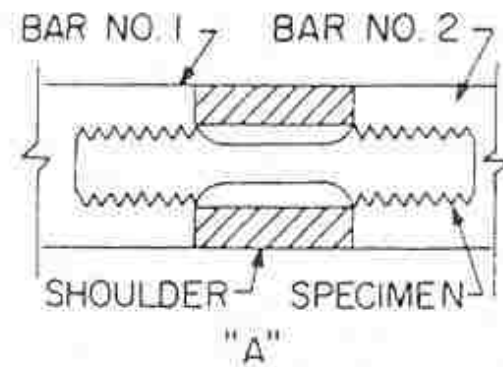


Figure 7: Nicholas experimental setup. (Nicholas, 1981)

The compression pulse travels along the incident bar, through the shoulder, through the transmission bar and reflects back as a tensile pulse to the sample. The apparatus “shoulder which carried the entire compressive pulse around the specimen, is unable to support any tensile loads because it is not fastened in any manner to the bars” (Nicholas, 1981). This setup limits the access to the specimen for optical measurement techniques and is not suitable for sheet materials.

2.2.4 The development of direct acting tensile SHPB apparatus.

The most common tensile SHPB apparatus in use today is the direct acting tensile SHPB. The direct acting tensile SHPB has been further developed into two different methods for loading the incident bar and that do not cover the test specimen. The two different loading methods consist of either static loading or dynamic loading of the incident bar.

The static loading is achieved by locking the incident bar in place with a clamp, applying a load on the non-specimen end of the bar, as shown in Figure 8. When the clamp is released, the load is suddenly transmitted to the other end of the incident bar, the specimen and the transmitter bar.

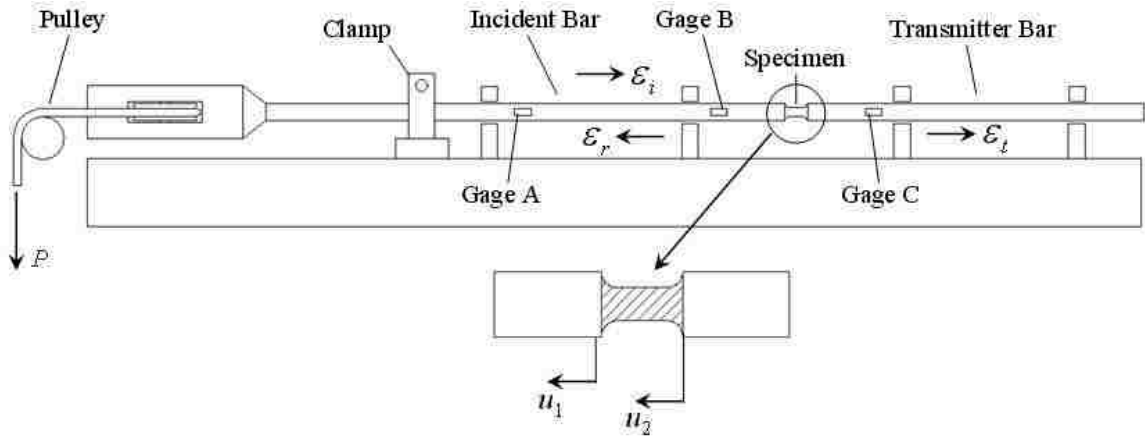


Figure 8: Static loading tensile SHPB (Ohio State University)

The design of the clamp is important “in order to minimize the possibility of applying an external load other than the reaction to the stored tension “ (Staab & Gilat, 1991). This design also allows a strain gauge to directly measure the applied tension load before releasing the clamp, which makes it easier to replicate the load for subsequent tests.

In a dynamic loading tensile SHPB apparatus, the loading is done by placing a hollow striker bar around the incident bar, and firing it with a gas gun. The hollow striker bar travels along the incident bar and strikes an anvil, or end cap, attached to the end of incident bar, as seen in Figure 9.

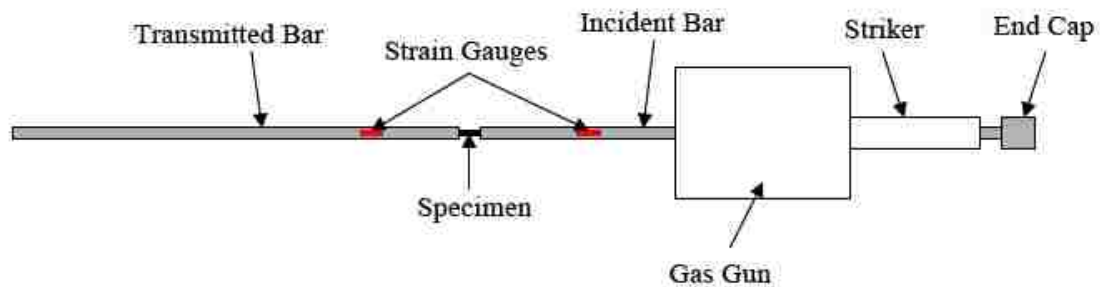


Figure 9: Layout of a dynamic loading tensile SHPB apparatus (Hasenpouth, 2010)

This set-up of the tensile SHPB apparatus ensures that the force due to the impact of the striker bar is the only force acting on the incident bar.

2.2.5 Exploring Other Tensile SHPB Apparatus Facilities

According to a literature search, the direct-acting tensile SHPB apparatuses are the most common. Most current tensile SHPB apparatuses have a useful strain rate range of 400 s^{-1} to 2000 s^{-1} . Above 1500 s^{-1} , noise in the transmitted strain signal increases and limits the upper strain rate of the tensile SHPB apparatus. A research team at Ohio State University has one of the few static loading tensile SHPB, which uses 12.7mm-diameter 7075-T6 aluminum bars, and allows testing up to 2000 s^{-1} . The use of aluminum bars allows softer materials to be tested, “in terms of impedance matching” (Gebremeskel et al., 2014). A dynamically-loaded SHPB apparatus at the University of Mississippi has bars made of various materials, ranging from maraging steel to AISI 6061-T6 aluminium to “enable the high-strain rate evaluation of metals, nano-reinforced specimens, foams and sandwich composites” (University of Mississippi, 2015). The team of researchers who developed a tensile SHPB apparatus at the University of Waterloo indicated that “momentum trapping ability allows the test to be interrupted at predetermined strain levels” (Worswick, 2015). Finally, the SHPB apparatus located at Tampere University of Technology uses “Kyowa CDV 700A series signal conditioners having a bandwidth of 500 kHz” (Tampere University of Technology, 2015) to amplify the signal from the strain gauges. This is a much larger bandwidth than is usually used; most SHPB facilities use amplifiers with a bandwidth of 100 kHz.

2.3 SHPB Theory

The following derivation of the basic SHPB equations based on wave propagation theory was developed to give the stress, strain and strain rate in the specimen using the strains measured in the incident and transmission bars. The equations for a compression SHPB apparatus are the same as a tension SHPB apparatus, other than the stress waves having the opposite signs. For analysis of the conservation of energy, the derivation is the same for compression and tension SHPB apparatuses.

2.3.1 Stress waves in cylindrical bars

Cylindrical bars of infinite length can have three types of waves propagate along the bar: longitudinal, torsional and flexural (transverse) waves. Pochhammer (1876) and Chree (1889) independently derived the equations and solutions for the propagation of longitudinal waves in an infinite elastic cylindrical bar. The “theory for an infinite cylinder is based on the boundary condition that at the free cylindrical surface both the normal stress and the shear stress vanish” (Kolsky H. , 1964). For the “fundamental mode longitudinal waves travel with velocities which depend on Poisson’s ratio, ν , and on the value of $\frac{\Lambda}{a}$, where, a , is the radius of the cylinder and, Λ , is the wavelength” (Kolsky H. , 1964). When, “ $\frac{\Lambda}{a} \gg 1$, the wave travels with the velocity, C_0 ” (Kolsky H. , 1964), from equation 2.1. As the “distance from the pressure end increases, the stress distribution becomes more uniform” (Davies R. , 1956). When the ratio of the bar length to bar diameter, L/D , is 10 or more, the stress wave is considered to be one-dimensional. With a one-dimensional stress wave “the longitudinal stress and displacement are uniform over the cross-section of the bar, the radial stress is everywhere zero” (Davies R. M., 1948). Considering the uniform longitudinal stress and uniform displacement throughout the bar we can use strain gauges on the surface of the bars to measure the strain.

2.3.2 SHPB equations

When the striker impacts the anvil on the incident bar, as shown in Figure 10, a compression stress wave, shown in red in Figure 10, propagates through the anvil to the back of the anvil and reflects as a tension stress wave through the incident bar. Due to the difference in cross sectional area of the incident bar and the specimen, part of the stress wave is reflected back toward the anvil and part of the stress wave passes through the specimen. The impact of the striker also creates a compression stress wave in the striker, shown in blue in Figure 10, which is reflected back at the free end of the striker as a tension stress wave. The tension stress wave transmits through the anvil and reflects as a compression stress wave cancelling out the tension stress wave due to the inverse amplitude, and is called the unloading wave. When the unloading wave encounters the specimen, it acts like the tension wave reflecting part back to the striker, and part traveling through the specimen.

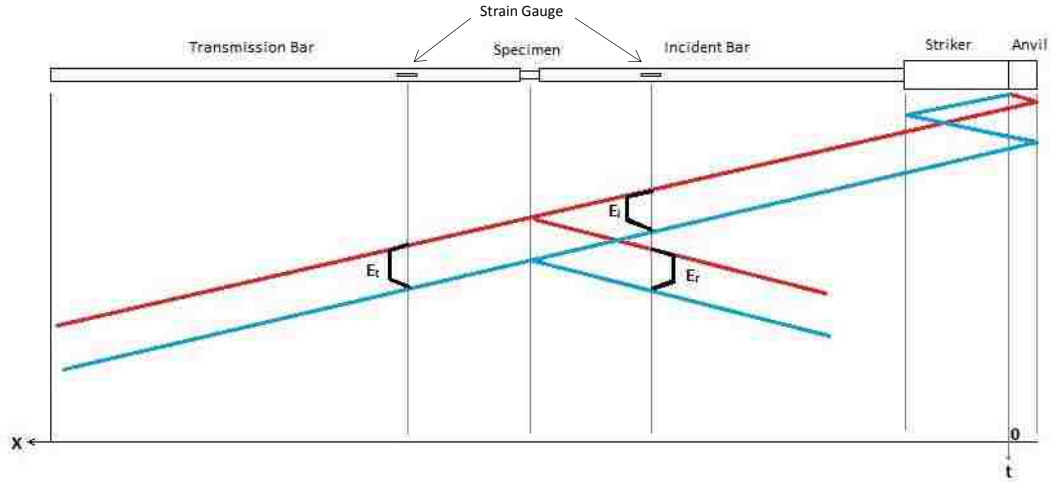


Figure 10: X-t diagram of stress wave propagation in a tensile SHPB apparatus

The velocity at which the one dimensional stress wave propagates through the material is the speed of sound in the bar material, C_B , which is a function of the Young's modulus of the bar, E , and the density of the bar material, ρ_B :

$$C_B = \sqrt{\frac{E_B}{\rho_B}} \quad (2.1)$$

The striker "transmits a 'square wave' pulse of compression into the" (Kraft, Sullivan, & Tipper, 1954) incident bar of a duration, Δt , which is determined by the length, L_{st} , of the striker bar:

$$\Delta t = \frac{2L_{st}}{C_B} \quad (2.2)$$

If the striker and the incident bars have the same material density and the same cross-sectional area, the magnitude of the induced stress pulse, σ_i , "is dependent on the striking velocity" (Chen & Song, 2011) .

$$\sigma_i = \frac{1}{2} \rho_B C_B v_{st} \quad (2.3)$$

Similarly the magnitude of the strain pulse, ε_i , is also dependent on the velocity of the striker.

$$\varepsilon_i = \frac{v_{st}}{2C_B} \quad (2.4)$$

The following derivations of the equations for stress, strain and strain rate in the specimen are given by William Sharpe Jr. (Sharpe, 2008), with the variables at the specimen rearranged for tension, as shown in Figure 11.

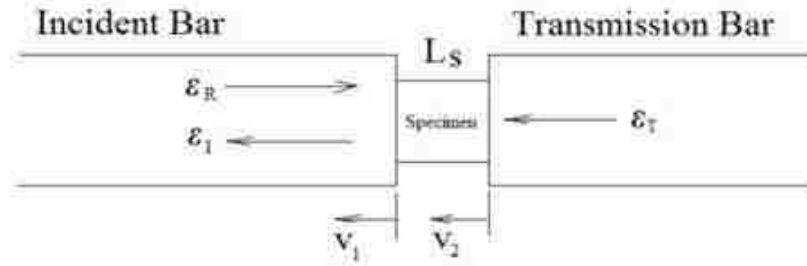


Figure 11: Variables at the specimen

These “equations assume that the stress waves propagate in the incident and transmission bars without dispersion in the bars, and by one dimensional stress wave theory that relates the particle velocities at both ends of the specimen to the three measured strain pulses” (Chen & Song, 2011).

$$v_1 = C_B(\varepsilon_R - \varepsilon_i) \quad (2.5)$$

$$v_2 = C_B(-\varepsilon_T) \quad (2.6)$$

Where the subscripts, i , R , and T , represent the incident, reflected, and transmitted strain amplitude pulses, respectively. The average engineering strain rate in the specimen is the difference in the velocity across the specimen divided by the gauge length of the specimen, L_s .

$$\dot{\varepsilon} = \frac{v_1 - v_2}{L_s} \quad (2.7)$$

Substituting equations 2.5 and 2.6 into equation 2.7 gives.

$$\dot{\bar{\epsilon}} = \frac{C_B}{L_S} (-\epsilon_i + \epsilon_R + \epsilon_T) \quad (2.8)$$

Taking the time derivative of equation 2.8 gives the average engineering strain.

$$\bar{\epsilon} = \int_0^{t_j} \dot{\bar{\epsilon}} dt = \frac{C_B}{L_S} \int_0^{t_j} (-\epsilon_i + \epsilon_R + \epsilon_T) dt \quad (2.9)$$

where, j , is the sample number to which the time integration is calculated up to. The stresses at both ends of the specimen are calculated with the following elastic relations.

$$\sigma_1 = \frac{A_B}{A_S} E_B (-\epsilon_i - \epsilon_R) \quad (2.10)$$

$$\sigma_2 = \frac{A_B}{A_S} E_B (-\epsilon_T) \quad (2.11)$$

where, A_B , and, A_S , are the cross-sectional areas of the bars and the specimen and, E_B , is the Young's modulus of the bar material. The specimen is assumed to be stress equilibrated in a Kolsky-bar experiment, such that the specimen uniformly deforms during the experiment.

$$\sigma_1 = \sigma_2 \quad (2.12)$$

By substituting equations 2.10 and 2.11 into equation 2.12 gives.

$$-\epsilon_i - \epsilon_R = -\epsilon_T \quad (2.13)$$

Substituting equation 2.13 into equations 2.8, 2.9 and 2.10 gives

$$\dot{\epsilon}_u = 2 \frac{C_B}{L_S} \epsilon_R \quad (2.14)$$

$$\epsilon_u = 2 \frac{C_B}{L_S} \int_0^{t_j} \epsilon_R dt \quad (2.15)$$

$$\sigma_u = \frac{A_B}{A_S} E_B \epsilon_T \quad (2.16)$$

Equations 2.14, 2.15 and 2.16 are known as the Hopkinson equations.

If the specimen does not experience perfect equilibrium when deformed, the mean value of the stresses experienced at both ends of the specimen is taken to get the average stress in the specimen:

$$\bar{\sigma} = \frac{1}{2}(\sigma_1 + \sigma_2) = \frac{1}{2} \frac{A_B}{A_s} E_B (-\varepsilon_T - \varepsilon_R - \varepsilon_i) \quad (2.17)$$

However, equation 2.17 is not valid if the “stress or strain in the specimen is in a drastic non-uniformity” (Chen & Song, 2011). This uniformity can be checked by using equation 2.12.

2.3.3 SHPB Theory using Conservation of Energy

The following analysis of the conservation of energy in a SHPB is from Chen and Song (Chen & Song, 2011). When a stress wave propagates in a long rod, the mechanical energy of the stress wave takes the form of strain energy through bar deformation and kinetic energy through bar motion (Chen & Song, 2011). Using the incident strain, ε_i , caused by the stress wave moving through the incident bar, the elastic strain energy, U_i , can be calculated.

$$U_i = V_i \int_0^{\varepsilon_i} \sigma d\varepsilon \quad (2.18)$$

where, V_i , is the deformed volume in the incident bar. The deformed volume in the incident bar depends upon the loading duration and the cross-sectional area of the incident bar, which can be expressed by:

$$V_i = A_B C_B \Delta t \quad (2.19)$$

The linear elastic stress in the incident bar can be expressed as:

$$\sigma_i = E_B \varepsilon_i \quad (2.20)$$

Substituting equation 2.20 into 2.18 gives.

$$U_i = \frac{1}{2} A_B C_B E_B \Delta t \varepsilon_i^2 \quad (2.21)$$

The elastic strain energies of the reflected and transmitted waves, U_R and, U_T , can be calculated using a similar derivation giving:

$$U_R = \frac{1}{2} A_B C_B E_B \Delta t \varepsilon_R^2 \quad (2.22)$$

$$U_T = \frac{1}{2} A_B C_B E_B \Delta t \varepsilon_T^2 \quad (2.23)$$

The specimen deformation based on the contribution of the elastic strain energy in the bars is given by:

$$\delta_{es} = U_i - U_R - U_T \quad (2.24)$$

Substituting equations 2.21, 2.22 and 2.23 into equation 2.24 gives:

$$\delta_{es} = \frac{1}{2} A_B C_B E_B \Delta t (\varepsilon_i^2 - \varepsilon_R^2 - \varepsilon_T^2) \quad (2.25)$$

When the specimen is in a state of dynamic stress equilibrium equation 2.25 is:

$$\delta_{es} = -A_B C_B E_B \Delta t \varepsilon_R \varepsilon_T \quad (2.26)$$

It is understood that the energy difference is positive since the reflected strain, ε_r , takes the opposite sign of the incident and transmitted strains. Considering the kinetic energy, KE_i , in the incident bar due to the incident wave as.

$$KE_i = \frac{1}{2} m v_i^2 \quad (2.27)$$

where m and v_i are the mass and particle velocity of the deformed portion of the incident bar which are given by:

$$m = \rho_B A_B C_B \Delta t \quad (2.28)$$

$$v_i = C_B \varepsilon_i \quad (2.29)$$

Substituting equations 2.28 and 2.29 into equation 2.27 gives:

$$KE_i = \frac{1}{2} \rho_B A_B C_B^3 \Delta t \varepsilon_i^2 \quad (2.30)$$

The kinetic energies of the reflected and transmitted waves, KE_R and KE_T , can be calculated using a similar derivation giving:

$$KE_R = \frac{1}{2} \rho_B A_B C_B^3 \Delta t \varepsilon_R^2 \quad (2.31)$$

$$KE_T = \frac{1}{2} \rho_B A_B C_B^3 \Delta t \varepsilon_T^2 \quad (2.32)$$

The contribution of the kinetic energy to the specimen deformation is:

$$\delta_{KES} = KE_i - KE_R - KE_T \quad (2.33)$$

Substituting equations 2.30, 2.31 and 2.32 into equation 2.33 gives.

$$\delta_{KES} = \frac{1}{2} \rho_B A_B C_B^3 \Delta t (\varepsilon_i^2 - \varepsilon_R^2 - \varepsilon_T^2) \quad (2.34)$$

When the specimen is in stress equilibrium equation 2.34 becomes:

$$\delta_{KES} = -\rho_B A_B C_B^3 \Delta t \varepsilon_R \varepsilon_T \quad (2.35)$$

For linear elastic bars,

$$E_B = \rho_B C_B^2 \quad (2.36)$$

Substituting equations 2.36 into equation 2.35 gives:

$$\delta_{KES} = -A_B E_B C_B \Delta t \varepsilon_R \varepsilon_T \quad (2.37)$$

It can be noted that the specimen deformation due to kinetic energy has the same form as the specimen deformation due to the elastic strain energy. If the specimen is assumed to have a perfectly plastic response, the specimen deformation energy is simplified to.

$$U_s = A_s L_s \sigma_y \varepsilon_p \quad (2.38)$$

where, A_s , is the initial cross-sectional area of the specimen and, L_s , is the initial length of the specimen. The yield strength, σ_s , and the plastic strain, ε_{ps} , of the specimen is:

$$\sigma_s = \frac{A_B}{A_s} E_B \varepsilon_T \quad (2.39)$$

$$\varepsilon_{ps} = \varepsilon \Delta t = -2 \frac{C_B}{L_s} \varepsilon_R \Delta t \quad (2.40)$$

Equation 2.40 is based on constant strain rate deformation in the specimen. Substituting equations 2.39 and 2.40 into equation 2.38 gives:

$$U_s = -2 A_B E_B C_B \Delta t \varepsilon_R \varepsilon_T \quad (2.41)$$

Therefore the specimen deformation energy is equal to.

$$U_s = 2 \delta_{es} = 2 \delta_{KES} \quad (2.42)$$

From equation 2.42 it can be seen that half of the energy needed to deform the specimen comes from the elastic strain energy in the bars and half comes from the kinetic energy in the

bars. It should be noted that this analysis does not include the kinetic energy in the specimen. Knowing that half the energy needed to plastically deform the specimen is important for setting up the momentum trap. If the momentum trap stops the movement of the incident bar too quickly, the specimen will not plastically deform and the specimen will not reach the ultimate strength and break.

2.3.4 Striker Velocity

The velocity of the striker is the determining factor of the specimen strain rate. The stresses generated upon impact of the striker on the incident bar can be determined from the strain gauge mounted on the incident bar. The stress in the striker, σ_{st} , and incident bar, σ_i , are “related with the velocity in the common interface” (Gallina, Birch, & Alves, 2003) by the two equations from Johnson (1972):

$$\sigma_{st} = \rho_{st} C_{st} (v_{st} - v_i) \quad (2.43)$$

$$\sigma_i = \rho_B C_B v_i \quad (2.44)$$

Also at impact, the force exerted onto the incident bar is equal to the reaction force exerted on the striker:

$$F_{st} = F_i \quad (2.45)$$

$$A_{st} \sigma_{st} = A_B \sigma_i \quad (2.46)$$

Substituting equation 2.43 and 2.44 into equation 2.46 gives:

$$A_{st} \rho_{st} C_{st} (v_{st} - v_i) = A_B \rho_B C_B v_i \quad (2.47)$$

$$\beta = \frac{A_{st} \rho_{st} C_{st}}{A_B \rho_B C_B} \quad (2.48)$$

In order to ensure one dimensional wave propagation, the properties and cross-sectional areas of the striker bar and incident bar must be equal, which yields $\beta = 1$. Therefore equation 2.47 can be rearranged as:

$$v_i = \frac{\beta v_{st}}{1 + \beta} = \frac{v_{st}}{2} \quad (2.49)$$

Substituting equation 2.49 into equation 2.43 and equation 2.44 gives:

$$\sigma_{st} = \rho_B C_B \left(v_{st} - \frac{v_{st}}{2} \right) = \frac{\rho_B C_B v_{st}}{2} \quad (2.50)$$

$$\sigma_i = \rho_B C_B \frac{v_{st}}{2} \quad (2.51)$$

Similar to the interface between the striker and incident bars, the force exerted onto the specimen is equal to the reaction force exerted on the incident bar, assuming no losses:

$$F_i = F_s \quad (2.52)$$

Recalling that the stress pulse is both transmitted and reflected at this interface, the transmitted and reflected stress pulses are:

$$A_B \sigma_t = A_s \sigma_s \quad (2.53)$$

$$\sigma_t = \frac{A_s \sigma_s}{A_B} \quad (2.54)$$

$$\sigma_r = E_B \epsilon_r \quad (2.55)$$

where “ σ_t ” is the transmitted stress, “ σ_r ” is the reflected stress, and “ A_s ” is the cross-sectional area of the specimen. Substituting equation 2.55 into equation 2.14 gives:

$$\sigma_r = \frac{E_B L_s}{-2C_B} \dot{\epsilon} \quad (2.56)$$

Given that the transmitted stress is equal to the difference between the incident stress and the reflected stress, the incident stress is equal to:

$$\sigma_i = \sigma_t - (-\sigma_r) \quad (2.57)$$

Substituting equations 2.54 and 2.56 into equation 2.57 gives:

$$\sigma_i = \frac{A_s \sigma_s}{A_B} + \frac{E L_s}{2C_B} \dot{\epsilon} \quad (2.58)$$

And substituting equation 2.58 into equation 2.51 gives:

$$v_{st} = \frac{2}{\rho_B C_B} \left(\frac{A_s}{A_B} \sigma_s + \frac{E_B L_s}{2 C_B} \dot{\epsilon} \right) \quad (2.59)$$

Equation 2.59 “allows the calculation of the striker velocity so a given strain rate and stress level in the specimen” (Gallina, Birch, & Alves, 2003) can be achieved.

The maximum velocity for the striker is limited by the yield strength of the bar material. Since the bar must not deform plastically the induced stress pulse, σ_i , in equation 2.3 can be substituted with the bar material yield strength, S_{yB} , and equation 2.3 can be rearranged as:

$$v_{st \max} = \frac{2 S_{yB}}{\rho_B C_B} \quad (2.60)$$

Equation 2.3 allows the maximum velocity of the striker to be calculated which will not cause plastic deformation of the bars.

Chapter 3: Design, Construction, and Assembly of SHPB

3.1 Overview of a Tensile Split Hopkinson Pressure Bar Apparatus

The Tensile SHPB apparatus is used to test materials in tension at various strain rates. This apparatus described in this thesis was specified to test sheet materials with a tensile strength up to 1500 MPa at strain rates up to 2000 s^{-1} . The SHPB apparatus is composed of mechanical components, shown in Figure 12, and instrumentation that will gather the data from the apparatus.

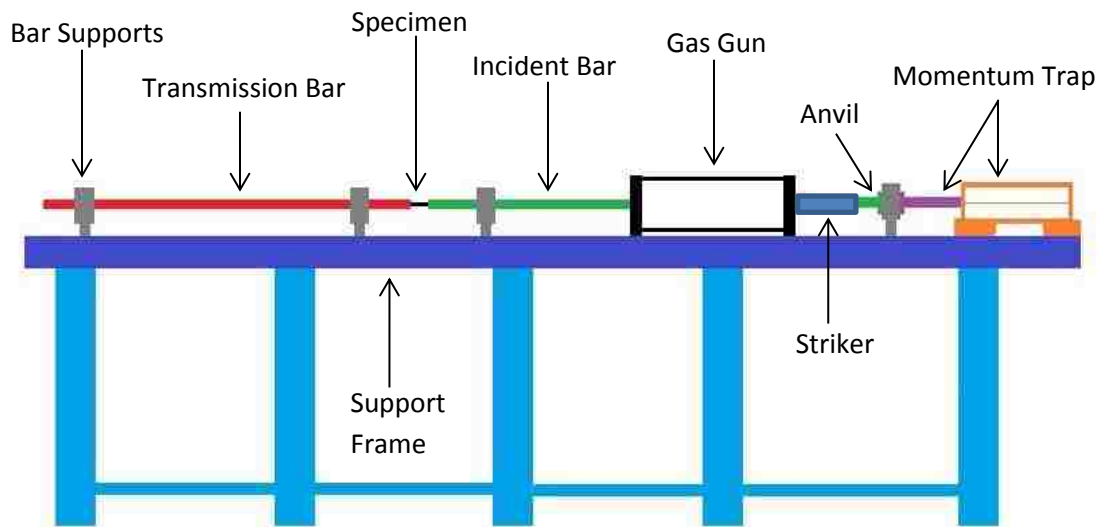


Figure 12: Mechanical components of tensile SHPB

The mechanical components are composed of a support frame, incident bar, transmission bar, bar supports, gas gun, the momentum trap, and the specimen; these will be described in detail in Section 3.2. The instrumentation components are comprised of the data acquisition system, pressure transducer, strain gauges, strain gauge completion circuits, strain gauge amplifiers, and an optical gate to measure the velocity of the striker; these components will be described in Section 3.3.

3.2 Mechanical Components

3.2.1 Support Frame

A stable frame to mount the tensile SHPB apparatus is required. The SHPB frame must also be adjustable for level, because the floor surface cannot be assumed to be level. To meet these requirements an I-beam mounted on adjustable support legs was designed as part of a 2012 capstone project to build a compression SHPB apparatus. To accommodate both tensile and compressive SHPB apparatuses two I-beams were mounted parallel on the adjustable frame seen in Figure 13.



Figure 13: Support frame for SHPB apparatus

The length of the I-beam was determined by the length of the SHPB apparatus plus extra length for future expansion if longer incident or transmission bars were used. A W5x16 I-beam “was chosen based off the width of its flange” (Zanettin, Young, & Hussain, 2012), with a length of 8.5m. The I-beam supports were located every 1.3m for a total of six supports. With this spacing between supports, the maximum deflection of the I-beam between the supports was calculated to be 0.2mm (Zanettin, Young, & Hussain, 2012) under static loading. The deflection of the I-beam can be compensated for by the adjustment built into the bar holders. The Vertical

supports, shown in Figure 14 (the technical drawings can be found in Appendix B), were made of 74mm x 74mm and 25mm x 25mm AISI 1020 CD square tubing.

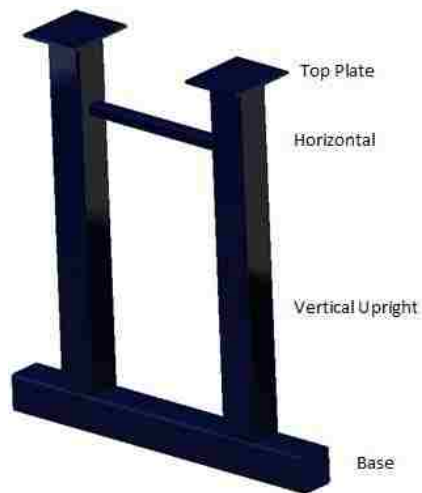


Figure 14: Vertical support (Zanettin, Young, & Hussain, 2012)

Each vertical upright has a top plate welded at one end to accommodate the I-beam and is welded to the base tube which has adjustable feet bolted to it for leveling of the frame assembly. To keep the vertical uprights the correct distance apart near the top plate, 25mm x 25mm tube was welded between the two vertical tubes. There are also slender horizontal support beams, shown in Figure 15, made of 25mm x 25mm tubing with a plate welded onto both ends of the tube, used to bolt onto the vertical supports.



Figure 15: Horizontal support bar (Zanettin, Young, & Hussain, 2012)

The horizontal support is used to keep the support legs from moving horizontally.

3.2.2 Bar Holders

The bar holders, designed during a 2012 capstone project for the compression SHPB apparatus, were designed to allow fine adjustment of the incident and transmission bars in three dimensional space and support the incident and transmission bars with minimal friction. The exploded view of the bar holder, shown in Figure 16, gives an overview of the components that make up the bar holder.

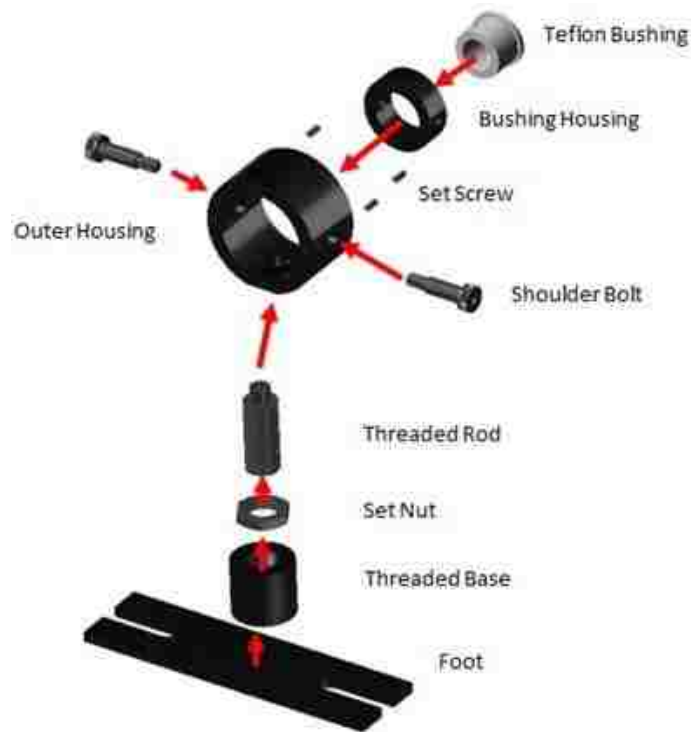


Figure 16: Exploded view of SHPB bar holder (Zanettin, Young, & Hussain, 2012)

The technical drawing in Appendix B shows the actual dimensions of the bar holder. The foot, threaded base, outer housing, and the bushing housing were made of AISI 1018 steel. The threaded rod is 3/4" UNF with a shoulder machined into one end to support the outer housing. A Teflon bushing was pressed into the bushing housing to give the incident and transmission bars a low friction surface to move on. The adjustment shown in Figure 17, allows the incident and transmission bars to be aligned coaxially with the gas gun.



Figure 17: Bar holder showing adjustability (Zanettin, Young, & Hussain, 2012)

The threaded rod allows the height of the outer housing to be raised or lowered, with the set nut locking the threaded rod's movement once the final height is set. The outer housing can rotate on the threaded rod's machined shoulder to align the bushing housing perpendicular to the incident, transmission and unloading bars, with a set-screw to lock the bushing housing once the final alignment is reached. The shoulder bolts allow the bushing housing to move from side to side in the outer housing and to rotate around the axis of the shoulder bolts, two set screws lock the shoulder bolts in the final place.

The bar holders were clamped to the support frame I-beams with two threaded rods between the bar holder and a lower bar, as shown in Figure 18. By using a clamping mechanism, instead of bolting the bar holders onto the I-beam, the position of the bar holders along the I-beam can be adjusted for different lengths of incident and transmission bars.



Figure 18: Bar holder clamped to support frame.

3.2.3 Striker and Bars

A) Striker

The striker must have good impact resistance in order to resist plastic deformation when it strikes the incident bar. The striker was machined from AISI 4140/ASTM A29 round bar, a material with good impact resistance. AISI 4140 steel “has high fatigue strength, abrasion and impact resistance, toughness, and torsional strength” (AZO Materials, 2015). The chemical composition of the AISI 4140 steel is provided in Table I.

Table 1: AISI 4140 / ASTM A29 (4140) Elements (ASTM , 2012)

Grade Designation	Carbon	Manganese	Phosphorus Max	Sulfur Max	Silicon	Chromium	Molybdenum
4140	0.38 - 0.43	0.75 - 1.00	0.035	0.040	0.15 - 0.35	0.80 – 1.10	0.15 - 0.25

The physical properties of AISI 4140 steel are presented in Table 2.

Table 2: Physical Properties of AISI 4140 (MatWeb, 2015)

Material	Density (kg/m ³)	Yield strength 0.2% (MPa)	Ultimate Tensile Strength (MPa)	Young's Modulus (GPa)	Elongation at Break (%)
AISI 4140	7850	415-1735	655 -1965	205	11-25.7



Figure 19: Striker

The striker, shown in Figure 19 (the technical drawing can be found in Appendix B), was manufactured by first drilling the hole down the length of a solid bar stock and then reaming the inside diameter of the hole to 19.1 mm, so as to have a slip fit over the incident bar. Secondly, the outside surface of the striker was turned down to a diameter of 27mm to provide a slip fit inside the gas gun, using the finished inside hole to make the outside axisymmetric with the inside hole.

B) Incident and Transmission Bars

In order for the stress wave to propagate with the same velocity through both the incident bar, transmission bar and the striker, the incident bar and transmission bar were fabricated from the same material as the striker, AISI 4140 alloy steel. The incident and transmission bars were machined identically to form a matched set of bars. The incident bar and transmission bar are composed of two parts: the bar and an anvil as seen in Figure 20.



Figure 20: Close up view of the bar and anvil attached

The AISI 4140 round bar from which the incident and transmission bars were made was purchased with the final outside diameter ground and polished to 19.05mm. Both incident and transmission bars are 2000mm long, which yields a length-to-diameter ratio of $L/D = 105$, so as to ensure a one-dimensional stress wave. One end of the bar was then threaded with 0.75" UNF thread (ASME, 2003), as seen in Figure 21, to attach the anvil to the bar. The durability of the threads subject to cyclic loading is provided in Appendix A. It was estimated that, under the maximum loading conditions, the threads on the incident bar and mating anvil would withstand approximately 30,000 cycles before failure.



Figure 21: Close up view of the threads on the bar

The other end of the incident bar has a slot, as shown in Figure 22, that was designed to accommodate the test specimen. This slot was precision electric discharge machined with a serrated surface finish to better grip the specimen. Figure 23 shows that the serrated surfaces of the slot are able to effectively grip a test specimen as they leave indentation marks on the specimen itself.



Figure 22: Slot in bars to hold test specimen



Figure 23: Specimen showing serrations from specimen slot in bars

The specimen slot was made 1.5mm wide to accept test specimens taken from sheet materials 1.5mm thick. The depth of the slot is 22.4mm. A two-piece aluminum clamp-on shaft collar is used to compress the incident/transmission bar specimen slot around the specimen, to hold the specimen in place during the test. The two-piece aluminum clamp-on shaft collar was ordered from McMaster-Carr (part number 6436K72).

The anvil was also made from the AISI 4140 round bar and was turned to a final outside diameter of 27mm, which is the same outside diameter as that of the striker. A hole was then turned in the centre of the anvil about half way along its length, and then threaded with a 0.75" UNF thread (ASME, 2003) so as to screw the anvil onto the incident bar. Figure 24 shows a photograph of the threaded anvil.



Figure 24: Anvil showing threading

Loctite threadlocker Blue 242 thread locking compound was used to fill in the voids between the threads to prevent the threads from loosening due to shock and vibration.

3.2.4 Gas gun

The gas gun was positioned on the I-beam frame in such a way that the striker will fit around the incident bar and slide along it at high velocity and strike the anvil with the required force. The gas gun is composed of three main components: a barrel, a pressure chamber and a valve assembly. Using mechanically actuated valves the pressure chamber is filled to the pressure required to achieve the desired striker velocity. This pressure is determined from equation (3.1). Once the gas gun pressure chamber reaches the required pressure, the pneumatic actuators move the valve toward the specimen uncovering two openings in the gas gun barrel. The valve blocks one end of the gas gun barrel, leaving the opposite side as the path of least resistance for the gas to escape. As the gas enters the gun barrel and the gas volume expands, the striker is accelerated along the incident bar up to the required velocity.

Using Newton's equations of motion, Berggren & Reynolds (1970) proposed an equation written in terms of a non-dimensional barrel length and projectile length, for a cylindrical projectile:

$$v_{st} = \left[\frac{2P}{\rho_p} \frac{L_{bar}/D_p}{L_{st}/D_p} \right]^{1/2} \quad (3.1)$$

The projectile velocity can be maximized by increasing the pressure and L_{bar}/D_p , while minimizing the density of the projectile and L_{st}/D_p . When the bore of the gun is held at a specific diameter, the velocity of the projectile will increase with an increase in the length of the barrel of the gun as can be seen in Figure 25.

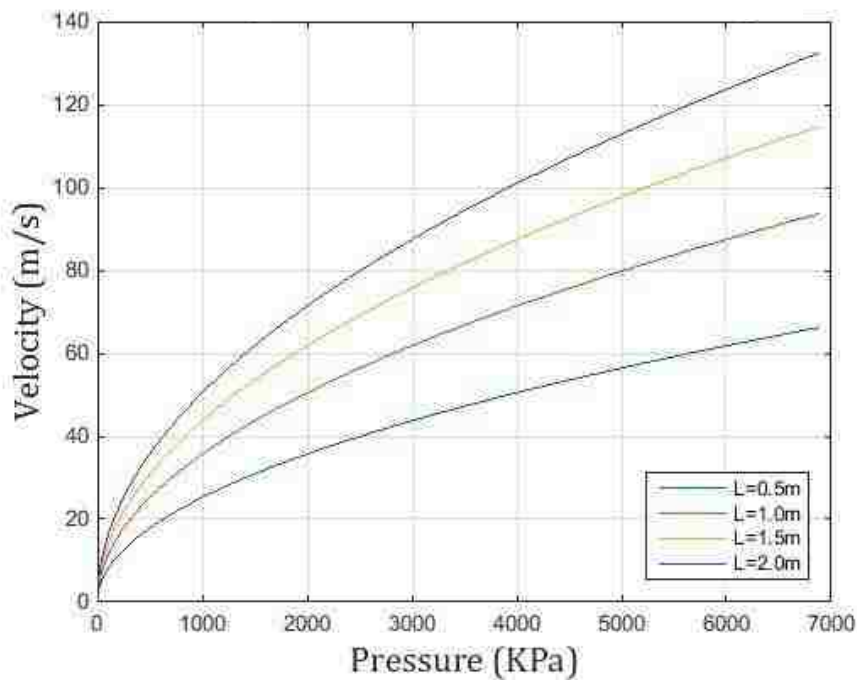


Figure 25: Velocity of striker for various barrel lengths

The gas gun was designed considering that the incident and transmission bars would be made of C350 maraging steel. This grade of steel was selected so that higher strength test specimens could be tested without plastically deforming the incident and transmission bars. The physical properties of C350 maraging steel are shown in Table 3.

Table 3: Physical Properties of C350 maraging steel (Cardarelli, 2008)

Material	Density (kg/m ³)	Yield strength 0.2% (MPa)	Ultimate Tensile Strength (MPa)	Young's Modulus (GPa)	Elongation at Break (%)
C350	8000	2318	2339	200	8

From equation 2.60, the maximum velocity of the striker for bars made of C350 maraging steel was calculated to be 121.14 m/s. Using Figure 25, a barrel length of 1m was selected, so the striker would not exceed the velocity of the striker that would induce plastic deformation in the C350 maraging steel. Using a 1m long barrel also kept the incident bar supports a reasonable distance apart. The barrel length was limited by the 1.2m-stroke of available gun drilling machines. The gas gun's maximum pressure was selected to be 6895 kPa, since this pressure will allow the striker to reach the design stress and strain rates while keeping the striker velocity below the maximum allowable for C350 maraging steel bars.

The technical drawings for the gas gun are in Appendix B, and the following is a brief description of how the parts were manufactured. The barrel was fabricated from AISI 304 stainless steel bar stock to eliminate corrosion inside the barrel. The physical properties of AISI 304 stainless steel are shown in Table 4: Physical properties of AISI 304 stainless steel.

Table 4: Physical properties of AISI 304 stainless steel (Cardarelli, 2008)

Material	Density (kg/m ³)	Yield strength 0.2% (MPa)	Ultimate Tensile Strength (MPa)	Young's Modulus (GPa)	Elongation at Break (%)
AISI 304	8000	205-760	515-1035	200	7-40

This AISI 304 stainless steel bar stock was turned into a hollow barrel by gun drilling along the central axis of the bar to an inside diameter of 27mm, then using a boring bar the valve area was enlarged to the final diameter of 38mm. Two openings were then machined to allow the pressurized gas to transfer from the pressure chamber into the gun barrel.

The pressure chamber, seen in Figure 26, is composed of four parts: two end plates, the gun barrel and a thick-wall cylinder.

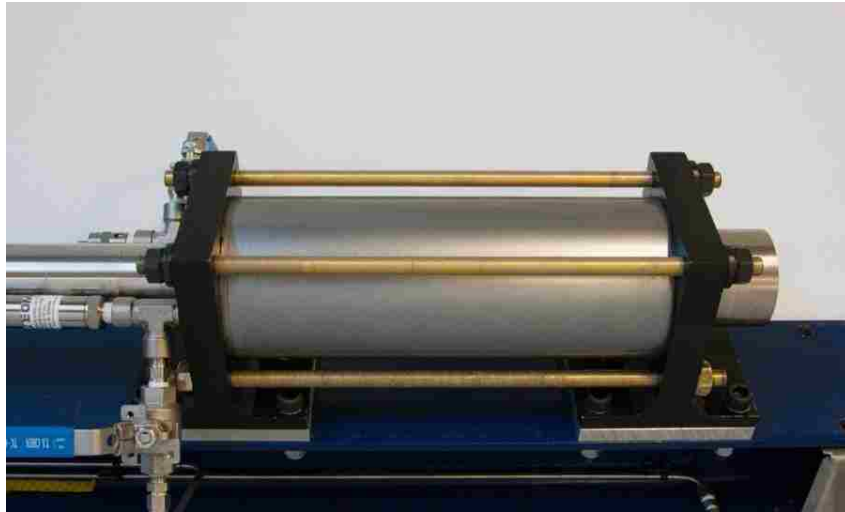


Figure 26: Gas gun pressure chamber

A cross section view shown in Figure 27, shows the relationship of the gas gun parts.

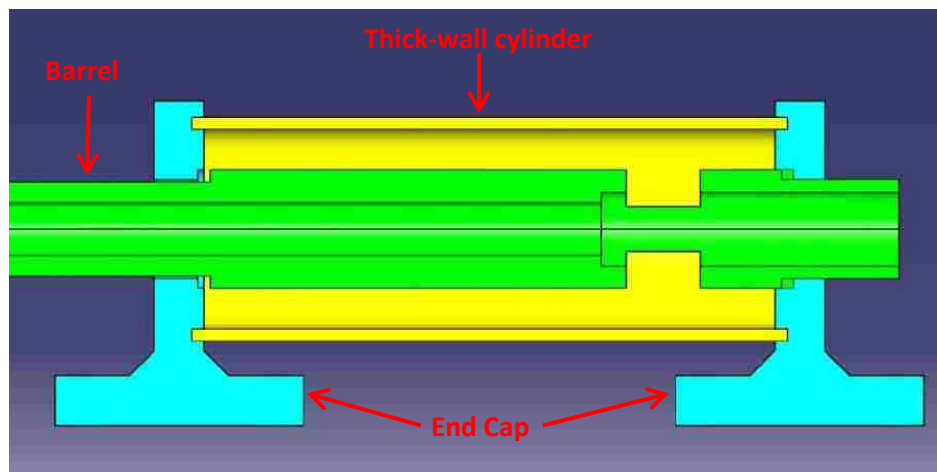


Figure 27: Gas gun cross section

The end caps of the pressure chamber serve two purposes. First, they are the end caps that seal the pressure chamber and enable it to hold a pressure. Secondly, they locate the barrel at a distance above the base frame and provide a means for the gas gun to be firmly mounted onto the base frame. The two end plates were machined from solid blocks of AISI 1018 steel into an inverted “T” shape with a hole in the centre of the upright to allow the barrel to pass through, and a circular groove machined into the upright to have a transition fit with the ends of the

thick-wall cylinder. The thick-wall cylinder was fabricated from a 114.5mm diameter, solid AISI 4140 bar stock by boring out the center material to achieve a final inside diameter of 101.8mm. The thick-wall cylinder was fabricated this way to avoid having a weld seam in the pressure chamber. The thick-wall cylinder was placed concentrically around the barrel and held in place by the two end caps. The thickness of the thick-wall cylinder was calculated using the following equation from Pressure vessels the ASME code simplified (Carson Sr., Chuse, & Ellenberger, 2004), for a thick-wall cylinder was used:

$$t_c = \frac{PR}{SJ - 0.6P} \quad (3.2)$$

This equation is valid for “use when, t_c , is less than $1/2 R$ or P , is less than $0.385 SJ$ ” (Carson Sr., Chuse, & Ellenberger, 2004). The joint efficiency is equal to 1, since there is no weld joint in the thick-wall cylinder, and the allowable stress has a value of “ $S = 95 \text{ MPa}$ ”

(Carson Sr., Chuse, & Ellenberger, 2004). This gave a wall thickness of 3.85mm, but a thickness of 6.35mm was used on the thick-wall cylinder for ease of machining the thick-wall cylinder. The thickness of the two end caps was also calculated from Pressure vessels the ASME code simplified (Carson Sr., Chuse, & Ellenberger, 2004) according to the following relationship:

$$t_{ec} = d \sqrt{\frac{CP_s}{SJ}} \quad (3.3)$$

where:

d = Bolt circle “diameter, or short span, measured as indicated in Figure PG-31” (ASME, 2010) in the ASME boiler and pressure vessel code.

C = Factor depending on method of attachment, “listed in PG-31.4” (ASME, 2010) in the ASME boiler and pressure vessel code.

From the ASME boiler and pressure vessel code (2010), the value for, C , was determined to be 0.30 and, d , was calculated to be 141mm. With these values the thickness of the flat end caps was calculated to be 20.78mm, however a thickness of 25.4mm was used since this is a common size available from steel suppliers.

The valve assembly, seen in Figure 28, consists of a cylindrical valve, pneumatic cylinders, a mount for the pneumatic cylinders and a collar to attach the pneumatic cylinders to the cylindrical valve.

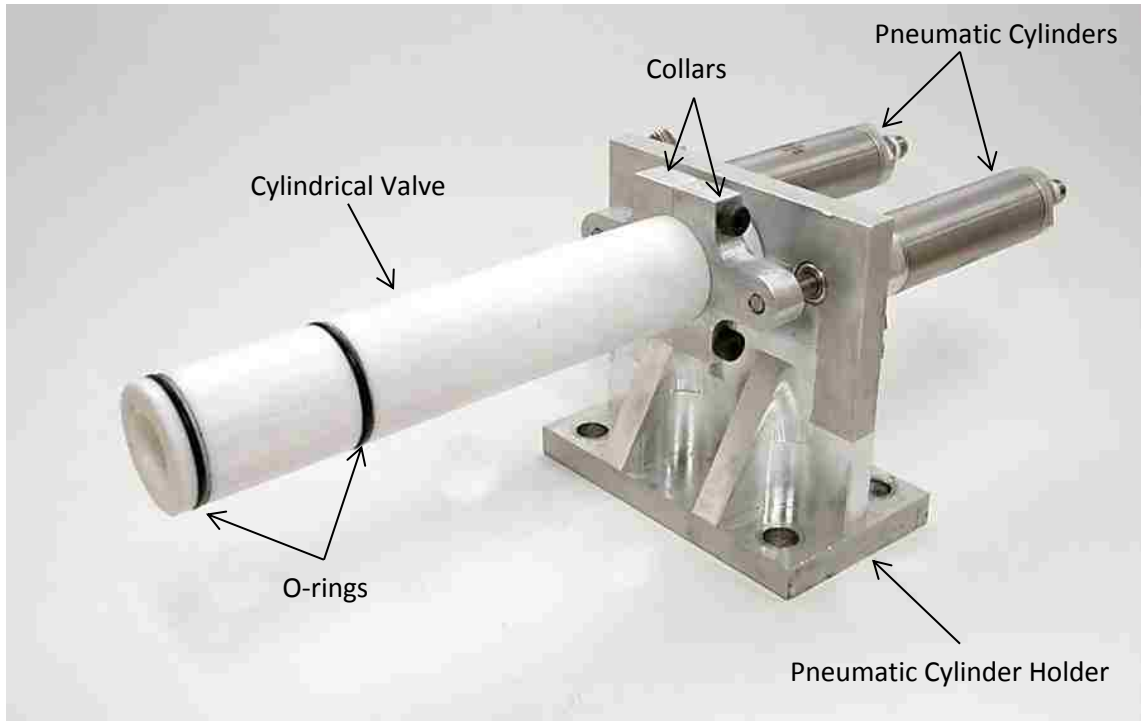


Figure 28: Valve assembly for gas gun

The cylindrical valve was fabricated from Teflon with a tight fit with the barrel, with two O-ring grooves to seal the barrel off from the pressure chamber, and a groove for locating the collar which is attached to the pneumatic cylinders. The valve has a hole in the center to concentrically locate the incident bar in the barrel. The collar is composed of two “Y” shaped pieces machined out of AISI 6160 aluminum that bolt together around the valve, and have a threaded hole in each arm to attach the two pneumatic cylinders. Each pneumatic cylinder is a double acting, 27mm bore, nose mount, with a force of 271 N at a pressure of 689 kPa. The pneumatic cylinder holder is machined out of a block of AISI 6160 aluminum, with a centre hole to clear the incident bar and two threaded holes to mount the pneumatic cylinders parallel to the incident bar.

3.2.5 Momentum trap

The purpose of the momentum trap is to arrest the forward motion of the incident bar, by dissipating its kinetic energy in a controlled manner. Another use of the momentum trap is to interrupt the test at a predetermined strain level. When the striker hits the anvil on the incident bar, the compressive pulse travels through the anvil into the momentum trap transfer bar and reflects as a tensile pulse at the end of the transfer bar. This reflected tensile pulse pulls the momentum trap transfer bar away from the anvil on the incident bar and traps the pulse within the momentum trap transfer bar. The trapped pulse energy is then dissipated into the momentum trap where the pulse energy is converted into heat through friction. With the compressive pulse trapped in the momentum trap, “the incident bar remains at rest” (Chen & Song, 2011) and “consequently the specimen is subject to only the first tensile loading” (Chen & Song, 2011). In order for the specimen to be “subject to only the first tensile loading” (Chen & Song, 2011) from the striker, the gap between the momentum trap transfer bar and the incident bar must be set precisely prior to the test.

The momentum trap, shown in Figure 29, is composed of a heavy steel base with a V groove that extends most of the length of the base, and a top cap that holds a rubber block and bolts onto the steel base.



Figure 29: Momentum trap assembly

A brass pin is sandwiched between the base and the rubber block to transfer the energy from the transfer bar to the momentum trap. The V groove in the base, shown in Figure 30, does not extend the whole length of the base, so as to provide a safety stop if the brass pin is hit with too much kinetic energy.



Figure 30: V groove in momentum trap base

There is a transfer bar which is used to transfer the kinetic energy of the incident bar to the brass pin of the momentum trap. This transfer bar is made of the same material as the incident bar. Since the transfer bar weighs less than the incident bar, it will move further than the incident bar and unload the stress wave from the incident bar so that the stress wave does not propagate multiple times down the incident bar. The transfer bar then pushes on the brass pin of the momentum trap to push the pin into the momentum trap dissipating the kinetic energy into heat from friction between the rubber block, the brass pin and the steel base.

3.2.6 Specimen design

Reviewing different papers on tensile SHPB apparatuses leads to the conclusion that the design of the specimen will vary with the design of the tensile SHPB apparatus. Smerd, et al., (2005) listed “two requirements for a tensile SHPB specimen are a small gauge length to reduce ring-up

time and inertial effects, as well as a geometry that results in a uni-axial stress state". These design requirements lead to a specimen design, shown in Figure 31, optimized for the University of Waterloo tensile SHPB apparatus, where the gauge length is $L = 12.5$ mm and the gauge width is $T = 1.75$ mm.

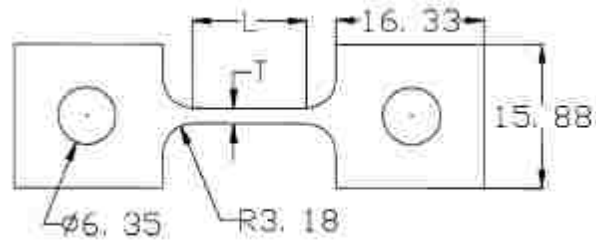


Figure 31: University of Waterloo specimen design (Smerd, Winkler, Salisbury, Worswick, Lloyd, & Finn, 2005)

The “specimen geometry for dynamic tests was chosen to: (i) follow the mechanical response of a standard ASTM specimen at quasi-static rates, which requires long gauge length and (ii) maintain uniaxial stress equilibrium during the testing, which is achieved by reducing the gauge length” (Ulacia, Salisbury, Hurtado, & Worswick, 2011). The standard ASTM specimen is specified in ASTM standards A8/A8M and A370. The University of Waterloo specimen design was then scaled up by 1.2x, as shown in Figure 32, to fit the 19.05 mm diameter incident and transmission bars being used in this tensile SHPB apparatus. This specimen design also excluded the 6.35 mm holes since the specimen was being held in place between the incident and transmission bars with collar clamps and not with bolts.

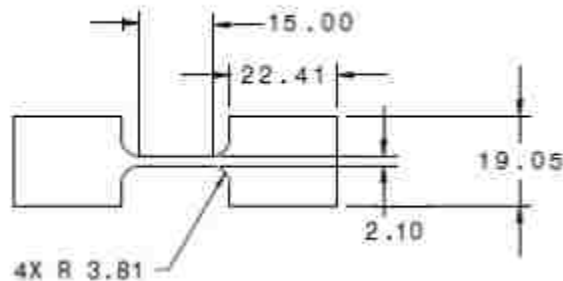


Figure 32: University of Waterloo specimen design modified to fit the new SHPB apparatus

This specimen design was used since the data from this new tensile SHPB apparatus would be compared with the known data obtained from the University of Waterloo's tensile SHPB apparatus using the same batch of DP600 material and specimen design.

3.2.7 Assembly and set-up mechanical components

Assembling the support frame was done by bolting the adjusting feet to the vertical supports, and then bolting the horizontal support bars onto the vertical supports. Once the supports were assembled the I-beams were bolted to the six vertical supports, creating the support frame for the SHPB apparatuses. The support frame was then leveled once located in its final position in the laboratory. The gas gun support and one flat endcap, shown in Figure 33, were attached to the I-beam using shoulder bolts. By using shoulder bolts to attach these two components to the I-beam, the gas gun was locked into place so that it cannot move relative to the I-beam when actuated, and therefore the bar alignment does not change.

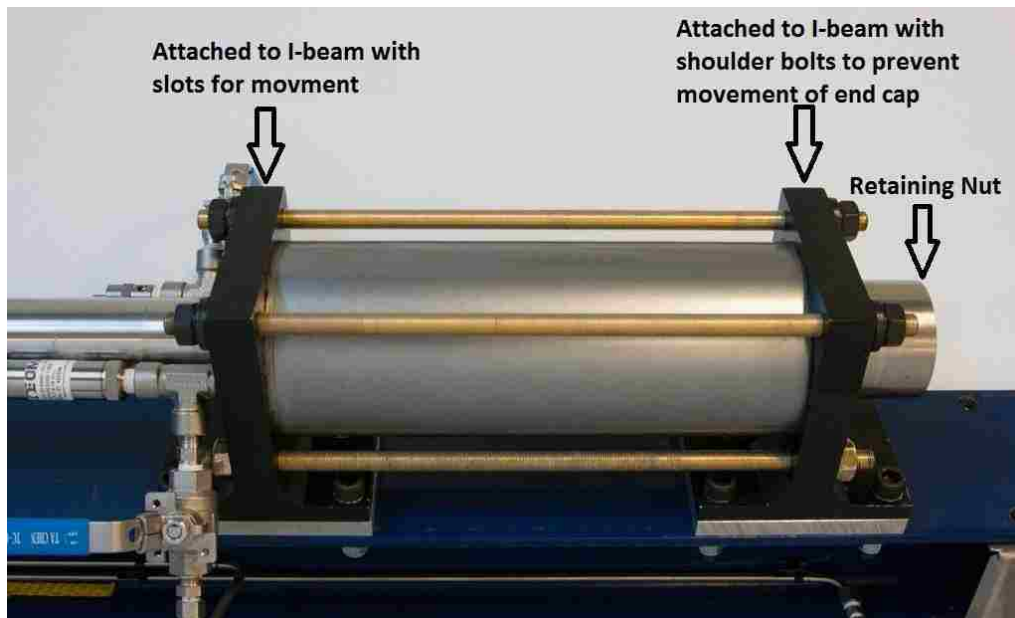


Figure 33: Gas gun showing which mount is attached with shoulder bolts to I-beam

The gun barrel was then attached to the bolted end cap with a retaining nut holding the gun barrel firmly to the flat endcap. The outer thick-wall cylinder was placed over the gun barrel into the groove in the flat end cap. The other flat end cap was slid down the free end of the gun

barrel so as to sandwich the thick-wall cylinder between both end caps. To seal the gas gun's pressure chamber, Permatex Aviation Form-A-Gasket® No. 3 Sealant Liquid was applied to the groove in the endcaps, and between the gun barrel and endcaps. The Permatex Aviation Form-A-Gasket® No. 3 Sealant Liquid "is a slow drying, liquid that changes to a pliable, tacky film through solvent evaporation" (Permatex, 2015), which is designed to seal close-fitting parts and machined surfaces. The flat end caps and thick-wall cylinder are held together with four 12.7mm-diameter threaded rods attached to both flat end caps. After the gas gun was assembled the valve assembly was inserted into the gas gun and the pneumatic cylinder holder was bolted to the I-beam. The momentum trap was then bolted to the I-beam. After the momentum trap, the bar holders were clamped to the I-beam, and the bars were inserted into the bar holders. Alignment of the incident, transmission and the momentum transfer bars was a critical step in the assembly process. The incident bar was aligned coaxially with the gas gun at one end by the cylindrical valve with a tolerance of .025 mm between the incident bar and the cylindrical valve. The cylindrical valve has a transition fit with the barrel. The other end of the incident bar was aligned to the gun barrel's central axis by adjusting the bar support and measuring with a pair of calipers at the four points shown in Figure 34.

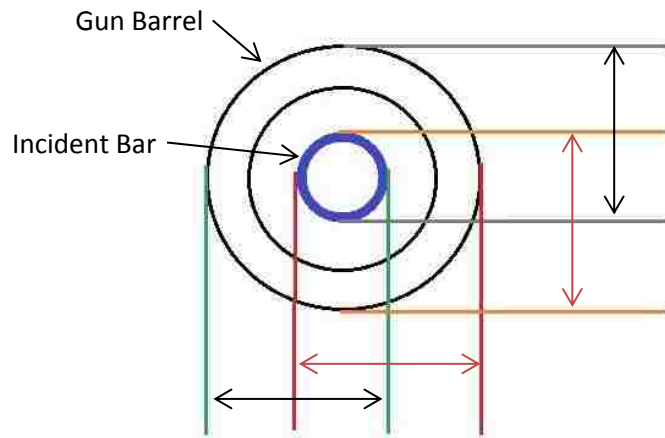


Figure 34: Aligning incident bar to gun barrel centre axis by measuring at different points

There is a tolerance of 0.025 mm between the incident bar anvil and the bar holder. Once the incident bar was aligned, the momentum transfer bar was then aligned with the incident bar. Since one end of the momentum transfer bar shares a support with the incident bar, adjustments were done to the other supports of the momentum transfer bar to align it with the

momentum trap. In order to align the transmission bar, the bar supports were roughly adjusted to get the transmission bar coaxially close to the incident bar. The transmission bar was then finely adjusted to align the specimen slot with the incident bar, so that the specimen fits freely into the slots in both incident and transmission bars.

3.3 Instrumentation

Instrumentation of the tensile SHPB apparatus is necessary for characterization of materials. The instrumentation on the tensile SHPB apparatus is used to obtain information about the stress wave propagating through the incident and transmission bars, the velocity of the striker, and the pressure in the gas gun. Changing the pressure in the gas gun allows the velocity of the striker to be varied. Changing the velocity of the striker, allows different strain rates to be applied to the test specimen, which can be measured through the strain gauges mounted on the incident and transmission bars. Finally, stress and strain data for the test specimen can be determined by post-processing the strain gauge signals.

3.3.1 Strain gauges

With a one-dimensional wave propagating through the bar, the strain at the surface of the bar is the same as the strain in the center of the bar. By using a strain gauge on the surface of the incident and transmission bars, it is possible to measure the amplitude of the incident, reflected and transmitted stress wave. 350 ohm, pre-wired, encapsulated foil strain gauges from Omega (part number: KFG-3-350-C1-11L1M2R) were installed on the bars. These strain gauges have a gauge length of 3 mm and a gauge factor of $2.09 \pm 1.0\%$. The strain gauges were attached to the incident and transmission bars using Omega TT300 cement, which is a heat-cured, 2-part epoxy adhesive. The strain gauges were located 450 mm from the end of the bars, which is more than one wave length from the specimen slot, to ensure that the reflected stress wave does not overlap the incident stress wave. Two strain gauges were mounted to each bar, diametrically across from each other. This arrangement of pairs of strain gauges when wired into the Wheatstone bridge as indicated in Figure 35, compensates for any bending strain that may be induced in the bars and doubles the output of the strain gauge.

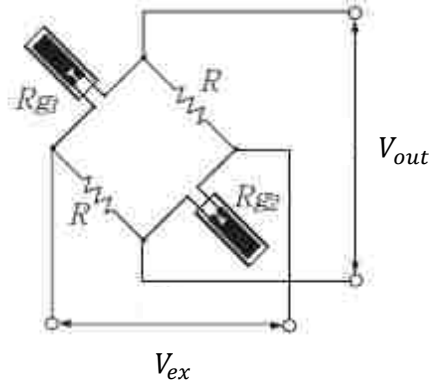


Figure 35: Strain gauges wired into the Wheatstone bridge (Kyowa, 2015)

With this Wheatstone bridge configuration, the output voltage can be converted to strain by:

$$\varepsilon = \frac{2 * V_{out}}{V_{ex} GF} \quad (3.4)$$

The output of the Wheatstone bridge is amplified by a Burr-Brown INA129 instrumentation amplifier. The instrumentation amplifier is set to a gain of 106, which multiplies the output signal of the Wheatstone bridge by 106. The Burr-Brown INA129 instrumentation amplifier at a gain of 100, has an max accuracy of 0.5%, with a typical accuracy of 0.05% (Texas Instruments, 2005). At a gain of 100 the Burr-Brown INA129 instrumentation amplifier has a bandwidth of 200 KHz.

3.3.2 Pressure Transducer

An Omega MMG1.0KV10P3C0T3A5CE pressure transducer, with a pressure range of 0 to 6895 kPa, an output signal of 0 – 10 VDC, with an accuracy of +/- 0.08% is used to measure the pressure in the gas gun pressure chamber. By controlling the pressure inside the pressure chamber, the striker velocity can be determined from an equation derived from calibration of the gas gun. The calibration of the gas gun was carried out by varying the pressure in the gas gun in small increments and recording the velocity of the striker for each pressure level. The tests were repeated in order to obtain a statistical average of the striker velocity at each pressure increment, then plotted to obtain a curve similar to those in Figure 25.

3.3.3 Striker Velocity

It is important to know the striker velocity, since it determines the strain rate in the test specimen. The strain rate can be calculated from equation 2.59. The velocity of the striker is measured using two optical gates placed at a distance of 0.05 m apart. The time difference (Δt) between the activation of each optical gate, and the known distance (D) between the gates allows the velocity of the striker to be calculated using:

$$v_{st} = \frac{D}{\Delta t} \quad (3.5)$$

The second optical gate is aligned with the face of the anvil on the incident bar. This placement of the second optical gate allows the velocity at impact to be recorded.

3.3.4 Start data acquisition signal

With the entire test taking place in less than 100 ms, an electrical signal is needed to start the data acquisition processed. A micro-switch is activated by the valve assembly collar, as shown in Figure 36, to output a +5V signal to the data acquisition system. This output signal, commonly called a TTL signal, is either 0V or +5V.

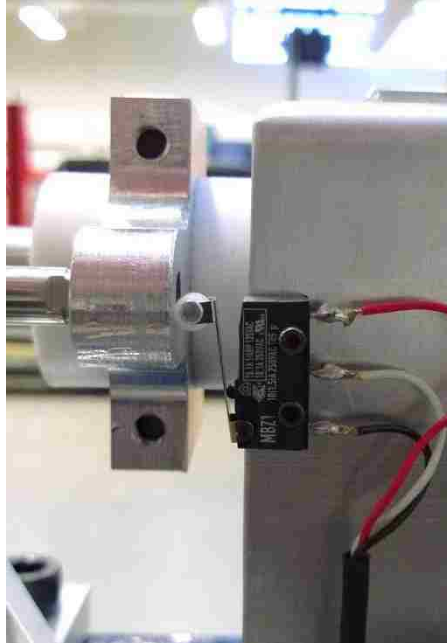


Figure 36: Micro-switch location on SHPB apparatus

The signal from the micro-switch is used to start the data acquisition by the digitizer, to obtain the striker velocity and to record the pressure in the gas gun at firing.

3.3.5 Data acquisition

In order to record the various signals from the strain gauges, pressure transducer, micro-switch, and striker timing gate, a data acquisition system is required. The data acquisition system dedicated to this SHPB apparatus is a National Instruments PXIe-1082 8 slot chassis, shown in Figure 37, populated with a PXIe-8135 Core i7-3610QE 2.3 GHz Controller card, a PXIe-6361 X series data acquisition card and a PXI-5105 digitizer card.

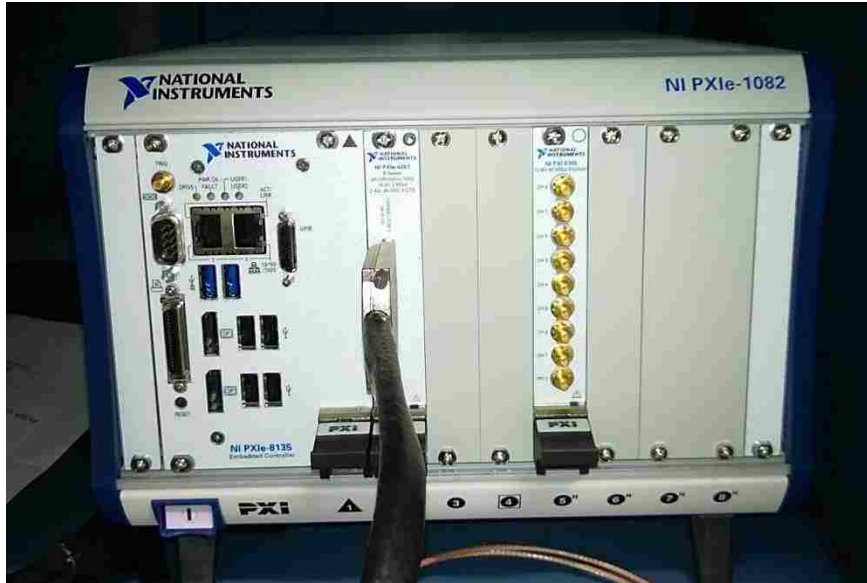


Figure 37: National Instruments data acquisition system

The PXIe-6361 card is used to read the pressure transducer, the time pulse from the striker velocity optical gate, and the TTL voltage signal from the micro-switch. The signals from the pressure transducer, optical gate and the micro-switch are sent to the PXIe-6361 card via a NI SCB-68A shielded I/O connector block. The SCB-68A provides a, “very low-noise signal termination” (National Instruments, 2015) and it is easy to attach the signal wires to. The PXI-5105 digitizer card is used to read the amplified signals from the Wheatstone bridge. Information about the two cards used for data acquisition is presented in Table 5.

Table 5: Information about the data acquisition cards (National Instruments, 2015)

Data acquisition card	Maximum Sample Rate	ADC Resolution	Number of analog input channels	Number of analog output channels	Number of digital input/output channels
NI PXIe-6361	2 MS/s	16 bit	16	2	24
NI PXI-5105	60 MS/s	12 bit	8	N/A	N/A

Table 6 gives the maximum range and accuracy, at that range, of the two data acquisition cards.

Table 6: Range and accuracy of the two data acquisition cards (National Instruments, 2015)

Data acquisition card	Range	Accuracy
NI PXIe-6361 Analog Input Maximum Voltage Range	+/- 10V	Absolute accuracy at full scale: $\pm 1.66 \text{ mV}$
NI PXI-5105 Input Impedance 1 M Ω Maximum Voltage Range	+/- 15 V	DC Accuracy at full scale: $\pm(0.75\%*\text{Reading}+0.25\% \text{ of FS}+600\mu\text{V})$

The PXI-5105 card has a maximum bandwidth of 60 MHz, and an optional 24MHz anti-aliasing filter. The National Instruments PXIe-8135 Controller card is a computer running Windows 7 Pro™ operating system, with National Instruments' NI-DAQmx and LabVIEW 2014 software to interface with the two data acquisition cards. Once the test data is collected it is saved in an Excel file for post-processing after the test is completed.

3.3.6 Assembly and set-up electrical components

The National Instruments PXIe-1082 chassis and data acquisition cards are placed inside a computer cabinet, shown in Figure 38. The computer cabinet is a secure and dedicated location in which to place the DAQ system, keyboard, mouse, monitor and cabling needed to connect the various instruments to the DAQ system.



Figure 38: Computer cabinet for storing DAQ system

Once the strain gauges were attached to the incident and transmission bars 450 mm from the ends of the bars, they were clamped while being heated to 80°C to cure the adhesive for four hours. After cooling to room temperature and removing the clamps, the strain gauges were then heated to 120°C for six hours to stress relieve them. The strain gauges were then wrapped in electrical tape, as shown in Figure 39, to protect the strain gauges and provide strain relief for the wires.



Figure 39: Strain gauge wrapped with electrical tape

The strain gauges were then wired into their separate half-bridge Wheatstone bridges, and the cables were run back to the DAQ system.

The pressure transducer was attached to the gas gun by a tee fitting installed on the flat endcap as seen in Figure 40.

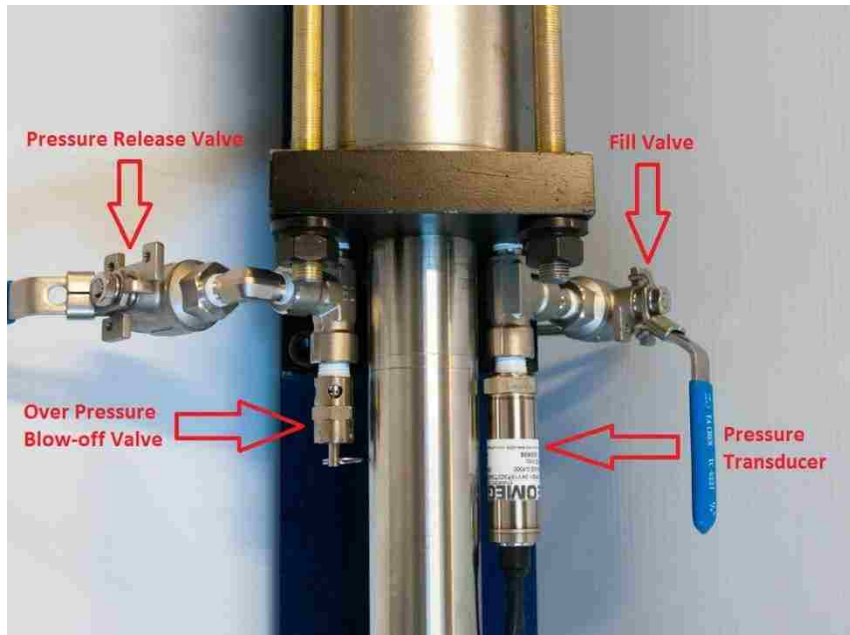


Figure 40: Valve configuration on gas gun

The striker velocity optical gate was installed on the end of the gun barrel as shown in Figure 41.



Figure 41: Optical gate to measure striker velocity

The micro-switch was installed by the valve assembly of the gas gun. Whenever the valve opens the micro-switch triggers the data collection by the DAQ system. The data wires are run separately from the power wires to the equipment and into the computer cabinet, so as to minimize noise on the data wires.

Chapter 4: Calibration, Operation and Data Analysis of a SHPB

4.1 Calibration of the gas guns velocity versus pressure

The gas gun was calibrated by taking five measurements of the velocity of the striker at various firing pressure values. The five measurements of each pressure and velocity were averaged to get the mean value of the pressure and velocity of the striker at the different pressure settings. The only difficulty was to manually set the same pressure each time a test was repeated. Table 7 summarizes the mean values of the firing pressure of the gas gun and the striker velocity. Table 7 also includes the standard deviation for both the pressure and velocity measurements.

Table 7: Average striker velocity and firing pressure of the gas gun

Mean		Standard Deviation	
Pressure (kPa)	Velocity (m/s)	Pressure (kPa)	Velocity (m/s)
0.00	0.00	0.00	0.00
76.97	4.58	1.95	0.65
145.91	9.60	3.49	0.51
212.26	12.56	2.25	0.25
279.97	14.96	3.73	0.31
349.08	16.98	2.25	0.21
419.96	18.94	2.62	0.34
488.69	20.49	2.26	0.23
557.81	22.13	4.48	0.37
625.69	23.60	5.30	0.20
691.25	24.99	4.98	0.26

The average deviation of the velocity of the striker was ± 0.333 m/s. The average deviation of the pressure was ± 3.33 kPa. The mean values for the gas gun firing pressure and velocity of the striker were plotted with the theoretical velocity values derived from equation 3.1. Figure 42 shows that the theoretical values correlate reasonably well with the experimental data.

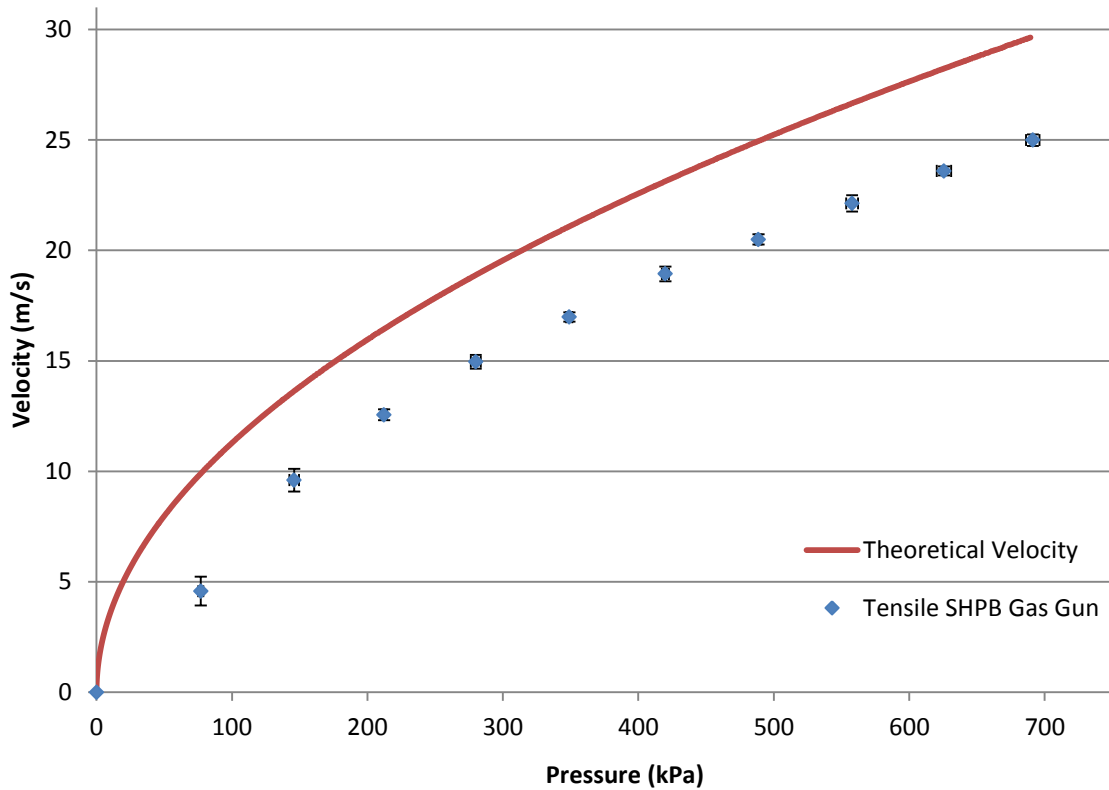


Figure 42: Velocity of striker vs. firing pressure of gas gun

In Figure 42 it can be seen that the measured velocities are consistently lower than the theoretical velocities; this is because friction between the barrel, the striker, and the air resistance the striker is subject to are not accounted for in the theoretical equation.

It is useful to establish an equation that correlates the striker velocity to the firing pressure of the gas gun, so that the strain rate can be selected using equation 2.59. Therefore, the pressure versus velocity data from Table 9 was plotted and a trendline equation was fitted to the experimental data, as shown in Figure 43.

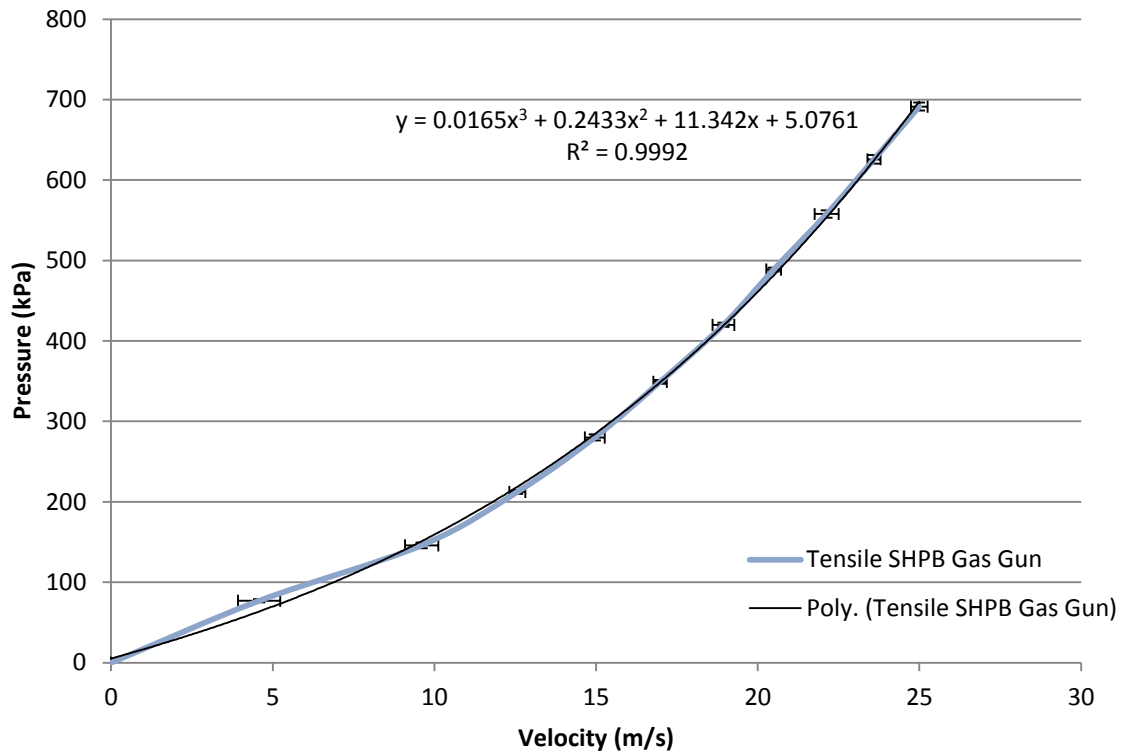


Figure 43: Pressure of gas gun vs. velocity of striker

The trendline equation extrapolated from the graph is:

$$y = 0.0165x^3 + 0.2433x^2 + 11.342x + 5.0761 \quad (4.1)$$

The velocity calculated in equation 2.59, can be inserted as variable x , in equation 4.1 to get the pressure, y , required in the gas gun in order to achieve the desired striker velocity. It was found during the calibration of the gas gun that the anvil on the incident bar and the anvil on the momentum transfer bar had come loose. The Loctite threadlocker Blue 242 had failed and was replaced with Loctite 648 Retaining Compound. It was also noted that the gas gun was not holding pressure. Taking out the valve assembly it was found that the sealing O-rings were damaged. The damage was most likely from the openings in the gun barrel to the pressure chamber. This pressure drop was slow and was taken into account during the calibration by filling slightly over the desired pressure and activating the gas gun at the desired pressure.

4.2 Calibration of the strain gauge output

The strain gauge signal goes through the Wheatstone bridge, out to the INA129 instrument amplifier into the PXI-5105 card as shown in Figure 44.

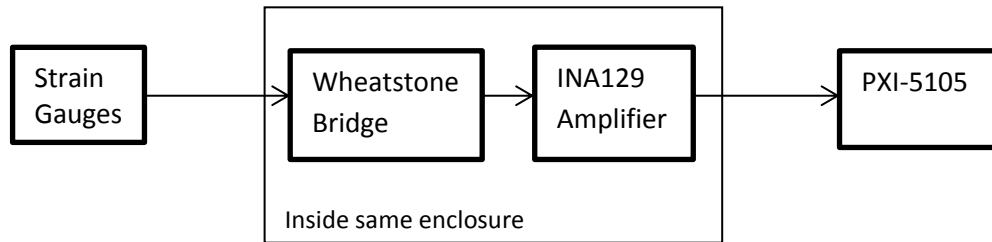


Figure 44: Path for strain gauge signal

The Wheatstone bridge has a voltage equalization circuit, shown in Appendix B, which is designed to eliminate the error that might be present in the strain gauge and the completion resistors of the Wheatstone bridge. The INA129 instrumentation amplifier error and the Wheatstone bridge error are much smaller than the error from the PXI-5105, and therefore the PXI-5105 is considered the main source of error for the strain gauge signals. The calibration of the strain gauges mounted on the incident and transmission bars was carried out with a LC305-20K miniature load cell connected to a DP-41-S-A strain meter. The accuracy of this miniature load cell was first verified using a MTS Criterion model 45 universal testing apparatus (having a calibrated load cell itself): the LC305-20K load cell was subject to increasing compressive forces up to 19,250 N in the MTS test machine, as shown in Figure 45, and it was found that the readings on the strain meter varied by less than 100 N from the readings on the MTS tester, which is within the MTS testers 1% force accuracy (MTS , 2015).



Figure 45: MTS tester applying a load on the LC305 load cell

In order to calibrate the strain gauges on the incident and transmission bars, the LC305-20K load cell was placed against the momentum trap which is fixed to the I-beam, as shown in Figure 46. The slots in the incident and transmission bars were filled and the bars were connected with a sleeve which kept the contacting faces of the incident and transmission bars aligned when the load was applied to the transmission bar. A jack screw was set up between the free end of the transmission bar and a steel block clamped to the I-beam so as to be able to apply an axial compressive force on the transmission bar, as shown in Figure 47. Since the change in electrical resistance in a strain gauge is similar in compression or in tension, the strain gauges can be calibrated in compression even though the incident and transmission bars of this SHPB apparatus will generally be loaded in tension.

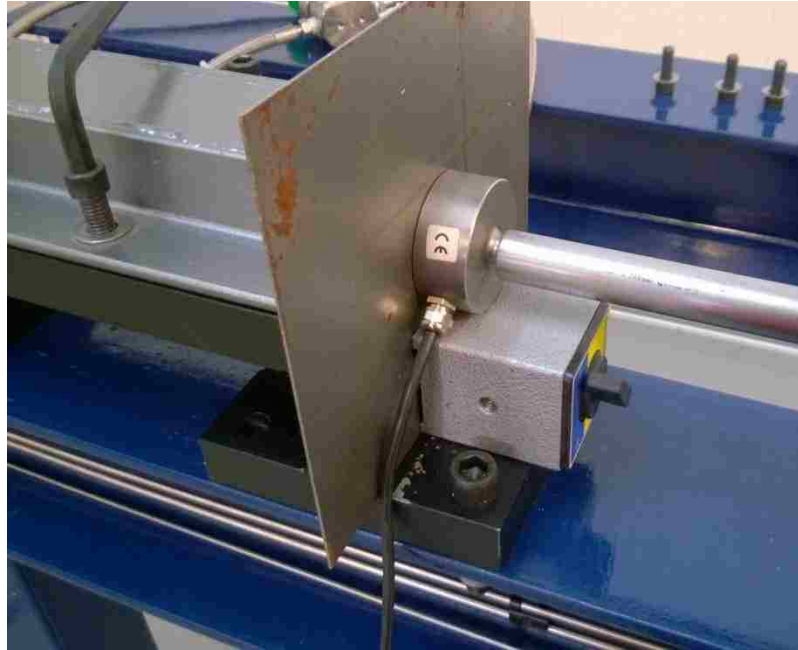


Figure 46: Load cell placement for calibrating strain gauges



Figure 47: Set up of jack screw used to apply a compressive load on the bars for calibration of strain gauges

In the strain gauge calibration procedure, the jack screw was used to apply load increments up to a maximum load of 6583.1 N. The maximum load was limited due to the risk of buckling the transmission bar under the static load and because the clamped steel block would start to move relative to the I-beam when the load exceeded a certain limit. The output voltages from the

Wheatstone bridges were measured through the PXI-5105 digitizer at the various load levels, and Ch0 represents the strain gauges on the incident bar and Ch1 the strain gauges on the transmission bar. The error calculated for the readings on the PXI-5105 were 0.0031 mV. The PXI-5105 gives a large error percentage at low readings, but the error percentage decreases as the readings get closer to full scale values on the PXI-5105. The measured voltage values from the strain gauges can be compared with the theoretical voltage values (or strains) that would be calculated for different values of applied force. The theoretical force is obtained by multiplying the stress (equation 2.3) by the cross-sectional area of the striker. The theoretical output voltage from the Wheatstone bridge (i.e. the theoretical strain) was calculated by substituting equation 2.4 into equation 3.4 and re-arranging to get the output voltage.

The experimental load and voltage data are presented in Table 8.

Table 8: Experimental data for calibration of strain gauges

Load (N)	Ch0 (V)	Ch1 (V)
66.9	-0.003052	-0.0024332
252.9	-0.0057202	-0.005954
767.7	-0.015065	-0.0151
1708.2	-0.033419	-0.031698
2878.6	-0.055269	-0.053348
3935.4	-0.074998	-0.07354
4578.8	-0.087259	-0.085028
5540.3	-0.10521	-0.10399
6093.5	-0.11461	-0.11442
6356.4	-0.12002	-0.11961

The data measured data for Ch0 and Ch1, and the theoretical data are plotted in Figure 48.

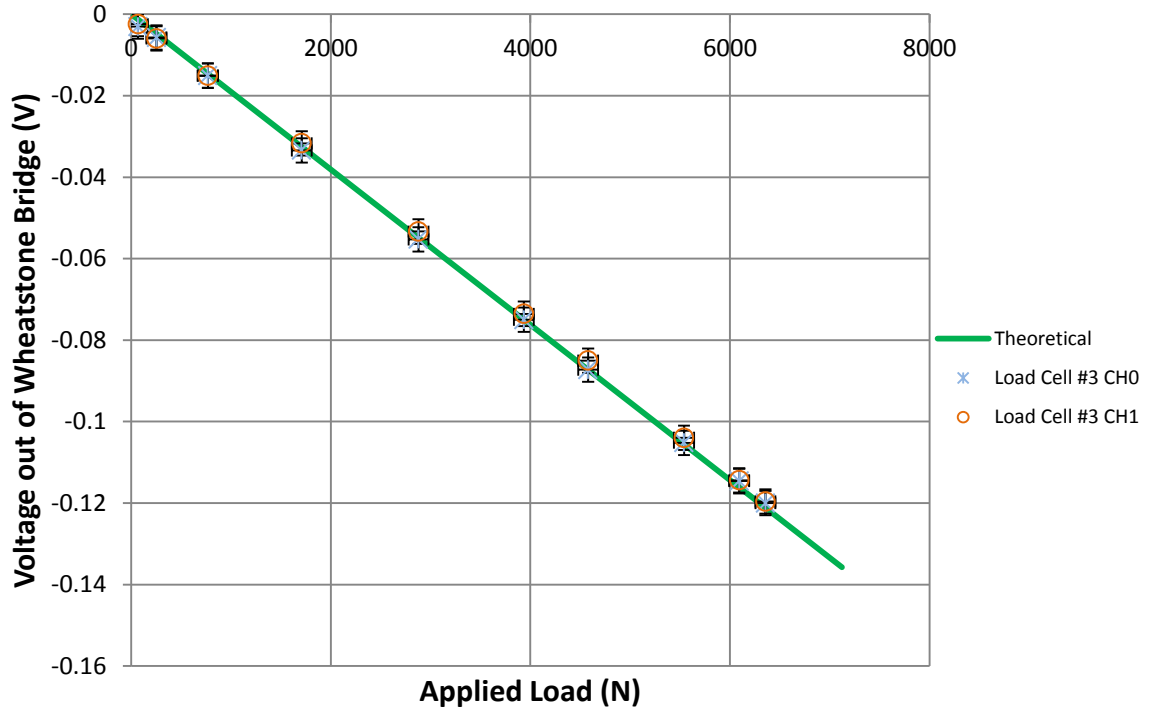


Figure 48: Voltage out of Wheatstone bridge vs. applied load for load cell #3

To compare the difference between the measured and theoretical strain gauge voltage values, the average error was calculated and a validation metric was computed. The average error was calculated from an equation from Audysho et al. (2013), that “represents the average error determined over the entire” (Audysho, Smith, Altenhof, & Patel, 2013) range of values measured.

$$EM = \frac{1}{X_2 - X_1} * \int_{X_1}^{X_2} \left| \frac{y(x) - Y(x)}{Y(x)} \right| dx \quad (4.2)$$

Oberkampf and Trucano (2002) developed a validation metric that compares measured values to computed values at the measured location.

$$VM = 1 - \frac{1}{X_2 - X_1} * \int_{X_1}^{X_2} \tanh \left| \frac{y(x) - Y(x)}{Y(x)} \right| dx \quad (4.3)$$

An advantage of this validation metric is that “first, it normalizes the differences between computational results and experimental data” (Oberkampf & Trucano, 2002). The second

advantage of this validation metric is that “the absolute value of the relative error only permits the difference between the computational results and the experimental data to accumulate” (Oberkamf & Trucano, 2002). A weakness of this validation metric, however, is that it “is inappropriate when any of the $Y(x)$ are near zero” (Oberkamf & Trucano, 2002). Therefore in this evaluation of the strain gauge readings, the first two data points were omitted from the calculation of the error and validation metric due to the values being close to zero and since they have large error percentages due to the digitizer error. The results for the error and validation metric are presented in Table 9.

Table 9: Error and Validation Results

	Error (%)	Validation Metric (V)
Ch0	1.17	0.988
Ch1	2.17	0.978

It is apparent from the analysis of these experimental data that the error percentage is very low and the validation metric is very close to 1.00 for both channels. Therefore the measurements from the strain gauges on both the incident and transmission bars can be considered accurate.

4.3 Operating Procedure

The operation of the tensile SHPB apparatus is quite straightforward, but requires a series of steps to set up the apparatus and to conduct a test. One must take precautions when working around a gas gun to ensure the operators safety. It is advisable to only pressurize the gas gun just before a test is to be conducted, and to empty any residual pressure immediately after the test is conducted. The following steps should be taken in order to prepare for testing:

- Open the DAQ cabinet, turn on the power bar in the bottom of the cabinet to power the sensors and Wheatstone bridge, then power on the DAQ system.
- Verify that the gas gun pressure release valve, Figure 40, is open and the fill valve, Figure 40, is closed.

- Check the bar supports for any loose hardware, if any bar supports are loose, re-alignment of the bars is required.
- Check that the striker is fully seated up against the gas gun valve.
- Align the incident bar with the velocity optical sensors by aligning the edge of the anvil with the top of the optical gate housing seen in Figure 49.

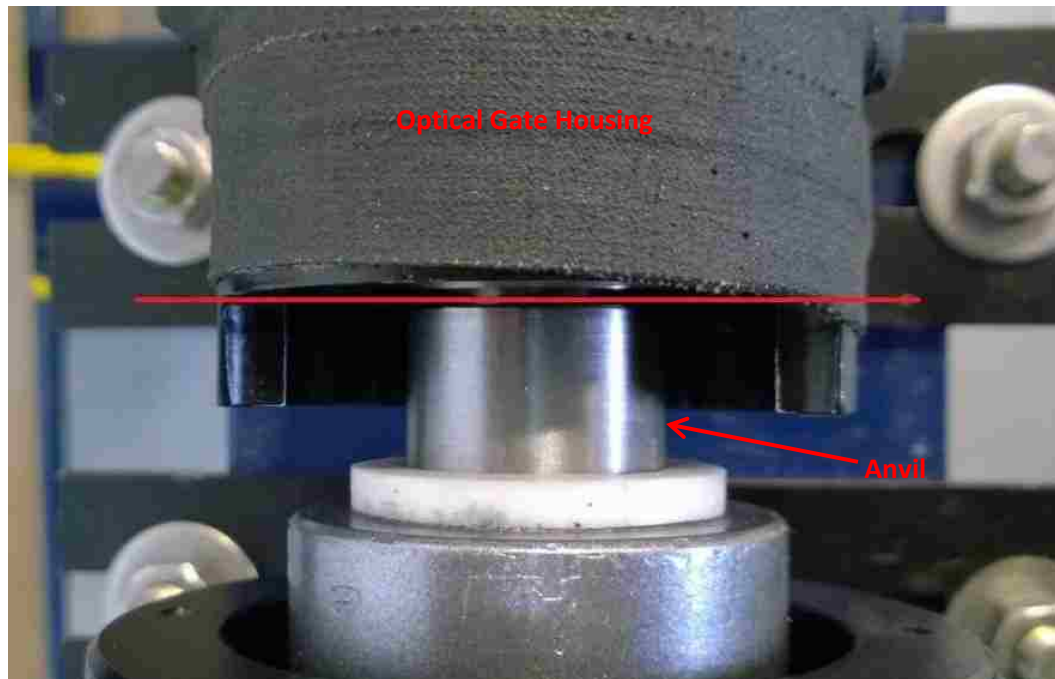


Figure 49: Alignment of incident anvil and optical gate housing

- Set the momentum trap cap pressure by tightening the screws, the higher the striker velocity the more pressure is required for the momentum trap cap. If the pressure on the momentum cap is too high the test specimen will not break; if it is too low the whole SHPB apparatus will be subject to a shock, which could affect the bar alignment or maybe even damage the bars.
- Connect the shop airline to the fitting for the pneumatic valve actuators, shown in Figure 50.

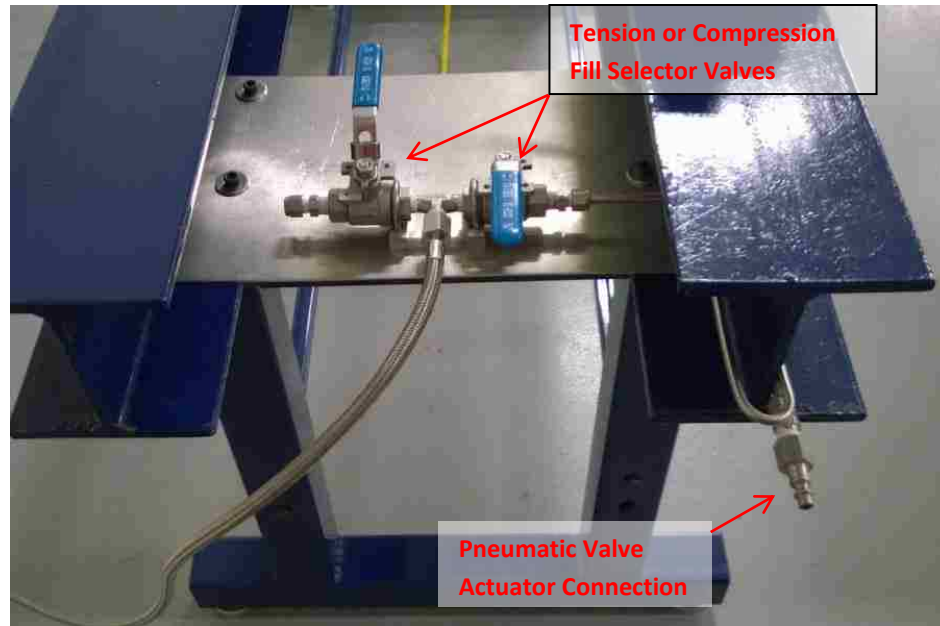


Figure 50: Valve actuator connection and fill selection valves

- Open nitrogen tank valve a quarter turn.
- Set pressure regulator for just over the maximum pressure calculated for the test.
- Open fill selector valve for either tension or compression, shown in Figure 50, depending on which SHPB apparatus is appropriate (the tension and compression SHPB systems are side-by-side on two different I-beams).
- Insert a test specimen into the incident bar and tighten the collar clamp; check that the specimen is not crooked and is fully inserted into the specimen slot.
- Insert the other end of the test specimen into the slot in the transmission bar; check that the specimen is fully inserted into the slot and tighten that collar clamp. It is very important not to twist the test specimen when tightening the collar clamps. When tightening collar clamp bolts, alternate between the two bolts and increase the bolt tightness incrementally.
- On the DAQ, open up LabVIEW 2014 software, and then open TensileSHPB.vi for the tensile SHPB apparatus.

The following steps should be taken in order to conduct a SHPB tensile test:

- Start the LabVIEW virtual instrument (vi) program to see the pressure in the gas gun pressure chamber.
- Close the pressure release valve, shown in Figure 40, and open the fill valve, shown in Figure 40, to increase the pressure in the gas gun pressure chamber to the value calculated from equation 4.1.
- Stop the LabVIEW vi, and click the switch to change the vi over to the data collection mode, and restart the vi.
- Open the gas gun valve by moving the lever shown in Figure 51.

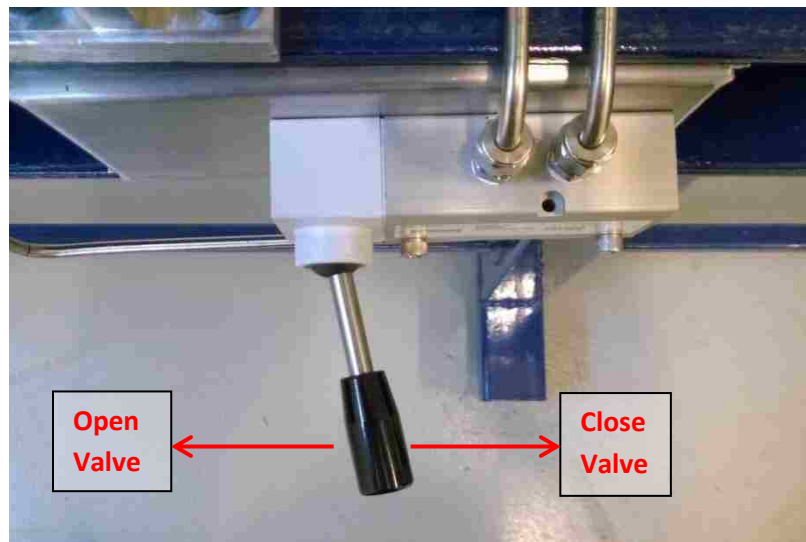


Figure 51: Valve pneumatic actuator controller

- Right click on graph in the vi and export the data to excel.
- Add the velocity and pressure data to the excel worksheet, and save the file.
- Open the gas gun pressure release valve (see Figure 40).

When finished with testing for the day:

- Open the gas gun pressure release valve.
- Close the gas gun fill valve.
- Disconnect the shop airline to the fitting for the pneumatic valve actuators.
- Close the nitrogen tank.

- Close the fill selector valve.
- Power down the DAQ and turn off the power bar.
- Close and lock up DAQ cabinet.

It is important for the SHPB operator to secure the SHPB apparatus, so that other people will not be hurt if they are in the lab area around the SHPB apparatus when the SHPB operator is not present.

4.4 Signal processing

A tensile SHPB tests generates a data set that is exported as an Excel worksheet and consists of thousands of rows of voltage data, recorded at a sampling rate of 60 million data per second. In order to post-process this data file, a MATLAB program provided in Appendix C, was written to calculate the true stress and corresponding true strain data for a given test specimen. The MATLAB data processing program executes the following operations:

- The program requires the user to select the data file to be processed using a graphical user interface, and then loads the output voltage data from the incident and transmitted strain gauges into the program.
- The output voltage data from the strain gauges are then divided by the amplification factor and then converted into micro-strain using equation 3.4.
- The initial strain gauge voltage readings are plotted as a graph, shown in Figure 52, for the user to see the initial offset of the signals.

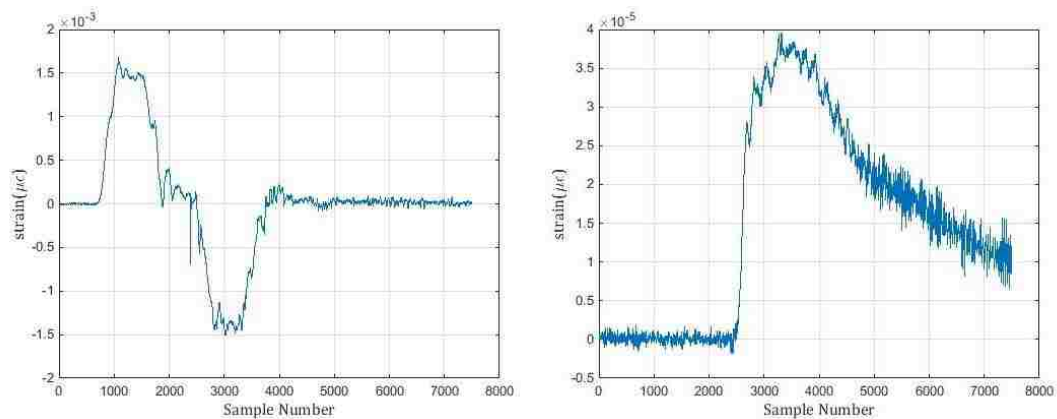


Figure 52: Example of initial strain vs. count graph for the incident and transmission bars

The initial strain gauge voltage readings might be slightly off zero, due to environmental factors (such as ... room temperature). Adding or subtracting microvolts to the entire data set so as to ensure the initial strain value is zero is easier to do with the software after the test than trying to precisely adjust the strain gauges to zero prior to the test, because the amplifier greatly increases the sensitivity of the adjustment.

- The data is then optionally filtered using a digital filter. The digital filter creates a low-pass infinite impulse response filter from the specified passband frequency and filter order number. The passband frequency denotes the upper limit of the low-pass filter and the order number represents how fast the filter attenuates the magnitude of the signal after the passband frequency. The higher the order number is the faster the signals magnitude is attenuated above the passband frequency; this can be seen between Figure 53 and Figure 54.

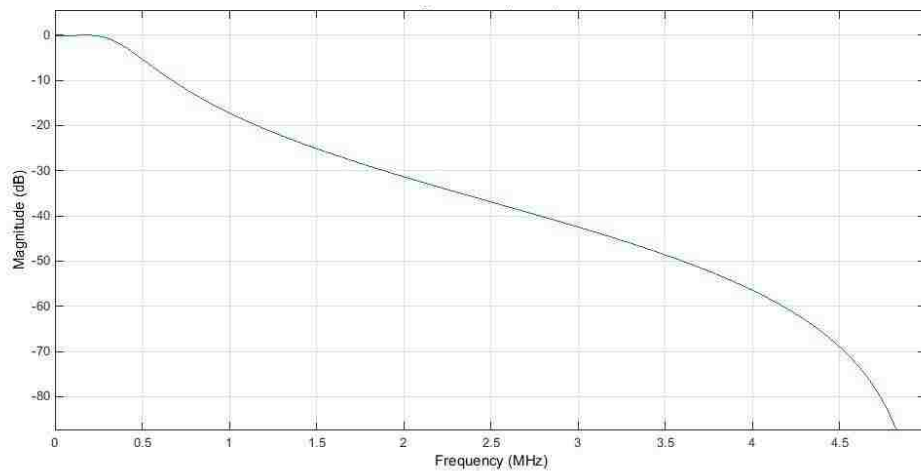


Figure 53: 250 kHz, 2nd order lowpass filter

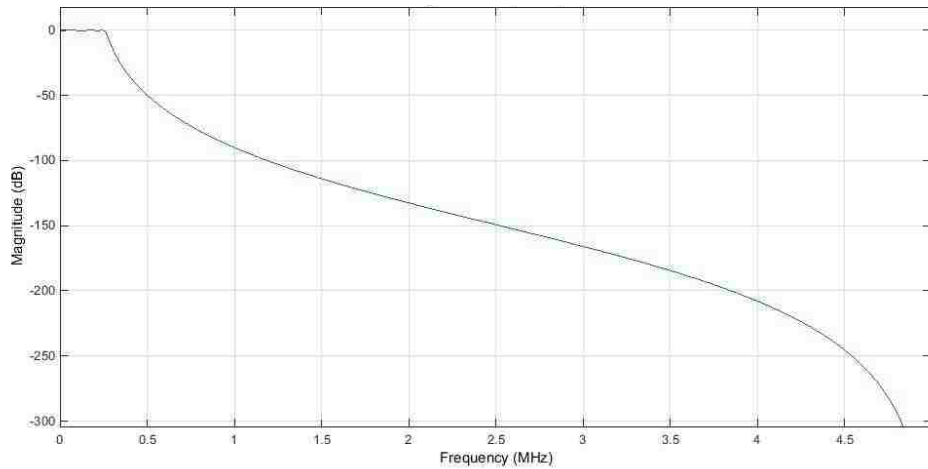


Figure 54: 250 kHz, 6th order lowpass filter

The initial settings for the digital filter provide a filter bandwidth of 250 kHz which is greater than the bandwidth of the INA129 instrumentation amplifier and eliminates noise from the signal as seen in Figure 55.

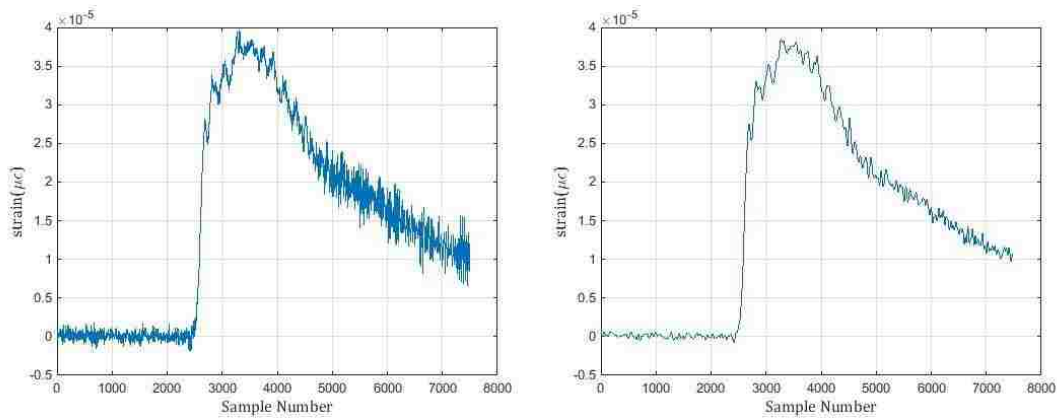


Figure 55: Unfiltered and filtered transmission bar strain gauge output

- The filtered data is plotted on two graphs, one for the incident bar data and one for the transmitted bar data. If the filtered data is acceptable to the operator, it is accepted and the user then moves on to select the start point and end point of the incident pulse. If the user does not want to filter the signal at all, the passband frequency is set to 5 MHz, the maximum passband frequency of the digital filter.

- By zooming in on the incident bar graph the sample number of the start and end points of the incident pulse can more accurately be selected. On the incident bar graph the sample number of the start of the reflected pulse is also found. The graph of the transmitted data is used to get the sample number for the start of the transmitted pulse. The number of sample points that the incident pulse covers is the same number of sample points used for the reflected pulse and the transmitted pulse.
- The incident pulse and inverted reflected pulse are plotted on the same graph so that the user can alter the start point of the incident pulse to align up the incident and reflected pulses, as shown in Figure 56.

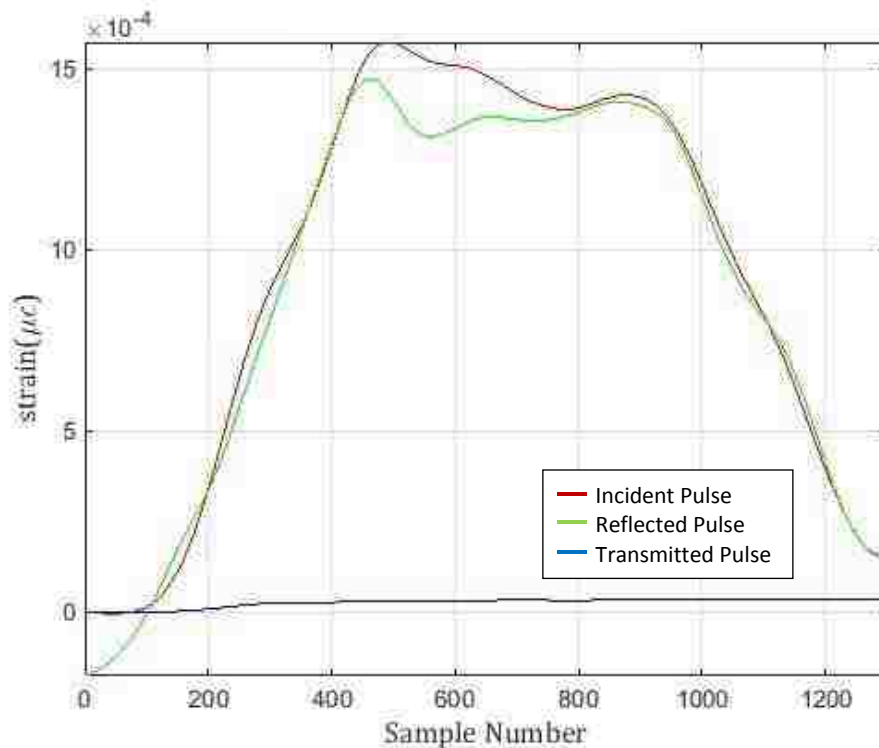


Figure 56: alignment of the incident and reflected pulses

- Once the user is satisfied with the incident start and end points and the reflected and transmitted start points, the engineering strain is calculated from equation 2.09 and 2.15. Equation 2.09 gives the average strain of the specimen without assuming the specimen uniformly deforms as equation 2.15 does, during the test. Comparing the results of equation 2.09 and 2.15 graphically shows that there is not much variation

between the two equations in the elastic region and minor variation as the strain increases in the plastic region.

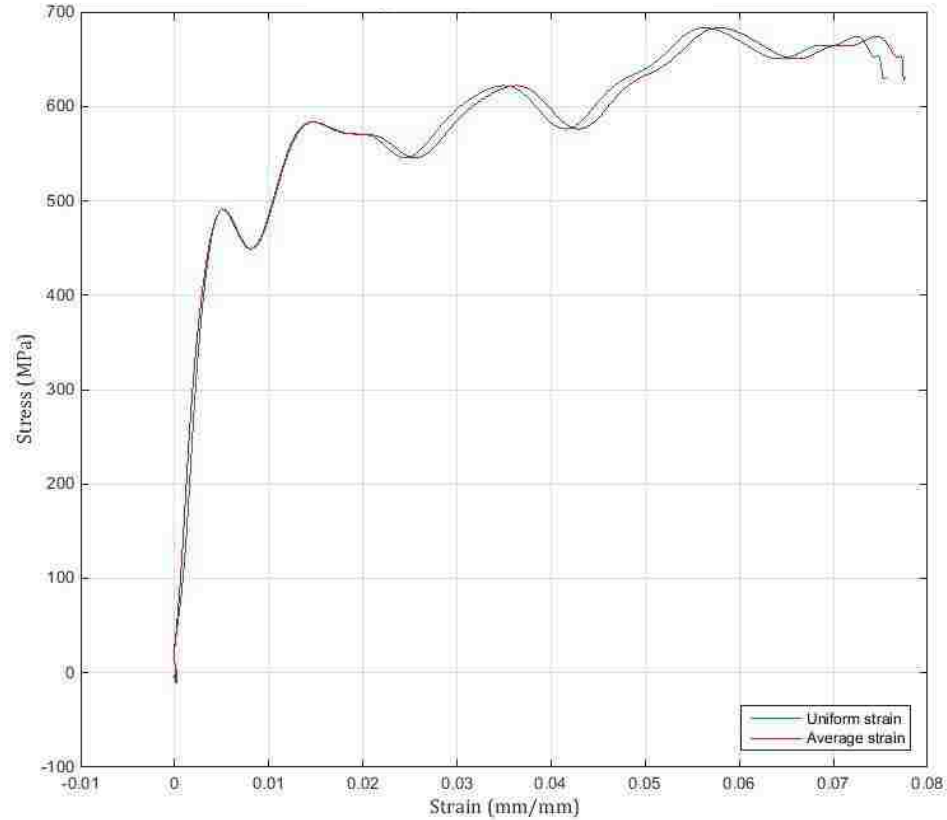


Figure 57: Engineering stress versus strain for uniform and average strain

The engineering stress is calculated from equation 2.16.

- The true stress and strain are calculated from:

$$\epsilon_{true} = \ln(1 + \epsilon_u) \quad (4.4)$$

$$\sigma_{true} = \sigma_u * (1 + \epsilon_u) \quad (4.5)$$

- The engineering stress versus engineering strain, the true stress versus true strain, the strain rate versus time, and the true strain versus time are graphed on separate graphs so the user can see the data visually. An example of the graphs plotted is shown in Figure 57 and Figure 58 .

- The strain rate is calculated from the slope of the true strain versus time graph.

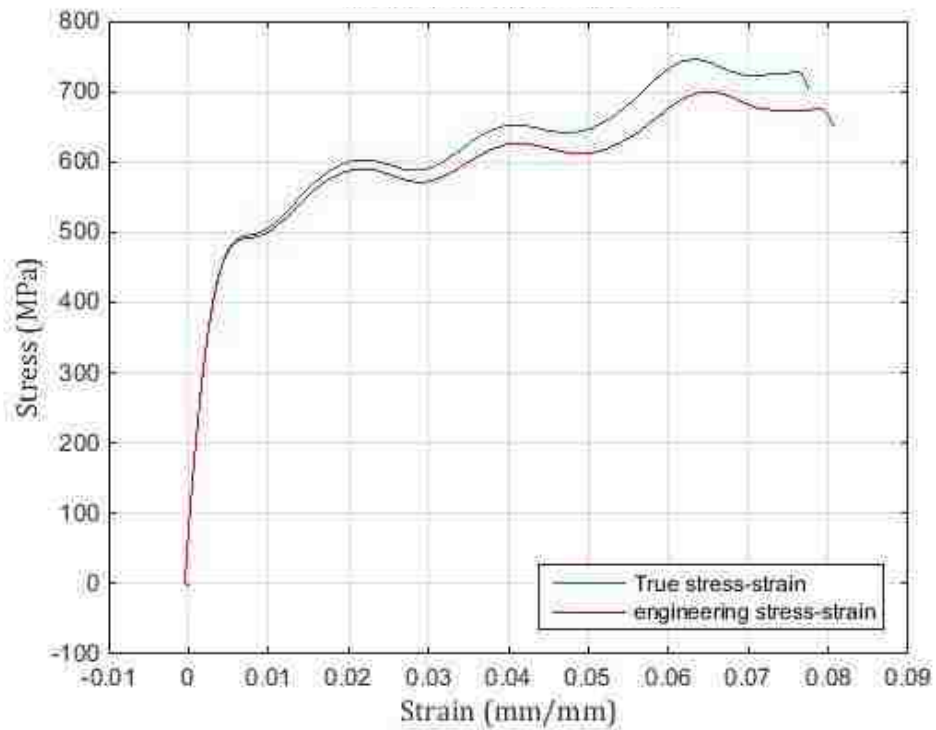


Figure 58: Example of the true stress-strain versus engineering stress-strain

- The user then has the option to save the data to an excel file. This excel file contains the engineering stress and strain data, the true stress and strain data and the strain rate data.

The MATLAB code developed for post-processing the experimental data from the SHPB tests yields a dynamic flow curve for the specimen tested.

Chapter 5: Experimental testing of DP600 Sheet Steel

5.1 High strain Rate flow behaviour of DP600 sheet steel

The tension SHPB apparatus that has been described in the previous chapters will now be used to perform some high strain rate tensile tests on a DP600 sheet material. This steel sheet material has been tested within the framework of another research project, and in particular, it's high strain rate behaviour was characterized at the University of Waterloo. This research team at the University of Waterloo is world-renowned in the field of high strain rate testing and has published extensive experimental data obtained with their own SHPB apparatus. The objective of this chapter is to describe the testing of DP600 sheet using our newly developed SHPB apparatus and compare our results with high strain rate flow curves for this same sheet material obtained at the University of Waterloo and published in peer-reviewed literature [Rahmaan et al., 2014].

5.1.1 Properties of DP600 sheet steel

The SHPB test specimens were taken from DP600 steel sheet material with a nominal thickness of 1.5mm supplied by ArcelorMittal. The chemical composition of the DP600 steel was obtained from ArcelorMittal and is provided in weight percent in Table 10.

Table 10: Chemical composition of DP600 steel in weight percent

C	Mn	P	Si	Al	Cu	Ni	Cr	Mo	V	Nb	Ti
0.11	1.50	0.01	0.18	0.04	0.06	0.02	0.18	0.21	<0.01	<0.01	0.03

Quasi-static uniaxial tension tests were performed on this DP600 steel, as seen in Figure 59

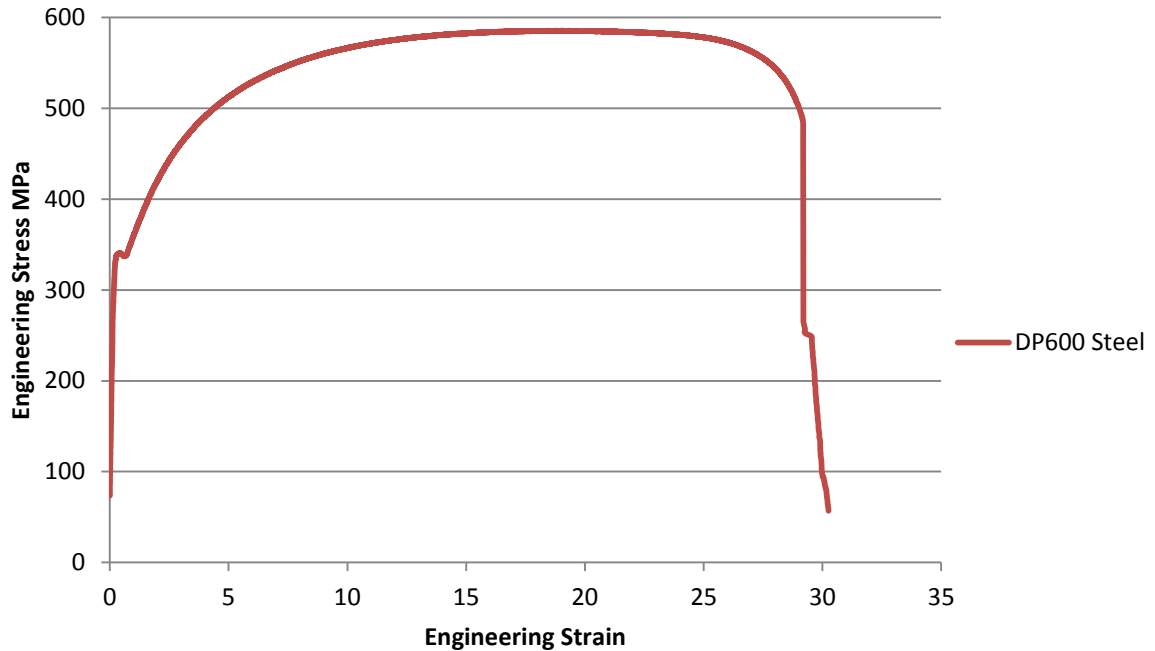


Figure 59: Uniaxial tension test data for DP600 steel

The mechanical properties of the DP600 steel obtained from the quasi-static uniaxial tension tests are shown in Table 11

Table 11: Mechanical properties of DP600 steel

Material	E (handbook) [GPa]	Yield Stress [MPa]	Ultimate Stress [MPa]	n-value [true]	r0
DP600	210	340	587	0.175	0.687

5.1.2 SHPB tests on DP600 sheet steel

In order to achieve a strain rate of 1000 s^{-1} during the SHPB tensile test and a stress of 600 MPa, the striker velocity was calculated to be 15.2 m/s, using equation 2.59. Using equation 4.1, a pressure of 292 kPa in the gas gun pressure chamber was required to achieve this striker velocity.

The PXI-5105 was set to a sampling rate of 10 MS/s so as to collect approximately 7500 data points in the TensileSHPB.vi LabVIEW program. The TensileSHPB.vi LabVIEW program was also set to have a low-pass Butterworth filter of an order of 2, and a 250 kHz cut-off frequency to reduce any signals above this frequency. Since the INA129 instrumentation amplifier has a bandwidth limit of 200 KHz at a gain of 100, any signal above 250 kHz is considered noise and not actually part of the signal.

Testing was conducted in such a way that a test specimen would reach its ultimate tensile strength and fracture. And in order for the test to be valid, the fracture must occur within the specimen gauge length. Furthermore, in order to demonstrate that the specimens did not slip in the bar specimen slots, the edge of the specimen-to-bar interface was marked with a black marker before each test, as shown in Figure 60. Figure 61 shows the specimen-to-bar interface after a test, showing no slipping of the specimen.



Figure 60: Mounted specimen with black marker at bar/specimen interface to show if slipping occurs

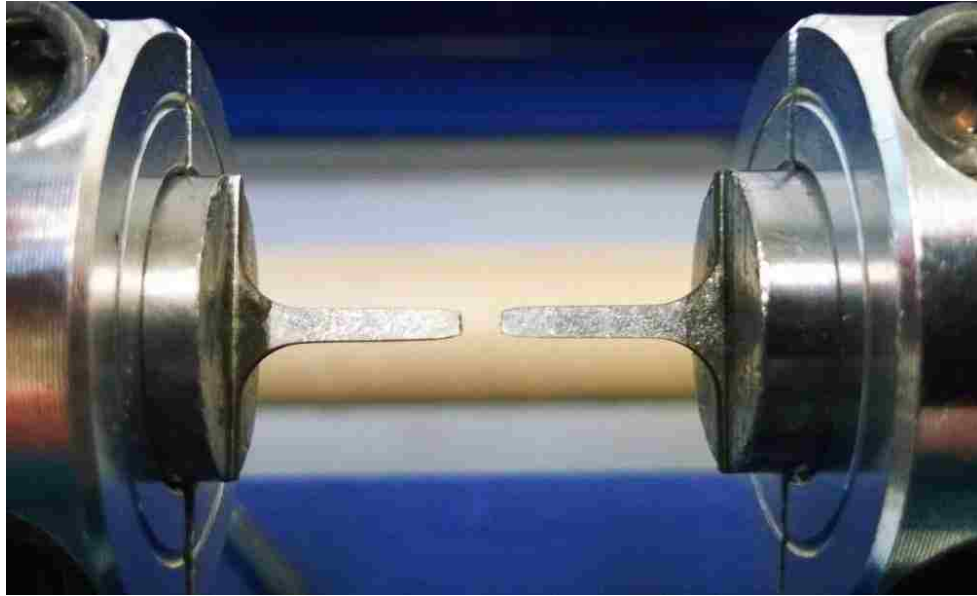


Figure 61: Fractured SHPB specimen with marker at bar/specimen interface showing no slipping

The striker bar was lubricated approximately every 10 tests. And the bar holders and the incident bar and momentum transfer bar anvils were also checked for any looseness every time the striker was lubricated.

5.1.2.1 SHPB test results in the rolling direction

A total of 11 test specimens were tested for the rolling direction. Of the 11 test specimens, eight tests were considered successful. Three tests were considered to have failed, due to the test specimens necking but not fracturing. All test specimens that fractured, had the fracture in approximately the middle of the gauge length, as seen in Figure 62.

Figure 62, also shows that specimens 7, 8, and 9 did not fracture, but did neck in the middle of the gauge length. Three failed test in a row was most likely due to the striker needing to have lubrication re-applied. The striker was lubricated after test specimen 9, and there were no more failed tests. The striker velocity did not indicate that the striker needed to be lubricated, since the striker velocities were still very close to 15.2 m/s.



Figure 62: RD fracture location

The test specimen shown in Figure 63 was bent due to the transmission bar not having a momentum trap and colliding with the stopped incident bar. Not having a momentum trap on the transmission bar was an oversight in the design phase. This oversight could be resolved by adding a hard stop on the I-beam so that the transmission bar does not impact the specimen after the test.

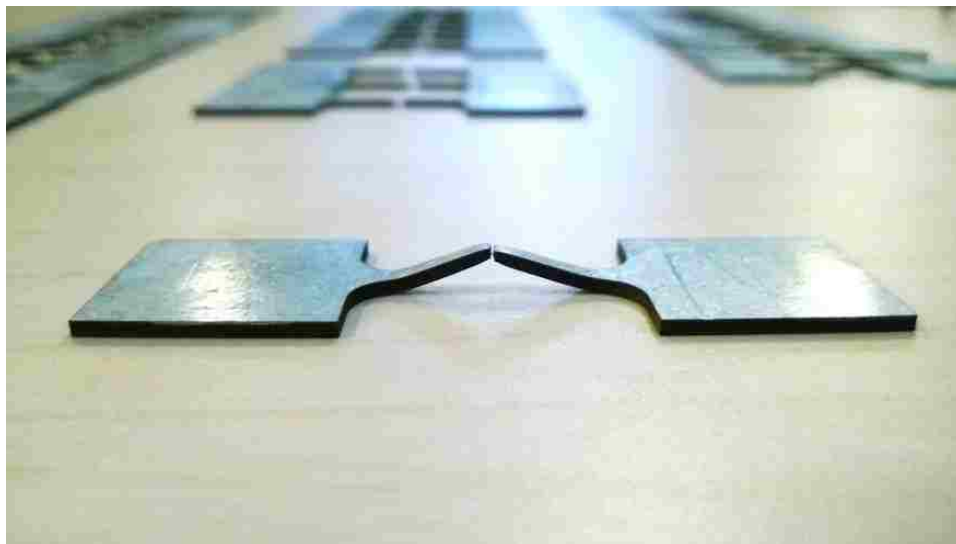


Figure 63: Bent test specimen from transmission bar collision

The gas gun firing pressure and corresponding striker velocity are presented in Table 12 for each tensile test in the sheet rolling direction.

Table 12: Gas gun pressure and striker velocity data for the RD specimens

	Pressure (kPa)	Velocity (m/s)
RD-EX1	299.3	15.16
RD-EX2	296.6	14.82
RD-EX3	295.3	15.10
RD-EX4	294.4	15.29
RD-EX5	296.6	14.89
RD-EX6	296.4	15.37
RD-EX7	297.7	15.05
RD-EX8	296.8	14.91
RD-EX9	299.3	14.92
RD-EX10	299.3	15.32
RD-EX11	298.6	15.10

The average pressure was 297.3 kPa, with a standard deviation of ± 1.7 kPa. The average velocity was 15.09 m/s with a standard deviation of ± 0.19 m/s. The calculated velocity was within the error range of the average striker velocity.

The strain rate calculated for each of the RD specimens is shown in Table 13. The average strain rate for the RD specimens is 1012 s^{-1} with a standard deviation of 33 s^{-1} . The necked specimens were not included in the average and standard deviation calculations.

Table 13: Strain rate for RD specimens

	Strain Rate (s^{-1})
RD-EX1	962
RD-EX2	1064
RD-EX3	1050
RD-EX4	1007
RD-EX5	1003
RD-EX6	996
RD-EX7-Necked	983
RD-EX8-Necked	1017
RD-EX9-Necked	986
RD-EX10	1027
RD-EX11	987

All of the valid tests for the RD are plotted in Figure 64.

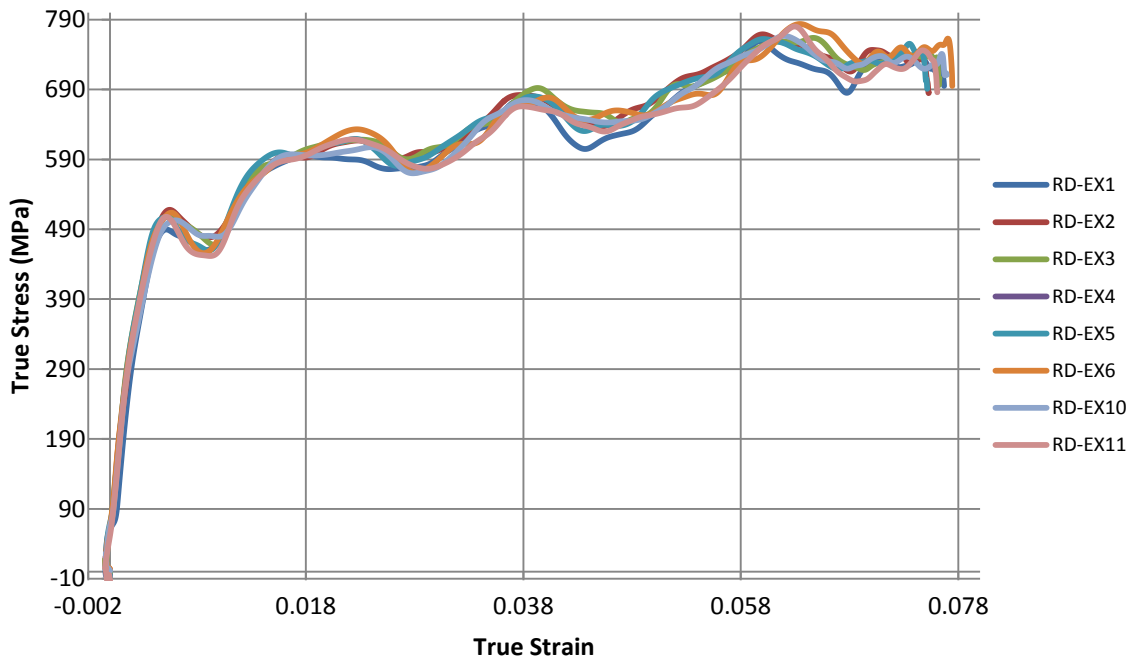


Figure 64: True Stress vs. True Strain curves for all SHPB specimen tested in the RD

From Figure 64 it can be seen that the elastic region of the stress-strain curves are almost identical with very little variation. The oscillations in the plastic region are most likely due to the stress wave not being fully one-dimensional. When the striker impacts the anvil many different frequency components are generated to make up the stress wave. The “higher frequency components travel slower than, C_0 , since phase velocity decreases with decreasing wavelength” (Follansbee & Frantz, 1983). This “difference in wave velocity leads to spreading or dispersion of the initial pulse; the rise time lengthens and oscillations occur” (Follansbee & Frantz, 1983). In order to reduce the oscillations in the incident pulse, the length of the incident bar can be increased to give the stress wave more bar length to disperse. The length of the striker can also be increased so that the stress wave will act over a longer period of time, giving the stress wave more time to disperse. The anvil on the incident bar is also “thought to induce oscillations and lower the rise time of the incident pulse” (Clark, 1993). By changing the shape of the anvil it may be possible to reduce the oscillations in the incident pulse.

5.1.2.2 SHPB test results in the Diagonal Direction

A total of 14 test specimens were tested for the diagonal direction. Of the 14 tested specimens, eleven tests were considered successful. Three tests were considered to have failed, due to the test specimens necking but not fracturing. Once again, the fractures consistently took place approximately in the middle of the gauge length, as can be seen in Figure 65.

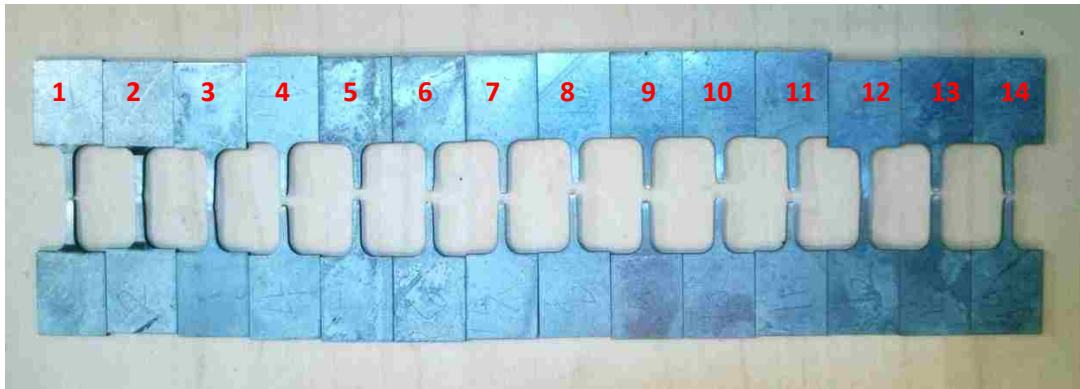


Figure 65: Central fracture location for DD specimens

It can be seen in Figure 67 that specimens 2 and 3 failed to fracture due to the momentum trap being set too tight and stopping the movement of the incident bar too quickly. The gas gun firing pressure and the striker velocity for each of the DD specimens are presented in Table 14.

Table 14: Gas gun pressure and striker velocity data for the DD specimens

	Pressure (kPa)	Velocity (m/s)
DD-EX1	300.4	14.48
DD-EX2	305.3	15.41
DD-EX3	305.5	15.38
DD-EX4	300.8	15.72
DD-EX5	298.4	15.21
DD-EX6	295.1	15.45
DD-EX7	295.5	15.23
DD-EX8	298.6	15.02
DD-EX9	297.7	15.49
DD-EX10	297.5	15.18
DD-EX11	297.1	15.50
DD-EX12	297.5	15.07
DD-EX13	294.2	15.21
DD-EX14	295.1	15.15

The average pressure was 298.5 kPa, with a standard deviation of ± 3.5 kPa. The average velocity was 15.25 m/s with a standard deviation of ± 0.29 m/s. The calculated velocity was within the error range of the average striker velocity.

The strain rate calculated for each of the DD specimens is shown in Table 15.

Table 15: Strain rate for DD specimens

	Strain Rate (s^{-1})
DD-EX1	995
DD-EX2-Necked	992
DD-EX3-Necked	978
DD-EX4	1021
DD-EX5	1098
DD-EX6	998
DD-EX7	1008
DD-EX8	1010
DD-EX9	1000
DD-EX10	1002
DD-EX11	1007
DD-EX12-Necked	952
DD-EX13	1005
DD-EX14	999

The necked specimens were not included in the average and standard deviation calculations. The average strain rate for all the DD specimens is $1013 s^{-1}$ and the standard deviation is $29 s^{-1}$.

5.1.2.3 SHPB test results in the Transverse Direction

A total of 13 test specimens were tested in the transverse direction of the sheet. Of the 13 specimens, 10 tests were considered successful. Two tests were considered to have failed due to the test specimens necking but not fracturing. One test was considered to have failed because the test specimen showed evidence of slipping in the incident bar specimen slot. The specimen showed a shiny area where it moved in the bar specimen slot, as seen in Figure 66.



Figure 66: Sample specimen showing evidence of slipping in bar specimen slot

The fracture consistently occurred approximately in the middle of the gauge length, as can be seen in Figure 67.

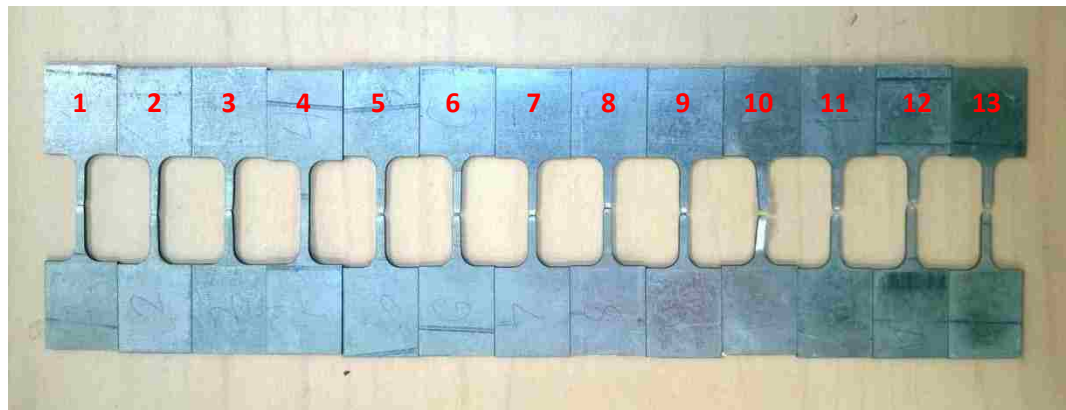


Figure 67: Central fracture location for TD specimens

The gas gun firing pressure and the corresponding striker velocity for the TD specimens are presented in Table 16.

The average pressure was 297.3 kPa and the standard deviation was ± 1.3 kPa. The average velocity was 15.32 m/s with a standard deviation of ± 0.15 m/s. The calculated velocity was within the range of error of the average striker velocity. The velocity of TD-EX2 was not included in the average and standard deviation calculations for the velocity, because this value is erroneous. It was found that when the incident bar anvil covers the second optical gate in the velocity sensor, the computed velocity will be high such as that which was calculated for specimen TD-EX2.

Table 16: Gas gun pressure and striker velocity data for the TD specimens

	Pressure (kPa)	Velocity (m/s)
TD-EX1	296.8	15.37
TD-EX2	298.8	394.54
TD-EX3	296.4	15.12
TD-EX4	298.6	15.54
TD-EX5	299.3	15.13
TD-EX6	295.9	15.43
TD-EX7	296.6	15.14
TD-EX8	297.3	15.43
TD-EX9	296.2	15.25
TD-EX10	297.5	15.47
TD-EX11	296.4	15.29
TD-EX12	299.1	15.21
TD-EX13	295.9	15.51

The strain rate for all the TD specimens is shown in Table 17.

Table 17: Strain rate for TD specimens

	Strain Rate (s^{-1})
TD-EX1	989
TD-EX2	995
TD-EX3	1014
TD-EX4-Necked	1035
TD-EX5	1003
TD-EX6	997
TD-EX7	1002
TD-EX8	988
TD-EX9	1001
TD-EX10-Necked	992
TD-EX11	992
TD-EX12-Necked	1006
TD-EX13	1013

The failed specimens were not included in the average and standard deviation calculations. The average strain rate for the TD specimens was $999 s^{-1}$ with a standard deviation of $9 s^{-1}$.

It is thought that this first series of tension tests performed with the newly developed SHPB apparatus were quite successful, in terms of the repeatability of the test, and the consistency of the striker velocity, the strain rates achieved and the fracture location near the centre of the gauge length. Apart from one specimen that showed evidence of slippage during the test, the collar clamps proved to be an adequate method of clamping the specimens to the incident and transmission bars. However it remains to be shown that the experimental results generated with this SHPB apparatus are indeed accurate.

5.2 Comparison of experimental data to known data

In order to validate the experimental results generated by the tensile SHPB apparatus described in this thesis, the DP600 stress-strain data presented in the previous section was compared to data obtained from the University of Waterloo for the same DP600 steel. A research team at the University of Waterloo carried out these tests within the framework of a collaborative research project with the University of Windsor and a number of industrial partners. This comparison is meaningful in as much as the experimental results from the tests described in the previous section and those that were supplied by the researchers at the University of Waterloo were all obtained from specimens taken from the very same coil of DP600 steel. Tensile tests were carried out with both SHPB testing facilities at a strain rate of 1000 s^{-1} in the RD, DD, and TD (Rahmaan et al., 2014). Figure 68 - Figure 70 show the comparisons of the flow curves obtained from both laboratories in the RD, DD and TD, respectively.

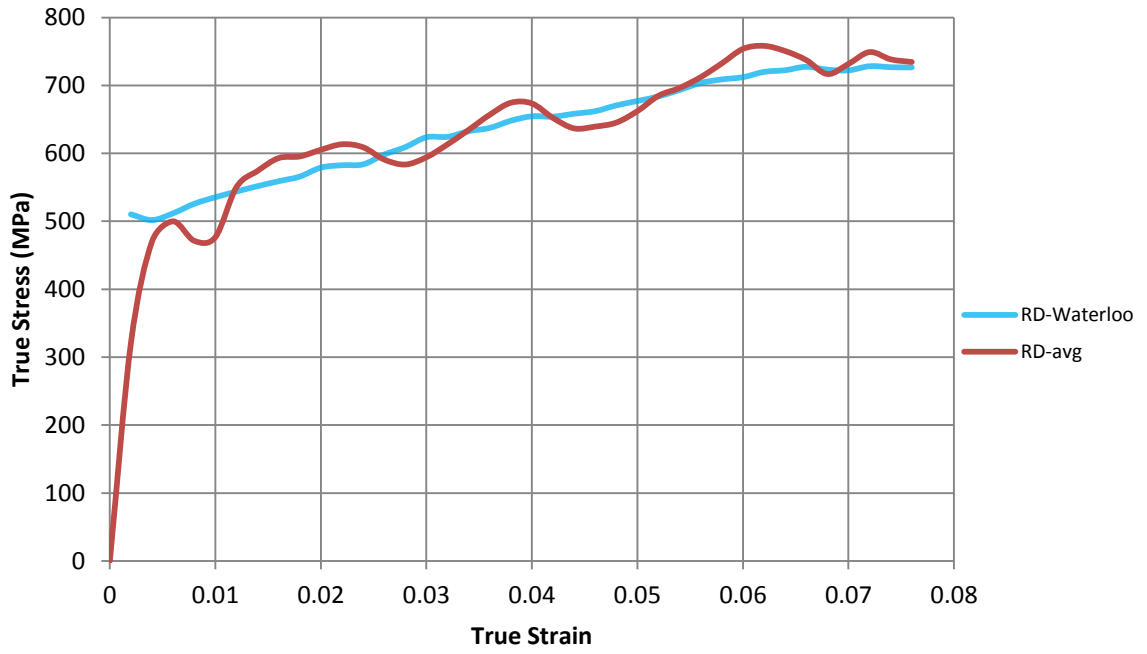


Figure 68: Comparison of the true stress vs. true strain data in the RD obtained from two different laboratories

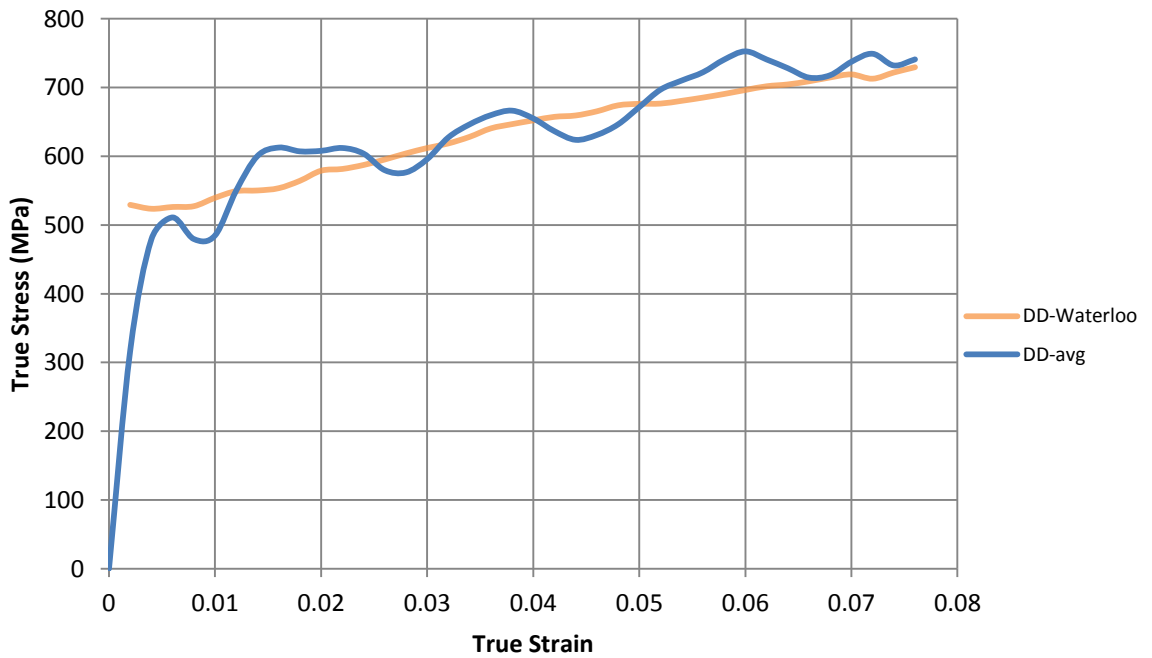


Figure 69: Comparison of the true stress vs. true strain data in the DD obtained from two different laboratories

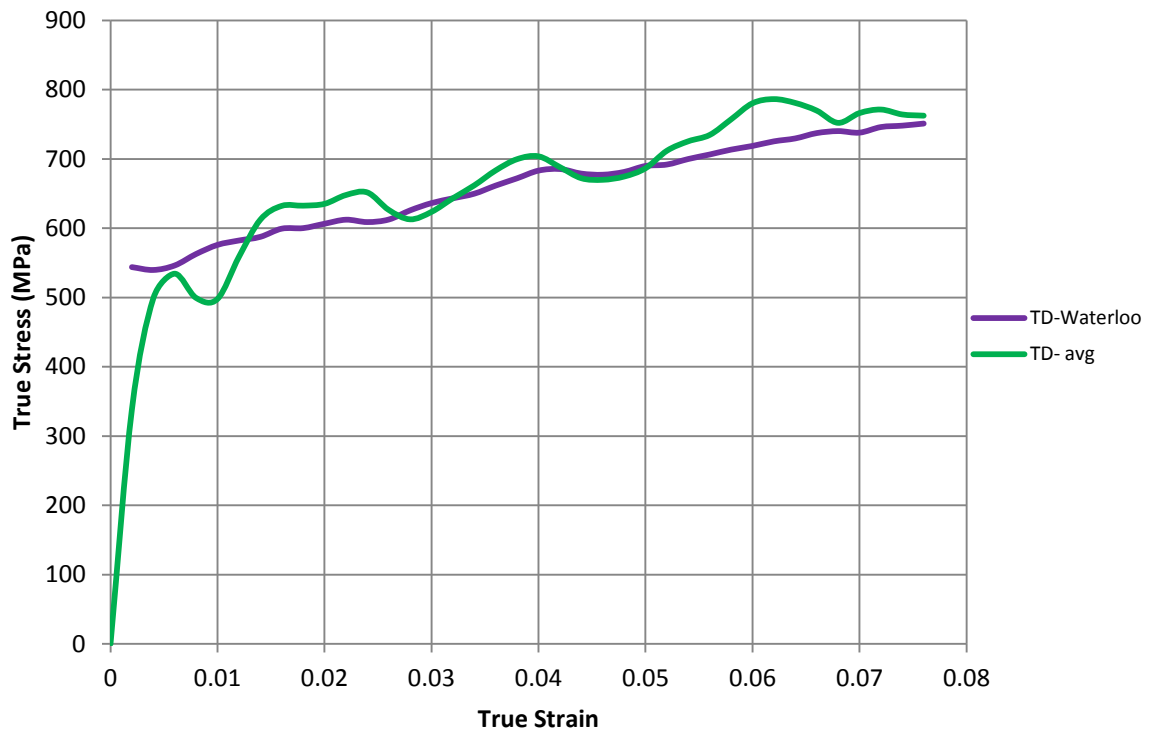


Figure 70: Comparison of the true stress vs. true strain data in the TD obtained from two different laboratories

The same validation metric and average error that were used to calibrate the strain gauges were also used to compare the flow curves obtained from this testing apparatus with those from the University of Waterloo. Since the Waterloo research team has been publishing data obtained from their SHPB testing apparatus in peer-reviewed papers for many years, it is reasonable to assume that these data are reliable and can be considered as a reference from which to evaluate the data obtained from our newly developed apparatus. The average error and validation metric for each material direction are summarized in Table 18.

Table 18: Error and Validation metric for comparing project data to known data

Direction	Error %	Validation Metric
DD	4.05	0.9596
RD	3.20	0.9681
TD	3.87	0.9614

The flow curves obtained from tests using the newly developed SHPB apparatus were also compared with data obtained from ArcelorMittal. However, in this case, the data supplied by ArcelorMittal was obtained from SHPB specimens taken from a DP600 steel sheet with a nominal thickness of 1.8mm and pulled them in tension along the RD at a strain rate of 1000 s^{-1} . It is not known which laboratory or SHPB apparatus was used to produce these data from ArcelorMittal. Nevertheless, the flow curve supplied by ArcelorMittal was plotted in Figure 71 along with the corresponding flow curve obtained from our SHPB apparatus.

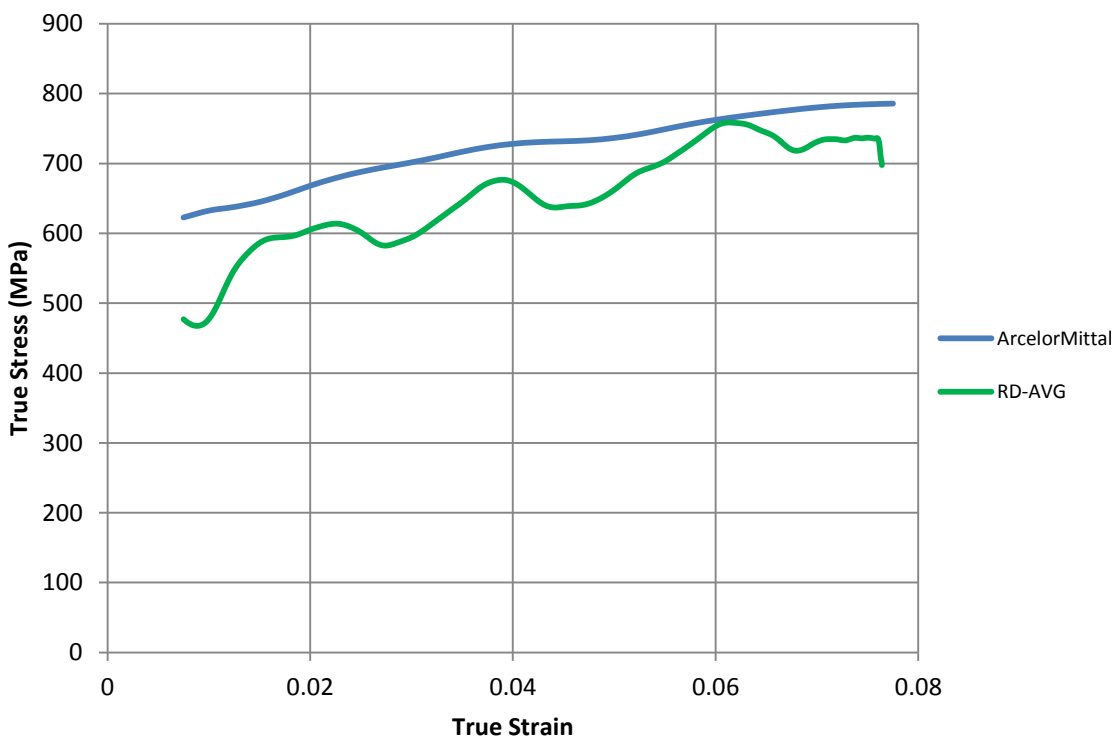


Figure 71: Comparison of ArcelorMittal and project data

The same validation metric and average error that was used with the strain gauge calibration was used to compare the data from ArcelorMittal and the adjusted data from this project. The average error and validation metric are compiled in Table 19.

Table 19: Error and Validation metric for comparing ArcelorMittal data to project data

Direction	Error %	Validation Metric
RD	9.49	0.9056

This large error could have been due to the materials being from different batches of DP600 steel with different mechanical properties.

The data sets obtained from the University of Waterloo and ArcelorMittal have very few data points in the data sets. ArcelorMittal has 40 data points making up their data set and the University of Waterloo has 71 data points in their data set. This is much less than the 1302 data points are used in the data sets, generated by our new apparatus. When looking at the data sets from ArcelorMittal and the University of Waterloo the strain intervals are evenly spaced and at exact points. This leads to the hypothesis that both ArcelorMittal and the University of Waterloo are reducing their data sets by interpolating the stress data at even strain spacing.

Chapter 6: Conclusions and Recommendations

6.1 Conclusions

The various mechanical components of a tension SHPB testing apparatus have been designed, built, assembled and shown to function well. The addition of a high-speed data acquisition system, the corresponding instrumentation and LabVIEW operating software has enabled the author to successfully carry out a series of SHPB tests on DP600 steel specimens. A MATLAB code was also developed to post-process the strain signals, and using the Hopkinson equations, to obtain the high strain rate flow curves of this grade of steel.

The following observations can be made based upon the experience of developing and using the tensile SHPB apparatus:

1. The gas gun has a slow pressure leak; however the largest pressure deviation during testing was only ± 3.5 kPa. In spite of this small deviation of the pressure over time the gas gun can be effectively operated at a specified pressure.
2. The gas gun had an average deviation in the velocity of the striker of 0.333 m/s during the calibration of the gas gun. This deviation is related to the friction in the barrel of the gas gun, since the inside of the gas gun is not polished to a smooth finish.
3. The average strain rate for the RD, DD, and TD directions were within error for the test strain rate of 1000 s^{-1} .
4. The data provided from the tensile SHPB apparatus is within 4.06% of the reference data obtained from the University of Waterloo.

In addition to the observations made, the following conclusions can be drawn after the completion of this tension SHPB apparatus:

1. The gas gun, striker, incident and transmission bars were adequately aligned so that friction between the bars and the bar holders was minimized.
2. The LabVIEW code is able to control the triggering of the data acquisition system
3. The MATLAB code developed is able to calculate the stress and strain in the test specimen
4. This tensile SHPB apparatus is functioning well and providing accurate results.

5. The length of the incident bar could have been increased in order to obtain flow curves that reach greater levels of deformation.

6.2 Recommendations for further improvement of the SHPB

A number of recommendations can be made to help improve the operation and performance of the tensile SHPB apparatus and the data provided by the tensile SHPB apparatus.

1. Disassemble the gas gun and remove the sharp edges that are cutting the O-rings, to stop the slow pressure leak in the gas gun.
2. When making new bars to replace the initial bars, consider using a longer incident bar to allow the stress wave to fully develop into a one-dimensional wave. It would also be useful to get some extra bar material to perform quasi-static tensile tests in order to obtain the bar's yield and ultimate tensile stress.
3. Incident and transmission bars made of C350 maraging steel rather than the AISI 4140 steel would allow the tensile SHPB apparatus to achieve greater strain rates, by enlarging the elastic region of the incident and transmission bars and allowing higher strength specimens to be tested.
4. Using a longer striker would allow the incident pulse to take place over a longer period of time, and thus the stress wave would take longer to disperse into a one-dimensional wave. And in order to fit a longer striker into the tensile SHPB apparatus the momentum transmitter bar would have to be shortened. The shortened momentum transmitter bar would let the incident bar holder to be moved away from the gas gun to allow the longer striker to use more of the gas gun barrel for acceleration up to the required velocity. It would also require higher gas pressures to achieve the striker velocity, and the calibration of the gas gun would need to be redone.
5. It would be very interesting to carry out SHPB tests with a high-speed, high-resolution digital camera. This would allow for an independent measure of strain and strain rate in the gauge of the specimen.
6. Additional development of the LabVIEW virtual instrument would help to make the software more user-friendly and versatile. For instance, adding a timing pulse that would trigger the operation of the high speed camera. Also, the current process of

having to start and stop the vi to switch between reading the pressure in the gas gun and data collecting, can be eliminated by using an event structure to read the selection buttons change of state.

7. The post-processing MATLAB code could be improved by adding dispersion correction to the code. This would help eliminate the oscillations in the incident pulse and provide a more accurate true stress versus strain graph.

References

- ASM Handbook . (2000). *ASM Handbook, Volume 8, Mechanical Testing and Evaluation*. Materials Park: ASM International.
- ASM International. (2006). *Atlas of Fatigue Curves*. Materials Park: ASM International.
- ASME. (2003). *Unified Inch Screw Threads, (UN and UNR Thread Form) B1.1-2003*. American Society of Mechanical Engineers.
- ASME. (2010). *2010 ASME Boiler & Pressure Vessel Code*. New York: American Society of Mechanical Engineers.
- ASTM . (2012). A29/A29M-12. *Standard Specification for General Requirements for Steel Bars, Carbon and Alloy, Hot-Wrought*. ASTM International.
- ASTM . (2014). A370-14. *Standard Test Methods and Definitions for Mechanical Testing of Steel Products*. ASTM International.
- ASTM. (2015). E8/E8M-15a. *Standard Test Methods for Tension Testing of Metallic Materials*. ASTM International.
- ATI Allvac. (2011). *ATI VascoMax C-200/C-250/C-300/C-350 Alloys (Version 2)*. Technical Data Sheet, Monroe.
- Audysho, R., Smith, R., Altenhof, W., & Patel, K. (2013). Aluminum foam core density and geometry influences on the deformation mechanisms of foam filled braided tubular structures in tension. *Materials and Design*, 54, 394–413.
- AZO Materials. (2015). *AISI 4140 Alloy Steel* . Retrieved 06 20, 2015, from AZOM.com: <http://www.azom.com/article.aspx?ArticleID=6769>
- Berggren, R. E., & Reynolds, R. M. (1970). The Light-Gas-Gun Model Launcher. In *AGARD BALLISTIC RANGE TECHNOLOGY* (pp. 9-96). Nasa.
- Boyer, H. E. (2006). *Atlas of Fatigue Curves*. Materials Park: ASM International.
- Budynas, R. G., & Nisbett, K. J. (2011). *Mechanical Engineering Design* (9th ed.). New York: McGraw Hill.
- Cardarelli, F. (2008). *Materials Handbook: A Concise Desktop Reference* (2nd ed.). London: Springer.
- Carson Sr., B. E., Chuse, R., & Ellenberger, J. P. (2004). *Pressure Vessels The ASME Code Simplified* (8th ed.). New York: McGraw Hill.

- Chen, W., & Song, B. (2011). *Split Hopkinson (Kolsky) Bar Design, Testing and Applications*. New York: Springer.
- Chowdhury, S. (2002). *Design For Six SIGMA*. Kaplan Publishing.
- Chree, C. (1889). The equations of an isotropic solid in polar and cylindrical coordinates, their solutions and applications. *Cambridge Philosophical Society*, 250-369.
- Clark, J. M. (1993). *High Strain Rate Tensile Testing*. Master's Thesis: Carleton University.
- Davies, R. (1956). Stress waves in solids. *British Journal of Applied Physics*, 7, 203-209.
- Davies, R. M. (1948). Critical Study of the Hopkinson Pressure Bar. *Philosophical Transactions of the Royal Society of London. Series A, Mathematical and Physical Sciences*, 240(821), 375-457.
- Follansbee, P. S., & Frantz, C. (1983). Wave Propagation in the Split Hopkinson Pressure Bar. *Journal of Engineering Materials and Technology*, 105(1), 61-66.
- Gallina, F., Birch, R., & Alves, M. (2003). Design of a Split Hopkinson Pressure Bar. *The 18th Brazilian Congress of Mechanical Engineering*. Brazil.
- Gebremeskel, S. A., Asija, N., Priyanshu, A., Chouhan, H., & Bhatnagar, N. (2014). Design Customization and Development of Split Hopkinson Pressure Bar for Light and Soft Armour Materials. *Global Journal of Researches in Engineering: A Mechanical and Mechanics Engineering*, 14(7), 62-75.
- Gorham, D. A., Pope, P. H., & Field, J. E. (1992, July). An Improved Method for Compressive Stress-Strain Measurements at Very High Strain Rates. *The Royal Society*, 438(1902).
- Hasenpouth, D. (2010). *Tensile High Strain Rate Behavior of AZ31B Magnesium Alloy Sheet*. Master's Thesis: University of Waterloo.
- Hauser, F. E. (1966, August). Techniques for Measuring Stress-Strain Relations at High Strain Rates. *Experimental Mechanics*, 6(8), 395-402.
- Hopkinson, B. (1914). A Method of Measuring the Pressure Produced in the Detonation of High Explosives or by the Impact of Bullets. *Proceedings of the Royal Society of London Series A, Containing Papers of a Mathematical and Physical Character*, 89(612), 411-413.
- Johnson, W. (1972). *Impact Strength of Materials*. Edward Arnold.
- Kaiser, M. A. (1998). Advancements in the Split Hopkinson Bar Test. Master's Thesis: *Virginia Polytechnic Institute and State University*, 1-94.
- Kolsky, H. (1949). An Investigation of the Mechanical Properties of Materials at Very High Rates of Loading. *Proceedings of the Physical Society. Section B*, 62(11), 676-700.

- Kolsky, H. (1964). Stress waves in solids. *Journal of sound and vibration*, 1(1), 88-110.
- Kraft, J. M., Sullivan, A. M., & Tipper, C. F. (1954). The Effect of Static and Dynamic Loading and Temperature on the Yield Stress of Iron and Mild Steel in Compression. *Proceedings of the Royal Society of London. Series A, Mathematical and Physical Sciences*, 221(1144), 114-127.
- Kyowa. (2015). *Technical Notes Strain Gauges*. Retrieved 06 28, 2015, from kyowa-ei.com: http://www.kyowa-ei.com/eng/download/technical/strain_gages/pdf_wiring_001_en.pdf
- Landon, J. W., & Quinney, H. (1923). Experiments with the Hopkinson Pressure Bar . *Proceedings of The Royal Society A, Mathematical, Physical and Engineering Sciences*, 103, 622-643.
- Lindholm, U. S., & Yeakley, L. M. (1968, January). High Strain-rate Testing: Tension and Compression. *Experimental Mechanics*, 8(1), 1-9.
- Maris, C. (2014). *Experimental determination of the forming limits of DP600 and AA5182 sheets in electrohydraulic free forming*. Master's Thesis: University of Windsor.
- MatWeb. (2015). *AISI 4140 Steel, annealed at 815°C (1500°F) furnace cooled 11°C (20°F)/hour to 665°C (1230°F), air cooled, 25 mm (1 in.) round* . Retrieved 06 20, 2015, from MatWeb : <http://www.matweb.com/search/DataSheet.aspx?MatGUID=7b75475aa1bc41618788f63c6500d36b&ckck=1>
- MTS . (2015). *MTS Criterion Series 40 Electromechanical Universal Test Systems*. Retrieved from MTS systems: https://www.mts.com/ucm/groups/public/documents/library/mts_006225.pdf
- National Instruments. (2006, 09 06). *Choosing the Right Strain-Gauge for Your Application*. Retrieved 07 02, 2015, from National Instruments white papers: <http://www.ni.com/white-paper/3092/en/>
- National Instruments. (2015). *National Instruments*. Retrieved 2015, from National Instruments: <http://canada.ni.com/>
- National Instruments. (2015, 06). *NI SCB-68A*. Retrieved 06 27, 2015, from National Instruments: <http://sine.ni.com/nips/cds/view/modelpopup/p/pcat/16779/lang/en>
- Nicholas, T. (1981, May). Tensile Testing of Materials at High Rates of Strain. *Experimental Materials*, 21(5), 177-185.
- Oberg, E., Jones, F. D., Horton, H. L., & Ryffel, H. H. (2008). *Machinery's Handbook* (28 ed.). New York: Industrial Pres.

- Oberkampf, W. L., & Trucano, T. G. (2002). Verification and validation in computational fluid dynamics. *Progress in Aerospace Sciences*, 38(3), 209-272.
- Ohio State University. (n.d.). *High Strain Rate Tension Tests*. Retrieved 2015, from Ohio State University, Dynamic Mechanics of Materials Laboratory:
<http://www.mecheng.osu.edu/lab/dmm/node/35>
- PBC Linear. (2010). *Simplicity Technical Guide - Linear Plane Bearing*. Roscoe.
- Permatex. (2015). *Technical Data Sheet Permatex® Aviation Form-A-Gasket® No. 3 Sealant Liquid*. Retrieved 06 2015, from Permatex:
<http://www.permatex.com/component/documents/?view=tds&format=raw&filename=80018.pdf&market=automotive>
- Pochhammer, L. (1876). Über die fortplanzungsgeschwindigkeiten schwingungen in einem unbegrenzten isotropen kreiscylinder. *J. fTur die reine angewandte Mathematik*, 81, 324-336.
- Rahmaan, T., Bardelcik, A., Imbert, J., Butcher, C., & Worswick, M. J. (2014). Effect of strain rate on flow stress and anisotropy of DP600, TRIP780 and AA5182-O sheet metal alloys. *The International Journal of Impact Engineering*.
- Salisbury, C. P., Worswick, M. J., & Mayer, R. (2006). High rate constitutive modeling of aluminium alloy tube. *Journal des Physiques IV France*, 134, 43-38.
- Sharpe, J. W. (2008). *Springer Handbook of Experimental Solid Mechanics*. Springer.
- Smerd, R., Winkler, S., Salisbury, C., Worswick, M., Lloyd, D., & Finn, M. (2005). High strain rate tensile testing of automotive aluminum. *International Journal of Impact Engineering*, 32(1-4), 541-560.
- Staab, G. H., & Gilat, A. (1991). A Direct-tension Split Hopkinson Bar for High Strain-rate Testing. *Experimental Mechanics*, 31, 232-235.
- Tampere University of Technology. (2015). *Hopkinson Split Bar (HSB)*. Retrieved 06 2015, from Tampere University of Technology Department of Materials Science:
<http://www.tut.fi/en/about-tut/departments/materials-science/research/research-equipment/mechanical-testing/hsb/index.htm>
- Texas Instruments. (2005, 02). *INA129 Precision, Low Power insrtumentation amplifier*. Retrieved from Texas Instruments: <http://www.ti.com/product/ina129>
- Ulacia, I., Salisbury, C., Hurtado, I., & Worswick, M. (2011). Tensile characterization and constitutive modeling of AZ31B magnesium alloy sheet over wide range of strain rates and temperatures. *Journal of Materials Processing Technology*, 211(5), 830-839.

- University of Mississippi. (2015). *Blast and Impact Dynamics Lab*. Retrieved 06 2015, from Mechanical Engineering Univeristy of Mississippi:
<http://www.engineering.olemiss.edu/mechanical/facilities/blast.html>
- WorldAutoSteel. (2014). *Advanced High-Strength Steels Application Guidelines Version 5.0*. WorldAutoSteel.
- WorldAutoSteel. (2015). *Vehicle Safety and Steel*. Retrieved 07 13, 2015, from WorldAutoSteel:
See more at: <http://www.worldautosteel.org/why-steel/safety/vehicle-safety-and-steel/#sthash.IR6kCqwv.dpuf>
- Worswick, M. (2015). *High Strain Rate Infrastructure*. Retrieved from University of Waterloo Forming and Impact Mechanics Research:
<http://www.me.uwaterloo.ca/~worswick/Facilities/highRate.html>
- Zanettin, L., Young, K., & Hussain, A. (2012). *Split bar apparatus for high rate material mechanical behaviour assessment*. Capstone Report: University of Windsor.

Appendix A – Durability Calculation of Threads on the Bars

Due to the nature of the loading on a tensile SHPB apparatus, calculating the durability of the threads on the incident bar is important. The durability calculation was done by calculating the ratio of the impact force to the shear area of the threads. This calculation gives the stress amplitude acting on the threads shear area, which can then be used with an S-N curve to gather the approximate number of cycles to failure. The assumption is made that there are no energy losses when the striker hits the anvil. Using this assumption the impact force on the anvil is equal to the incident stress from the striker. The impact force can be calculated from:

$$F_i = \sigma_i A_{st} \quad (A.1)$$

The highest stress that would be seen by the incident bar would be the yield stress of the bar material. The bar material used to test this tensile SHPB apparatus was a 4140 steel, with a Rockwell hardness of 28 HRC. Since the bar material yield tensile stress was not provided by the supplier, and because there was not sufficient bar material to produce test coupons, the material yield point was estimated from a comparison of measured hardness values and yield tensile stresses, seen in Figure 72. The HRC and yield values for the Tensile strength vs. HRC graph seen in Figure 72, were obtained from the website MatWeb.com.

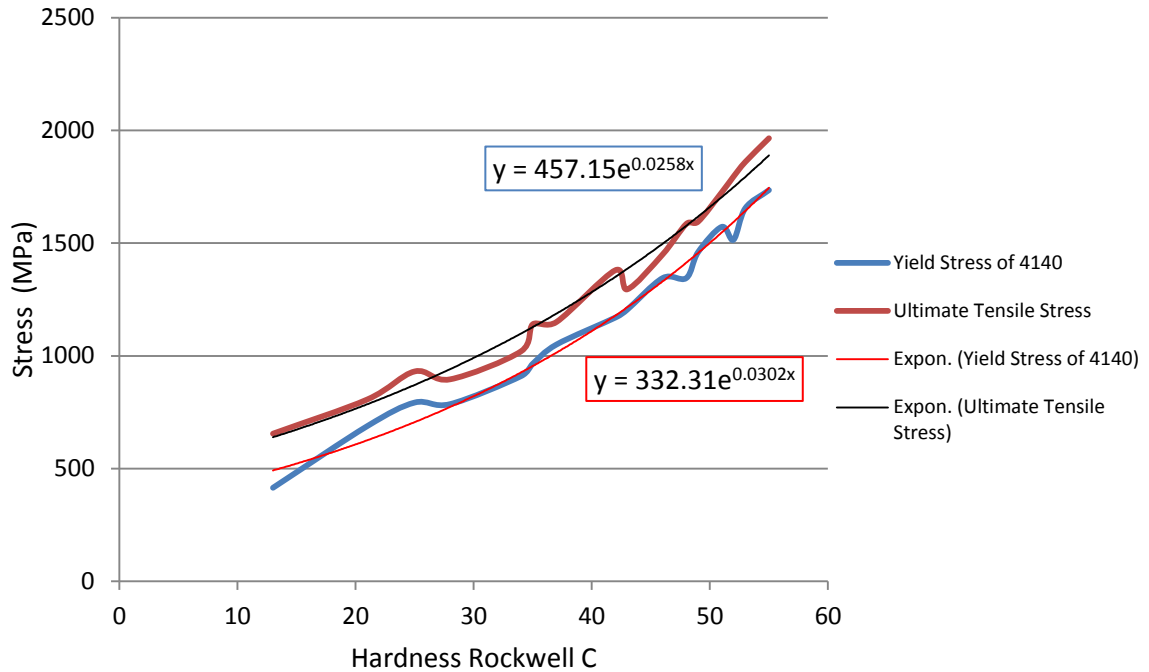


Figure 72: Yield Strength versus Hardness Rockwell C

From the trend line equation, the yield tensile stress of the 4140 steel was calculated to be 776 MPa. To use equation A.1 the area of the striker was calculated from:

$$A_{st} = \frac{\pi}{4} (d_o^2 - d_i^2) \quad (A.2)$$

$$A_{st} = \frac{\pi}{4} (0.023^2 - 0.019^2)$$

$$A_{st} = 0.00029 \text{ m}^2$$

Knowing the area of the striker and the yield stress, equation A.1 can be used to get the incident force:

$$F_i = \left(776 \frac{\text{MN}}{\text{m}^2} \right) (0.00029 \text{ m}^2)$$

$$F_i = 222832.9 \text{ N}$$

$$F_i = 223 \text{ kN}$$

To calculate the shear area of the threads, the geometry of the threads is needed. The threads used on the incident bar and the anvil are 3/4"-16 UNF, which allows the shear area of the

thread to be calculated. By using the minor diameter of the thread, the circumference of the minor diameter circle can be calculated using:

$$C_t = \pi D_{min} \quad (A.3)$$

$$C_t = \pi * 0.017178 \text{ m}$$

$$C_t = 0.054 \text{ m}$$

The length of each thread used to calculate the shear area is smallest at the minor diameter of the thread seen in Figure 73. The distance through the thread at the minor diameter is the area where the thread will shear.

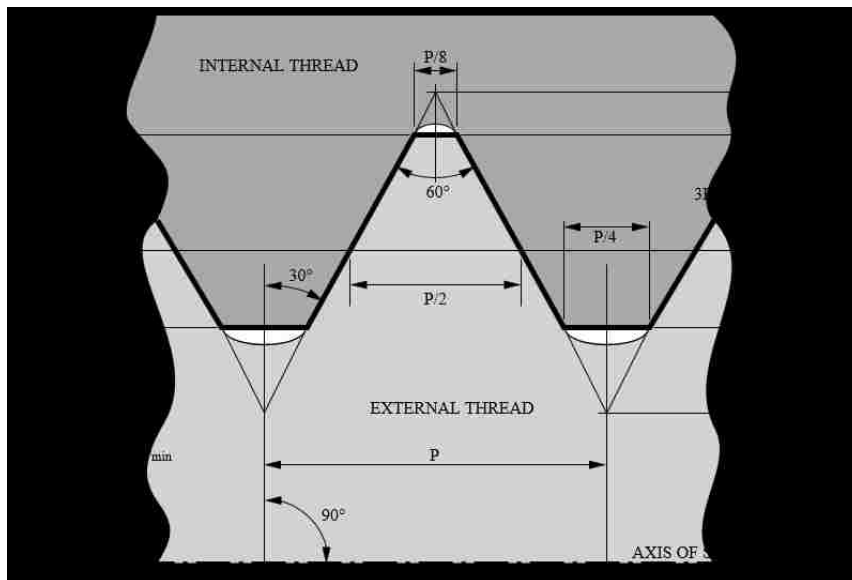


Figure 73: Unified Thread Standard profile dimensions

Simple trigonometry (see Figure 74), was used to calculate the distance, X, which is half the distance through the thread.

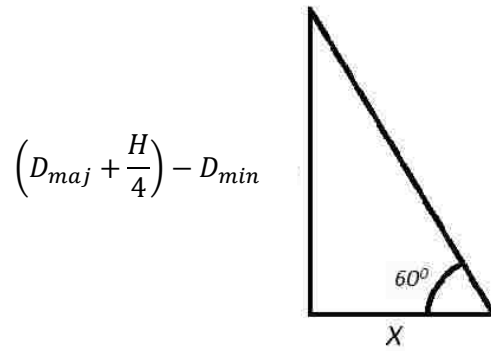


Figure 74: Triangle Used to calculate X, the half-distance through the thread

$$X = \frac{\left(\frac{(D_{maj} + \frac{H}{4}) - D_{min}}{2} \right)}{\tan 60^\circ} \quad (A.4)$$

$$X = \frac{\left(\frac{(0.01905m + 0.0003437) - 0.01717802m}{2} \right)}{\tan 60^\circ}$$

$$X = 0.000639613 \text{ m}$$

$$2X = 0.001279226 \text{ m}$$

The shear area is:

$$A_{thread} = \text{\#of threads} * 2X * C \quad (A.5)$$

$$\begin{aligned} A_{thread} &= (14)(0.001279226 \text{ m})(C \\ &= 0.054 \text{ m}) \end{aligned}$$

$$A_{thread} = 0.000967m^2$$

Using the incident force and the shear area, the shear stress amplitude can be calculated:

$$\tau_{thread} = \frac{F_i}{A_{thread}} \quad (A.6)$$

$$\tau_{thread} = \frac{223 \text{ kN}}{0.000967 \text{ m}^2}$$

$$\tau_{thread} = 230 \text{ MPa}$$

Using von Mises, the shear stress can be converted to normal stress:

$$\sigma = \frac{1}{\sqrt{2}} \sqrt{(\sigma_x - \sigma_y)^2 + (\sigma_y - \sigma_z)^2 + (\sigma_z - \sigma_x)^2 + 6(\tau_{xy}^2 + \tau_{yz}^2 + \tau_{zx}^2)} \quad (A.7)$$

$$\sigma = \sqrt{3} \tau_{thread}$$

$$\sigma = \sqrt{3} * 230 \text{ MPa}$$

$$\sigma = 398 \text{ MPa}$$

Knowing the normal stress amplitude, an S-N curve, seen in Figure 75, for ANSI 4140 steel is used to get the number of cycles to failure.

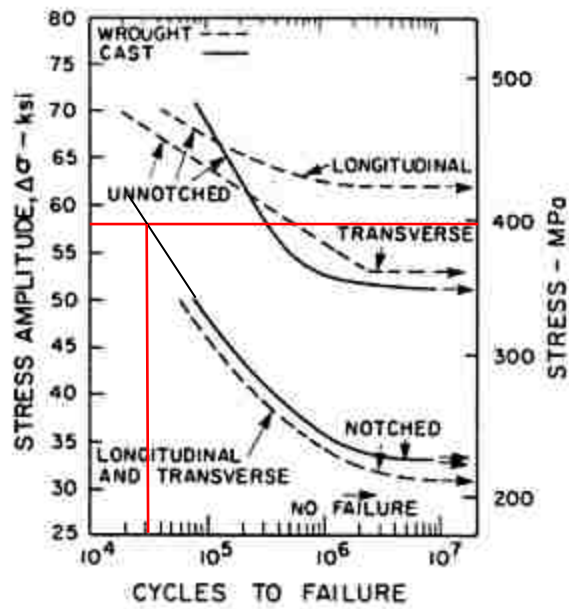
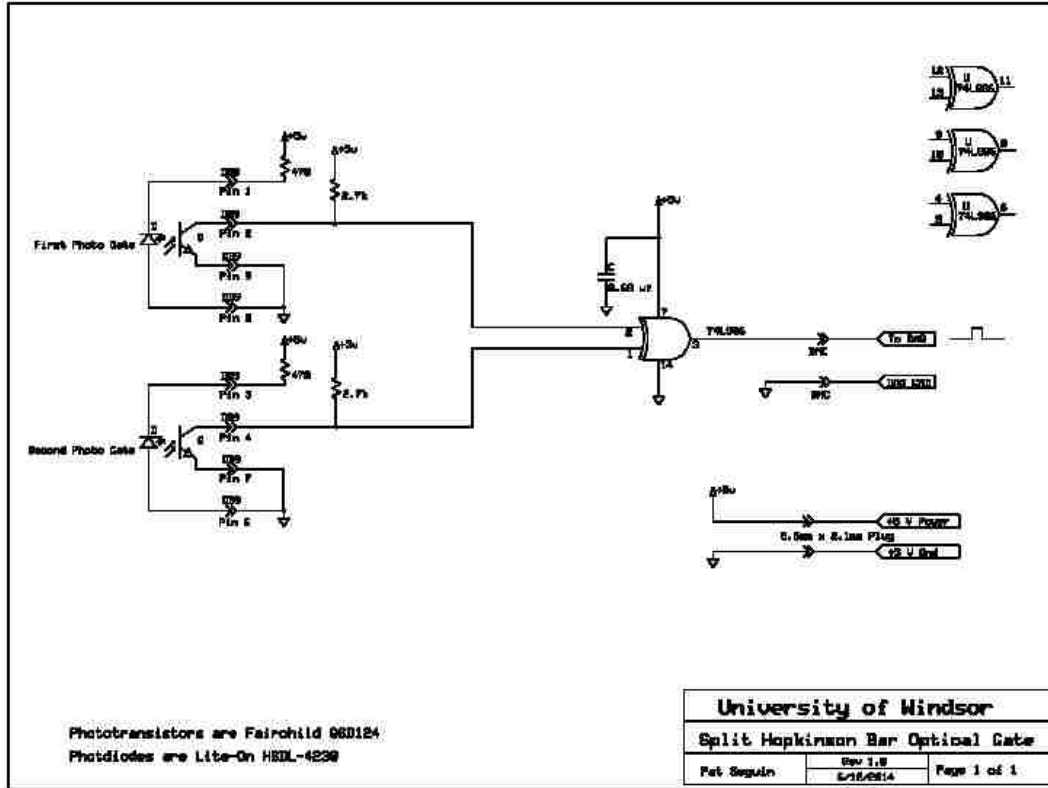


Figure 75: S-N Curve for 4140 steel (Boyer, 2006)

From the S-N curve in Figure 75, the estimated failure limit for the threads is about 30,000 cycles. This estimation was based on the maximum stress the bars can withstand without yielding. Since the bars will not be subject to this load every time the bars are used, the number of cycles that the bars can withstand before failure will be greater than this estimate.

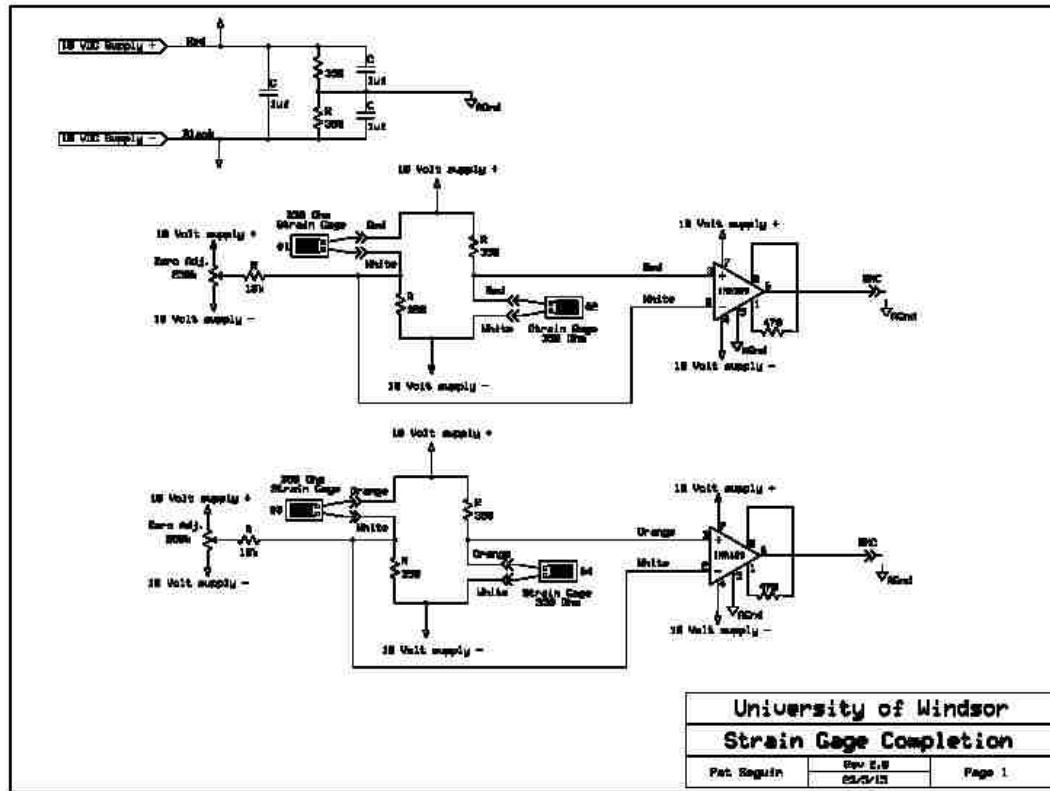
Appendix B - Technical Drawings

Striker velocity optical gate



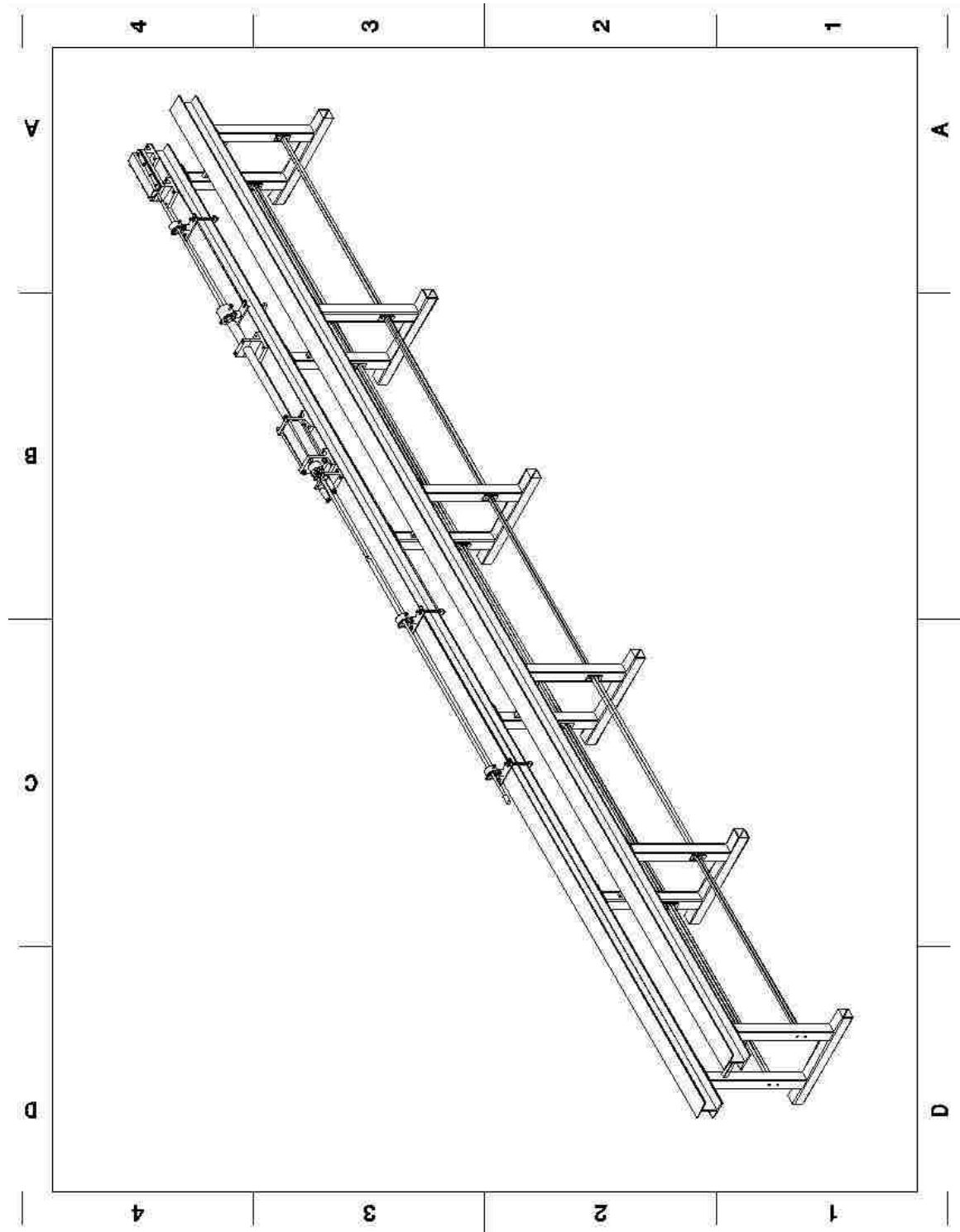
C:\Schematics\Split Hopkinson Bar.sch - Sheet1

Strain Gauge Completion and Amplification



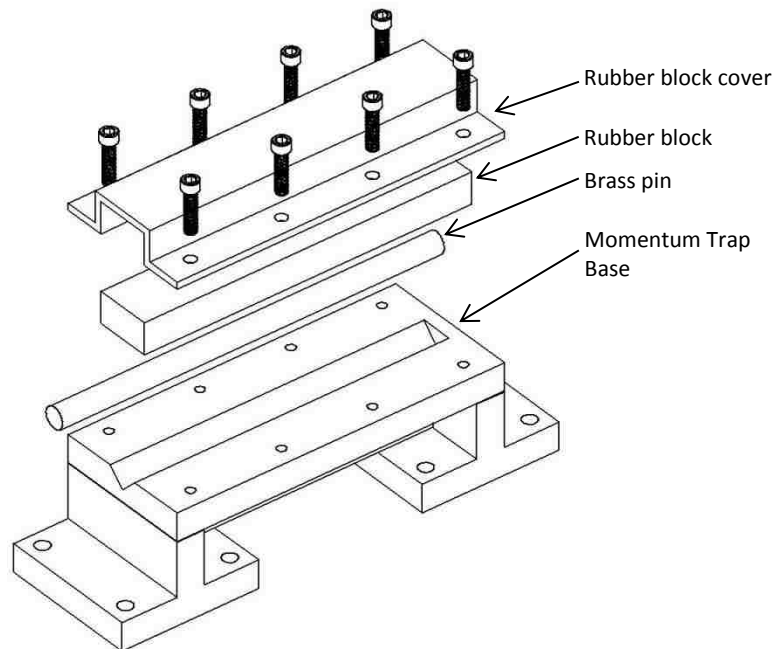
C:\Schematics\Split Hopkinson Bar gate _strain_amp.sch - Sheet2

Overall assembly of tensile SHPB apparatus

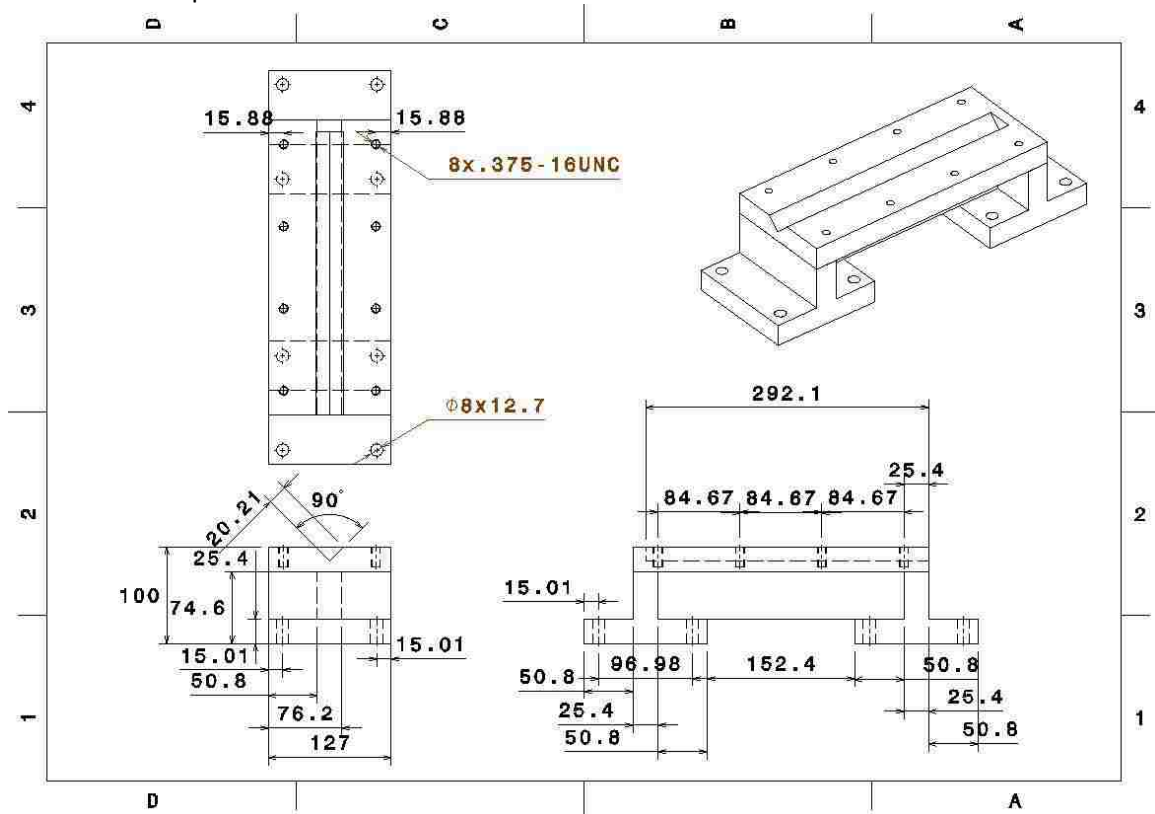


The assembly of the momentum trap consists of:

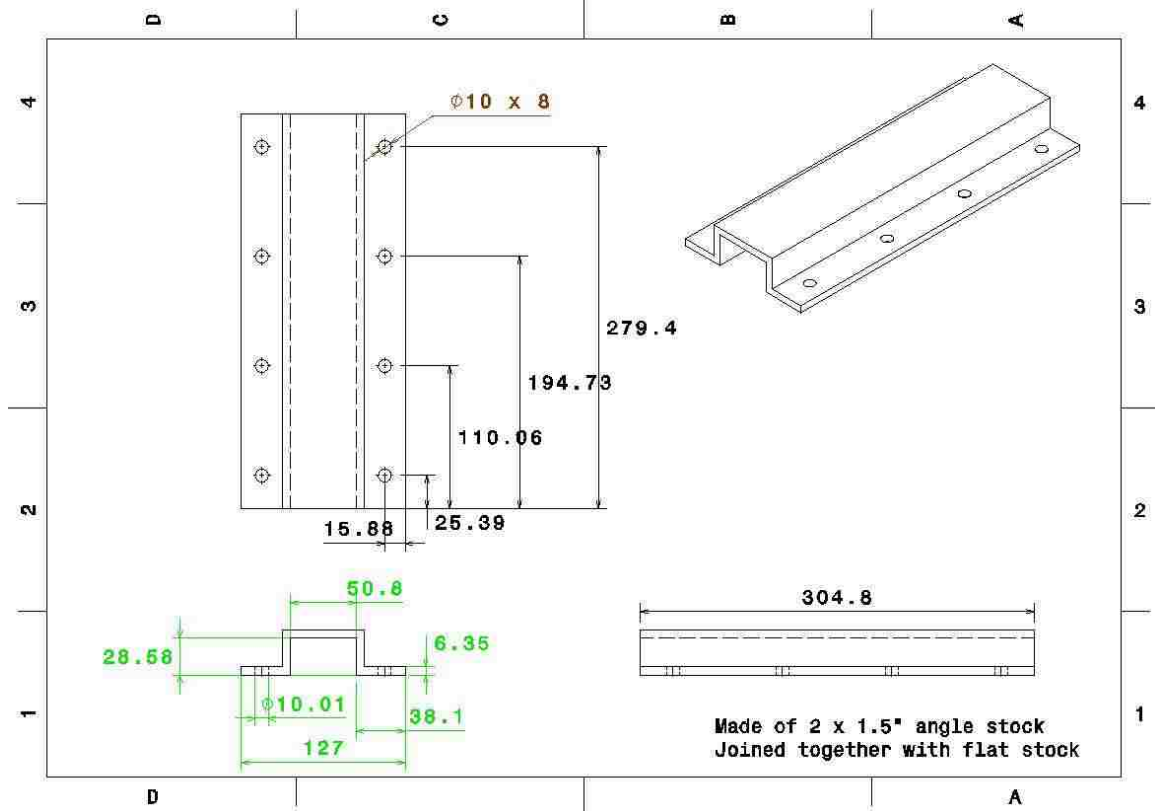
- Momentum trap base
- Rubber block cover
- Rubber block
- Brass pin
- Momentum transfer bar and anvil



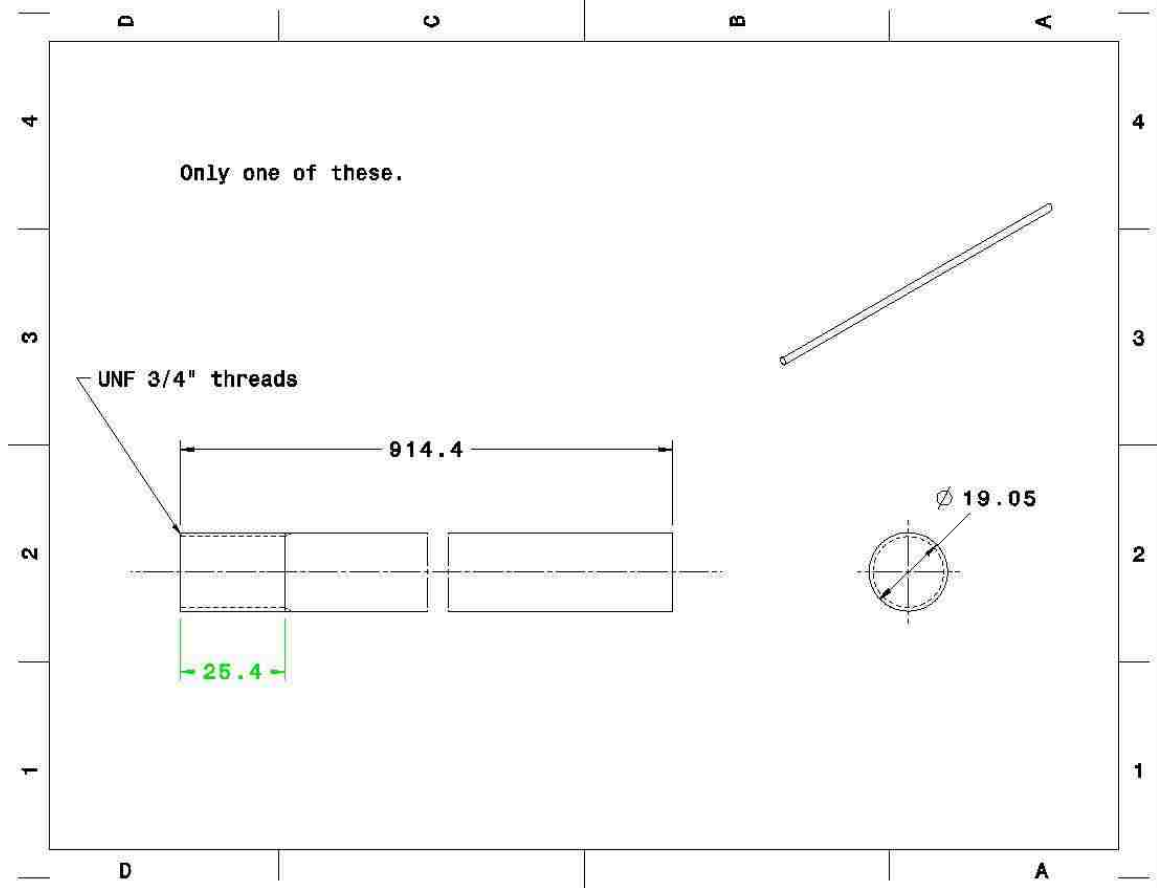
Momentum trap base



Momentum trap cover

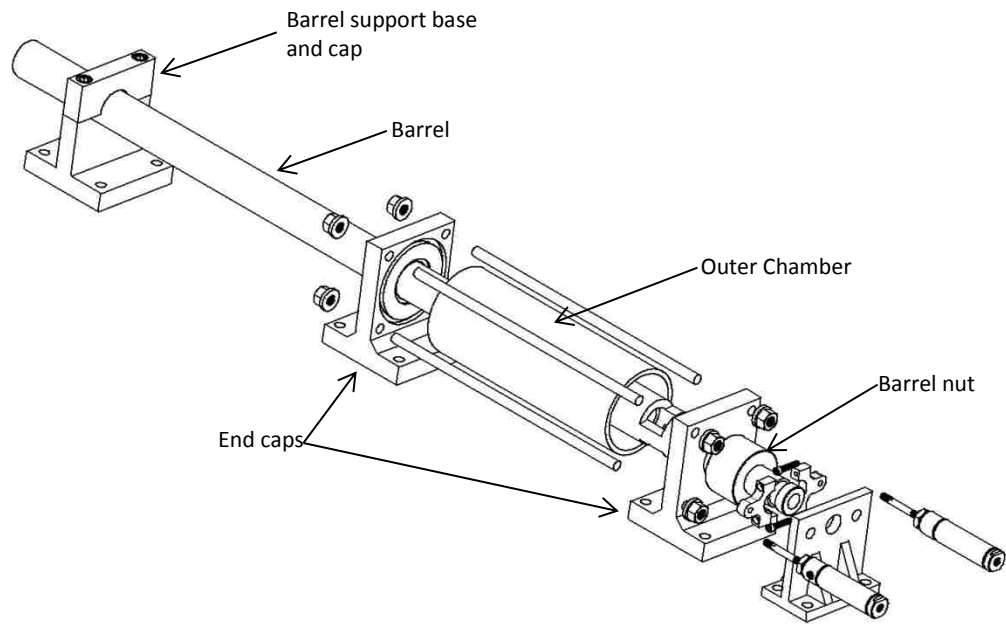


Momentum transfer bar

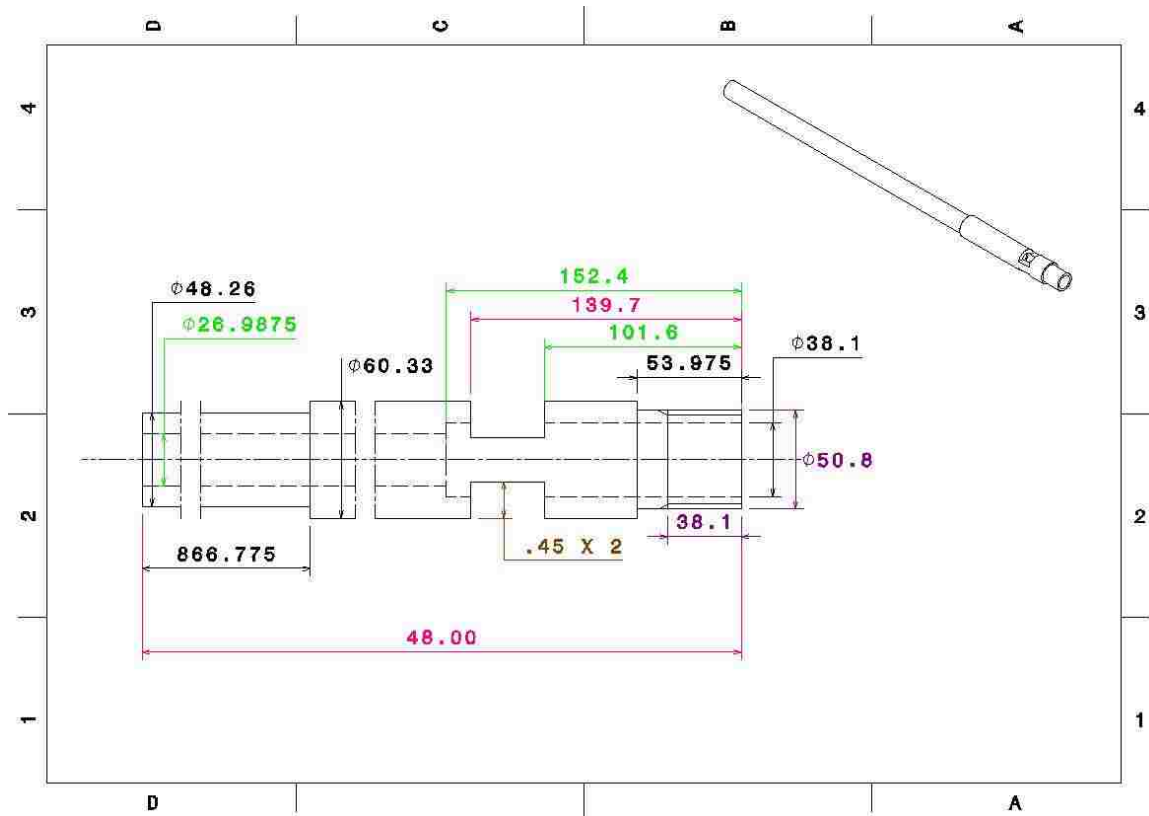


The assembly of the gas gun consists of:

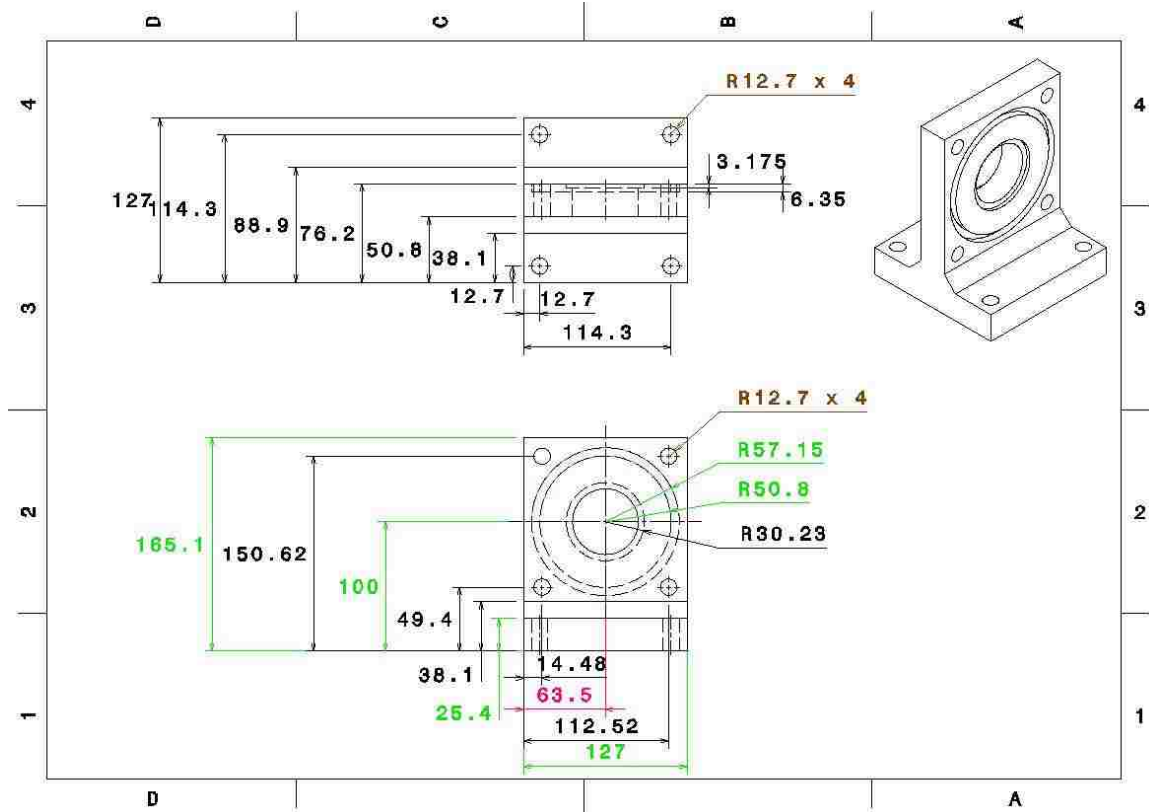
- Barrel
- End caps
- Outer chamber
- Barrel nut
- Barrel support base and cap



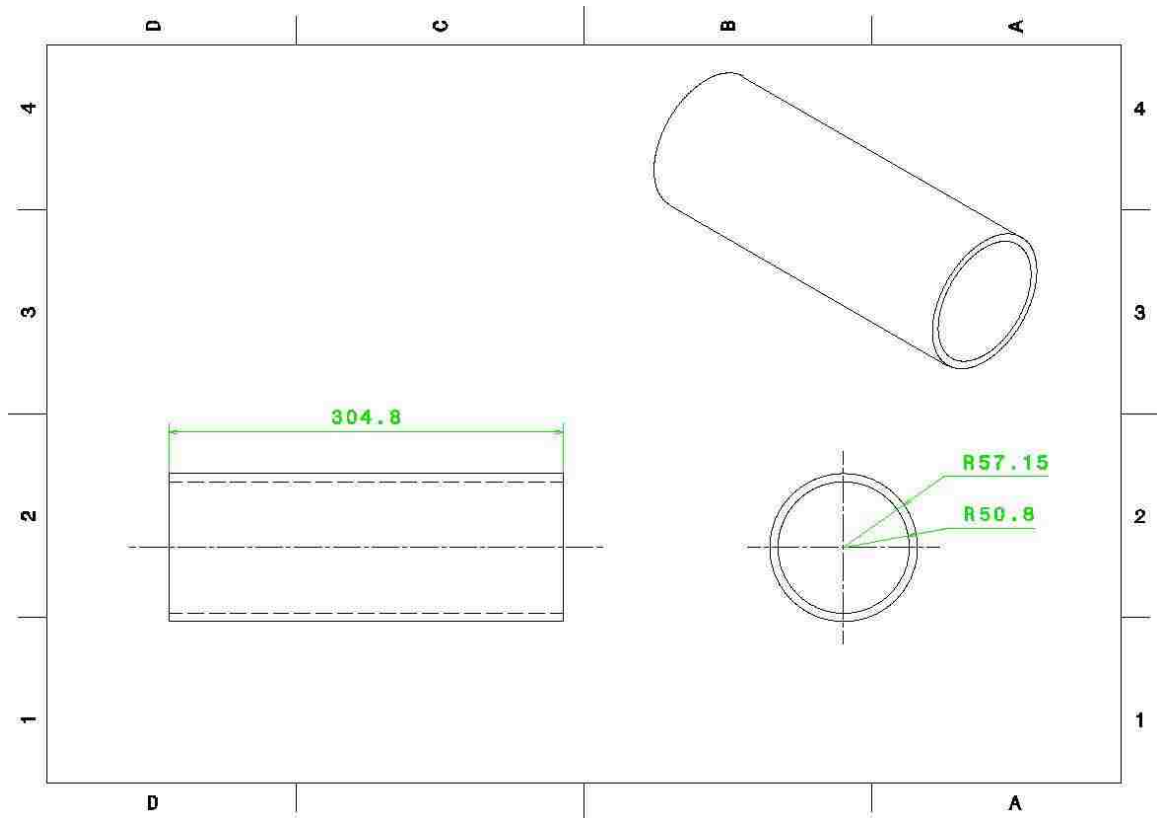
Barrel



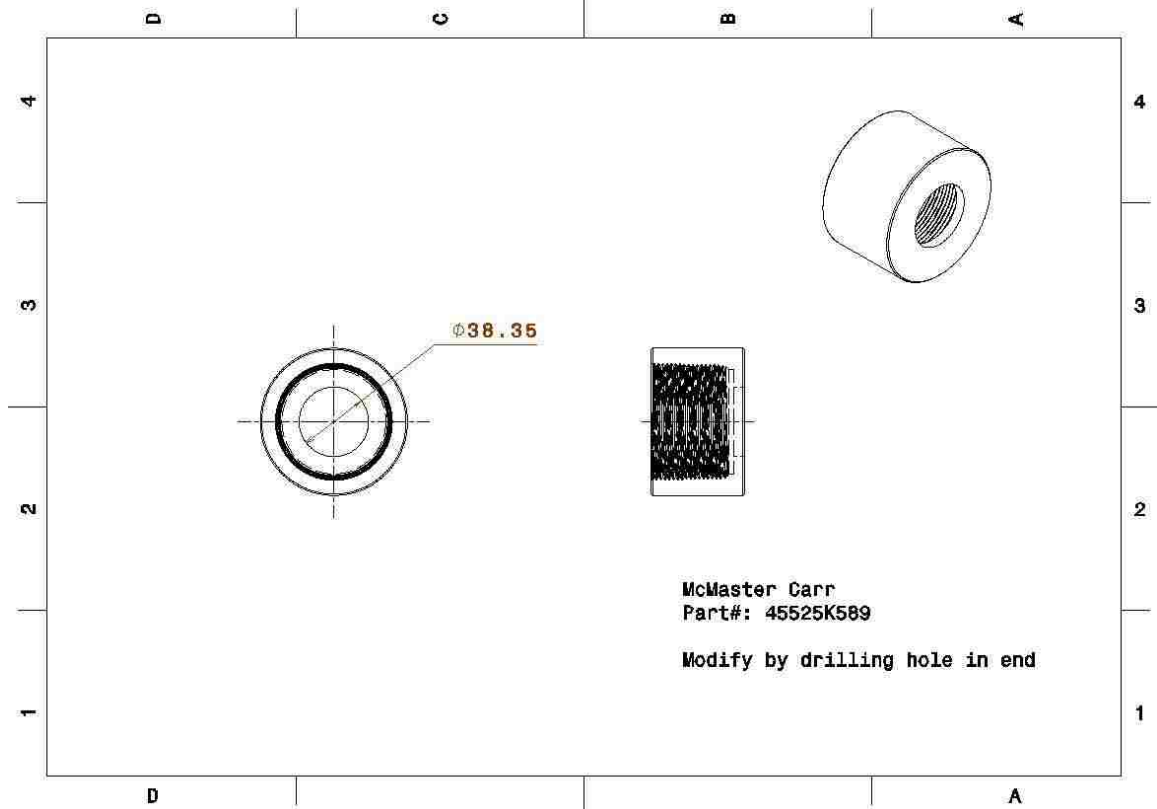
End Cap



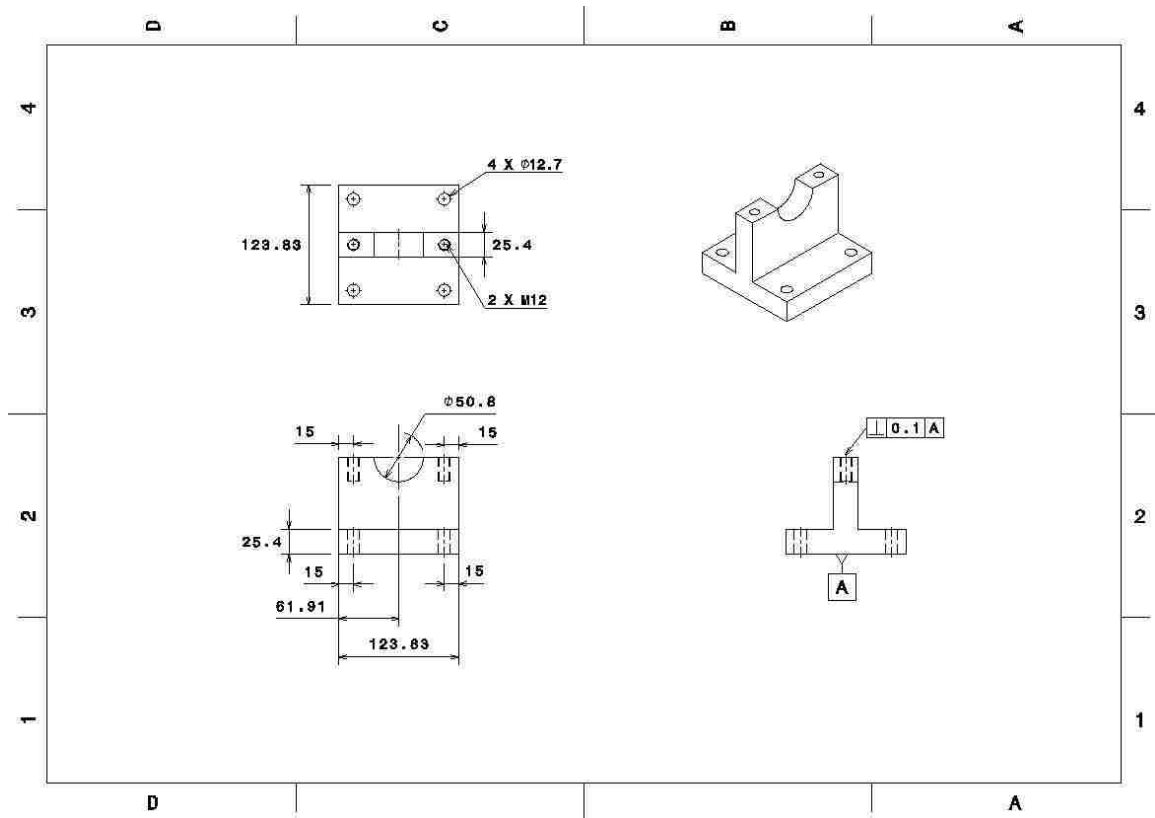
Outer Chamber



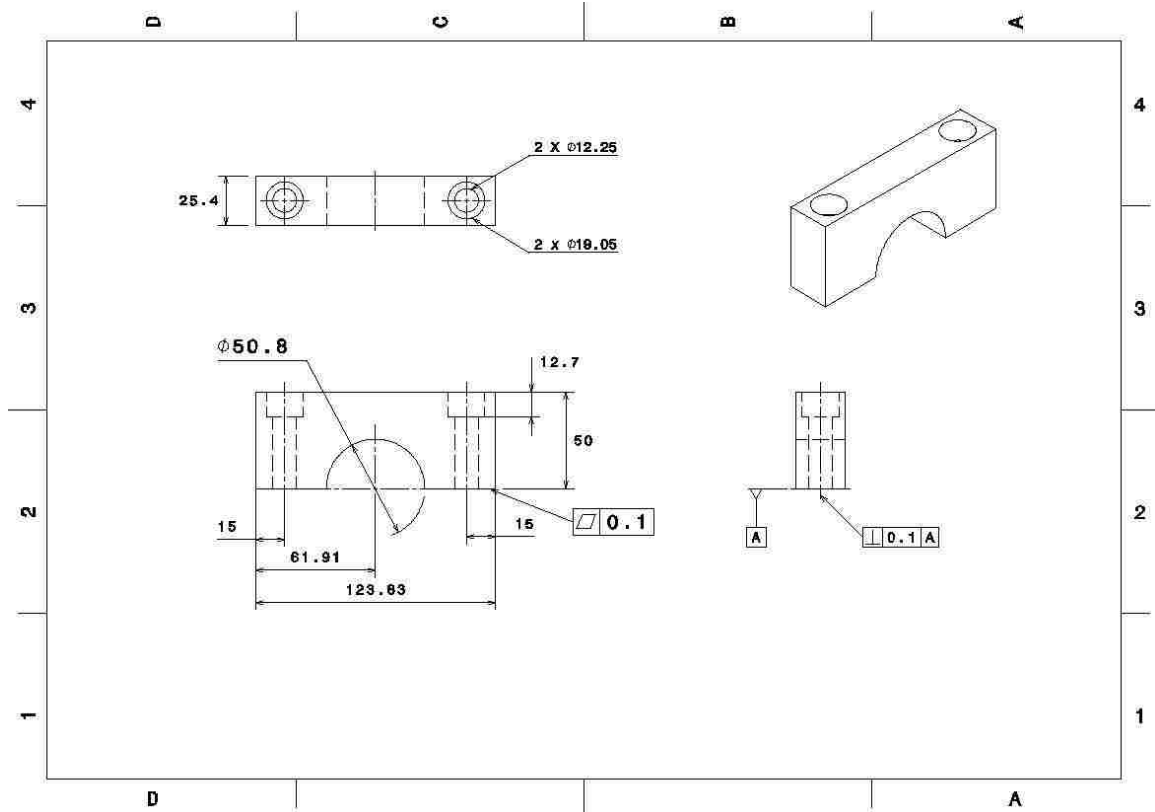
Barrel Nut



Barrel Support Base

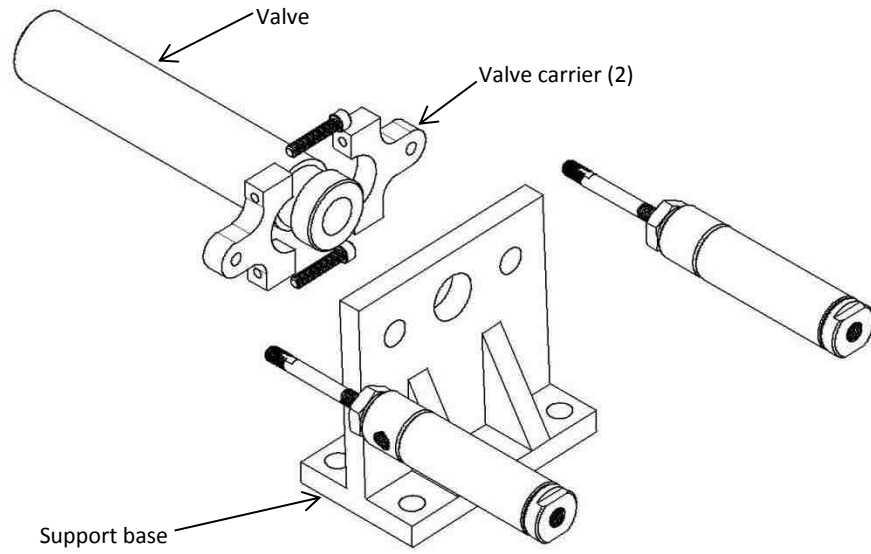


Barrel Support Cap

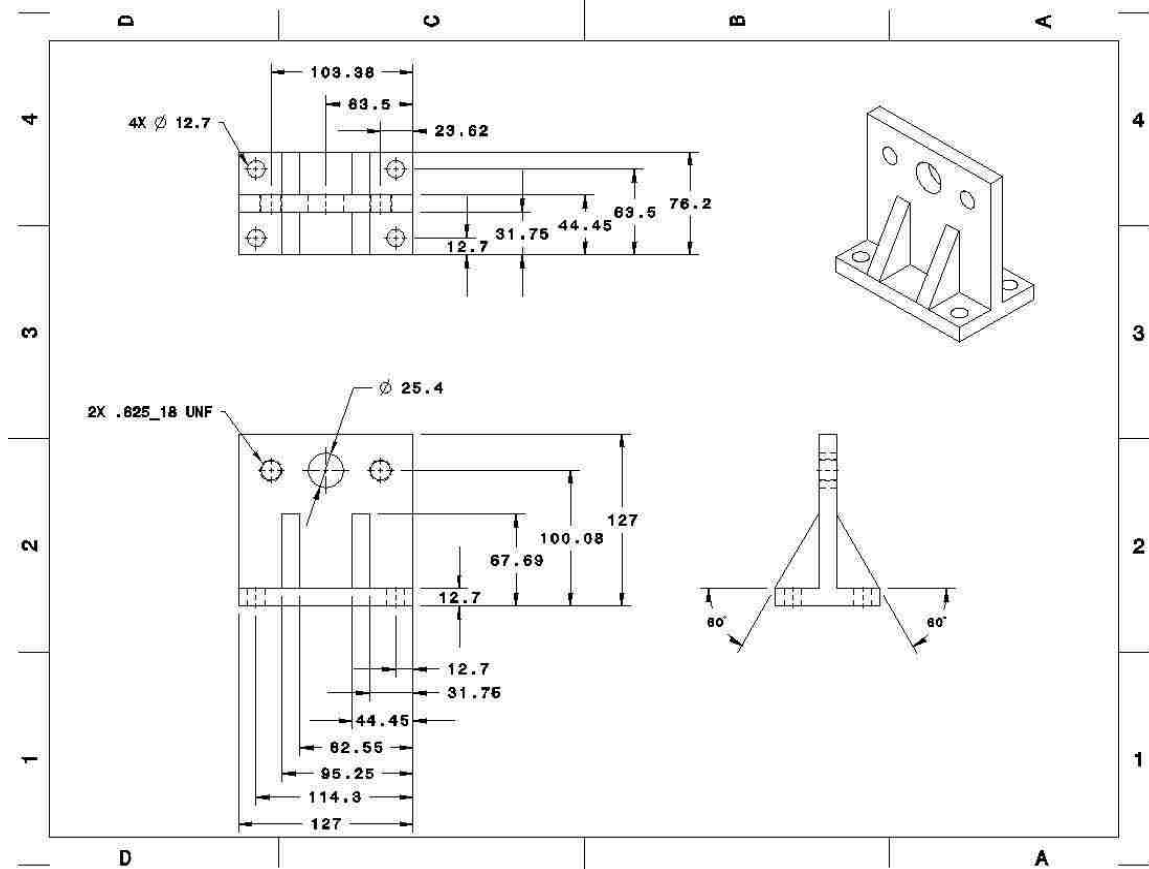


The assembly of the gas gun valve assembly consists of:

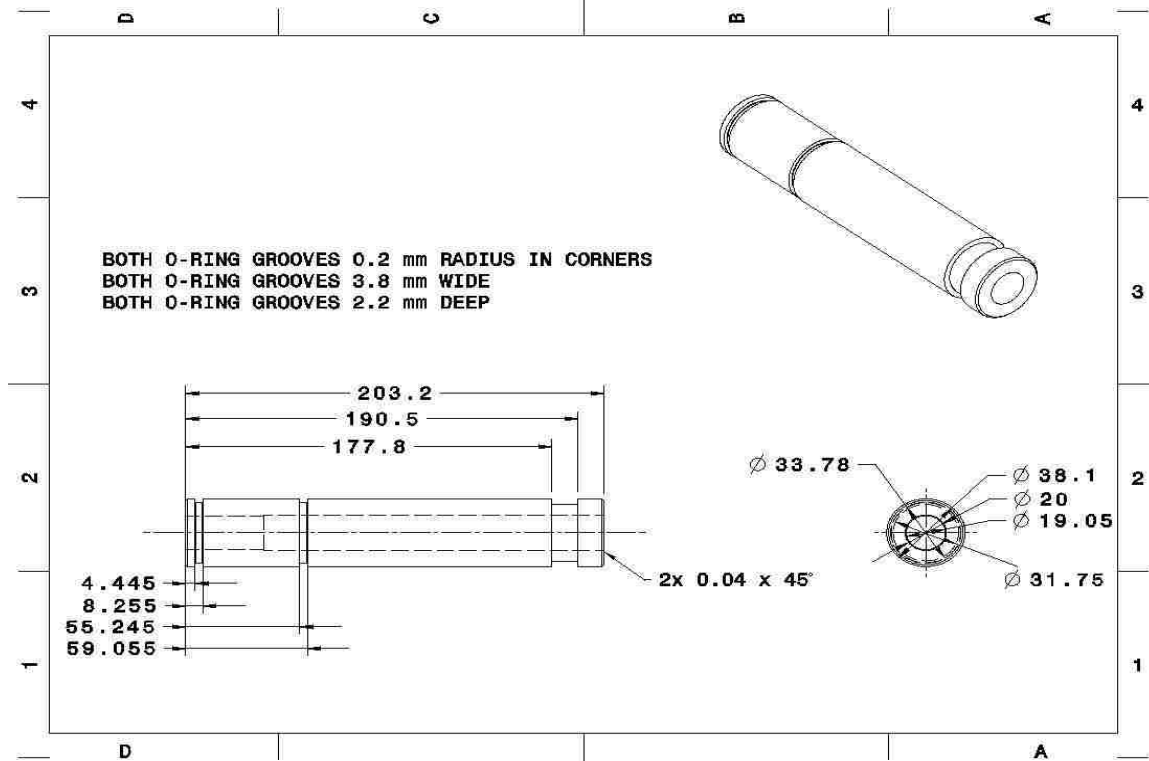
- Support base
- Valve
- Valve carriers



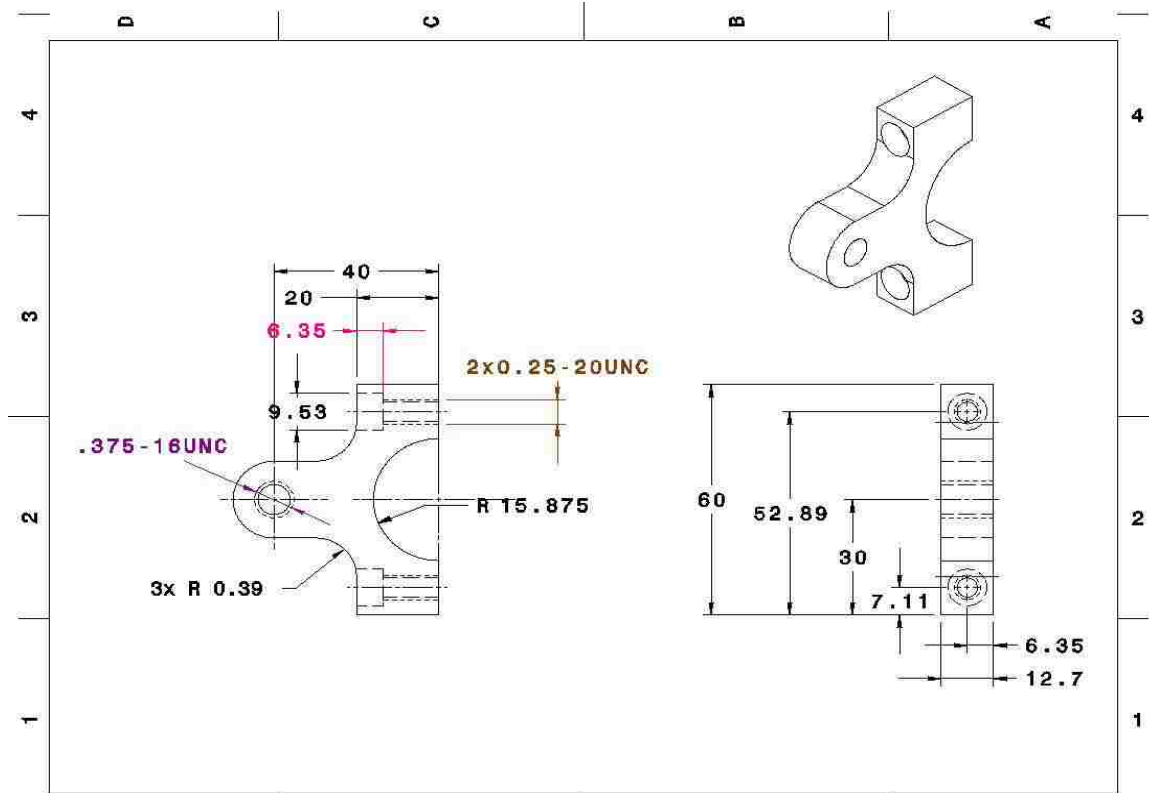
Support Base



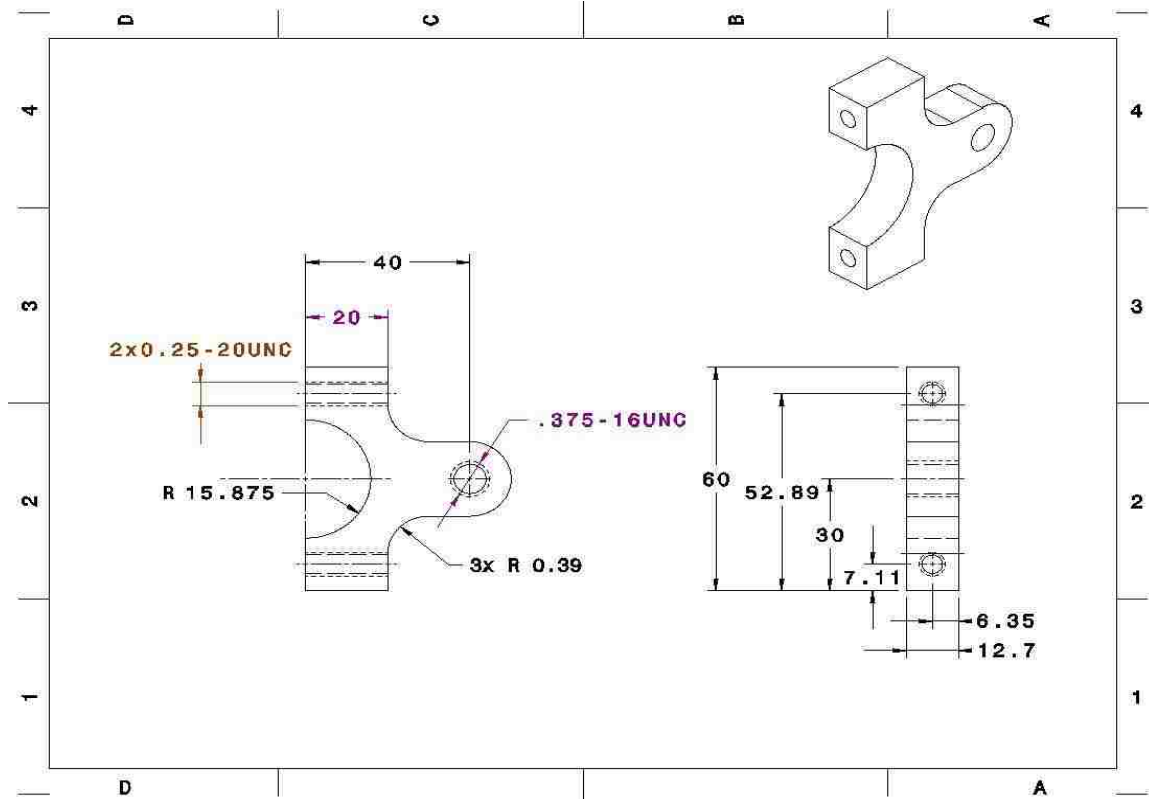
Valve



Valve Carrier



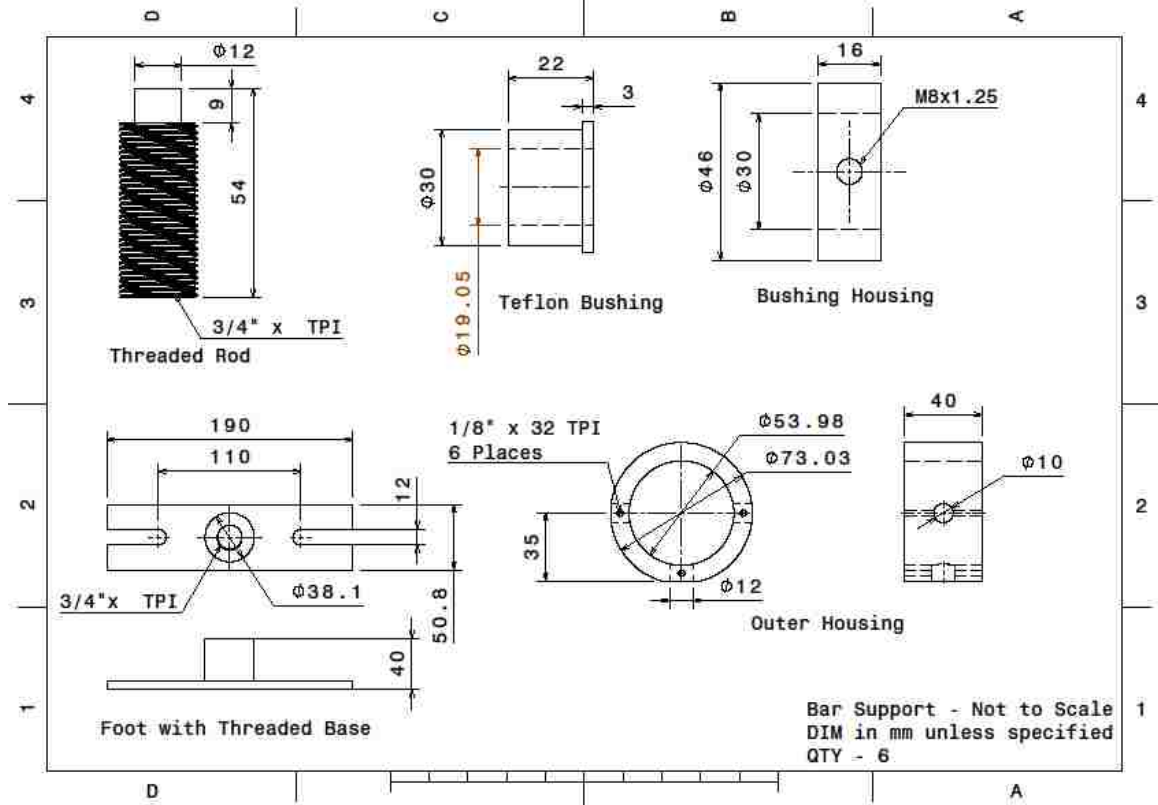
Valve Carrier



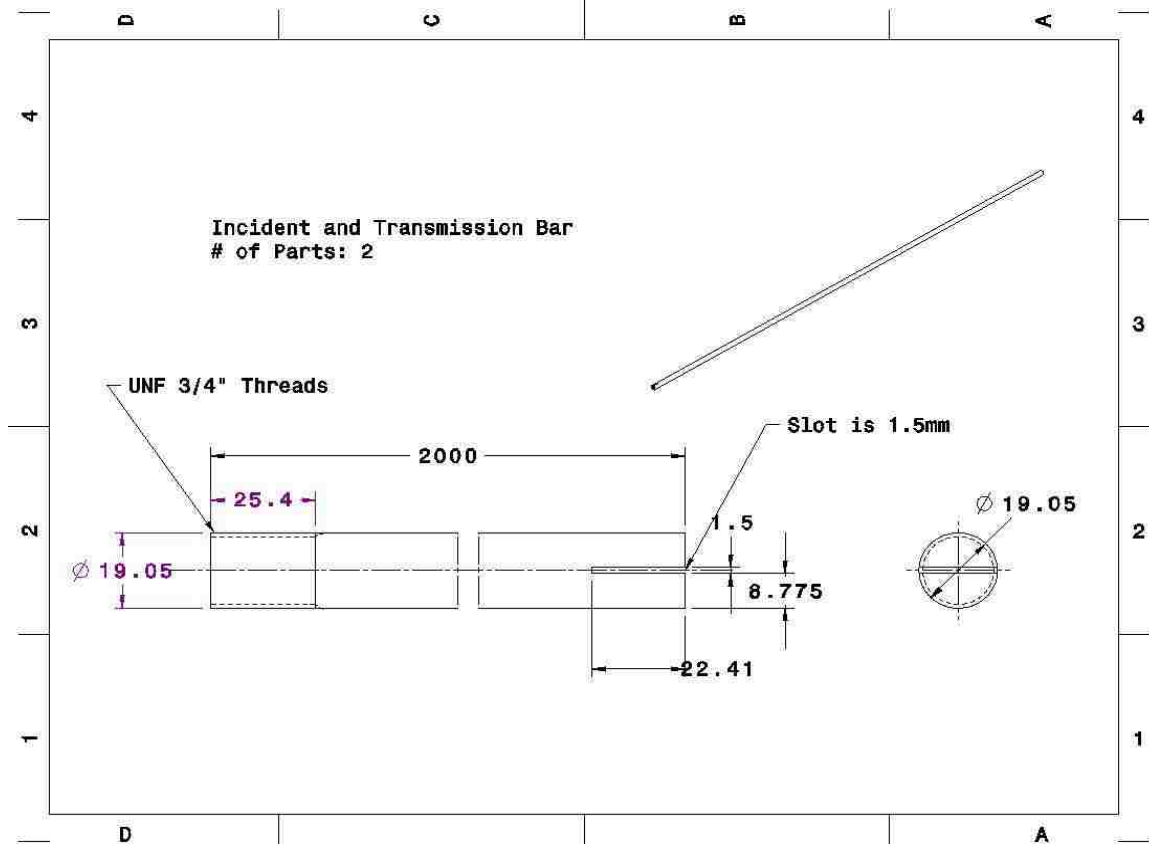
The assembly of the incident and transmission bars consists of:

- Incident and transmission bars
- Anvils
- Striker
- Bar holder

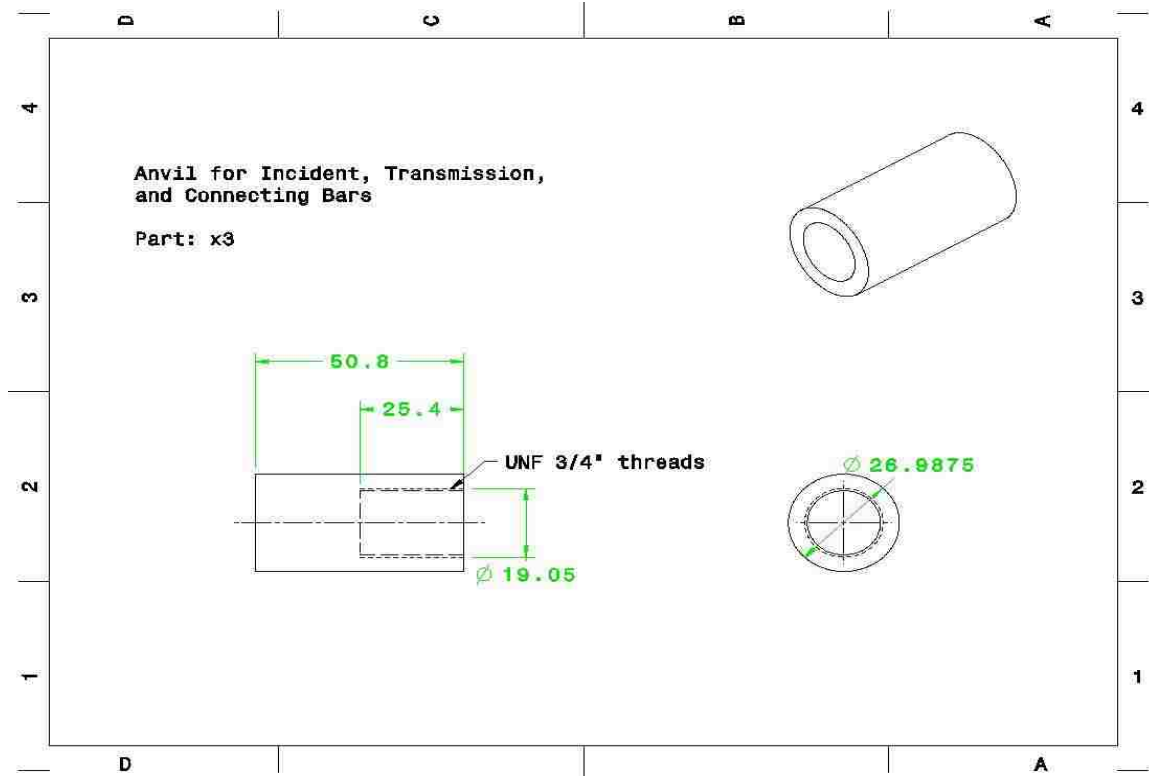
Bar holder (Zanettin, Young, & Hussain, 2012)



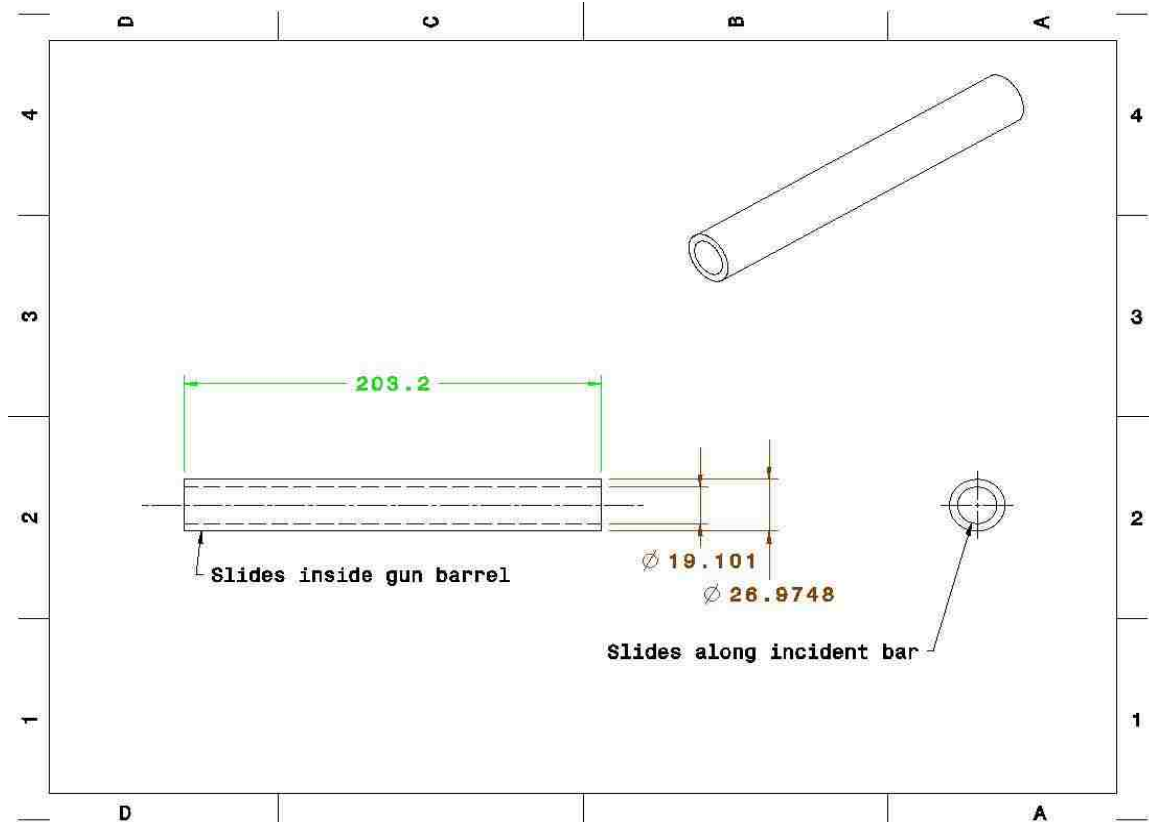
Incident and Transmission Bars



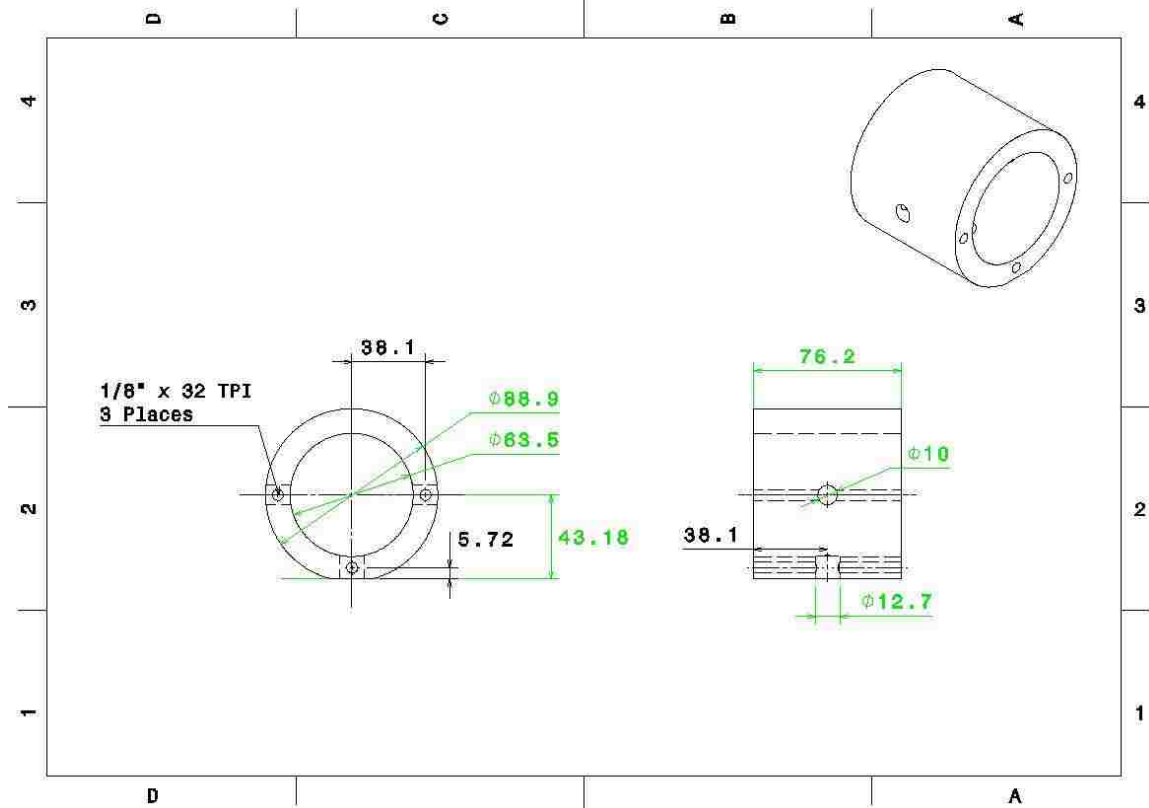
Anvil



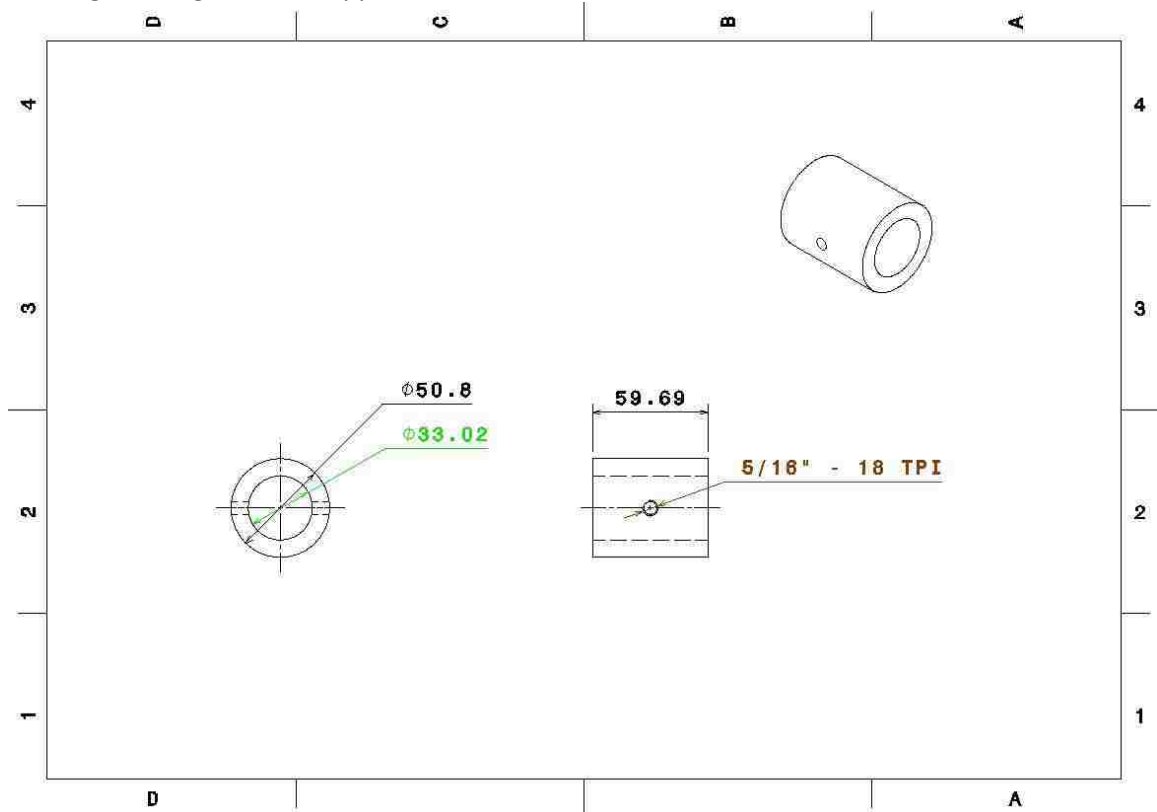
Striker



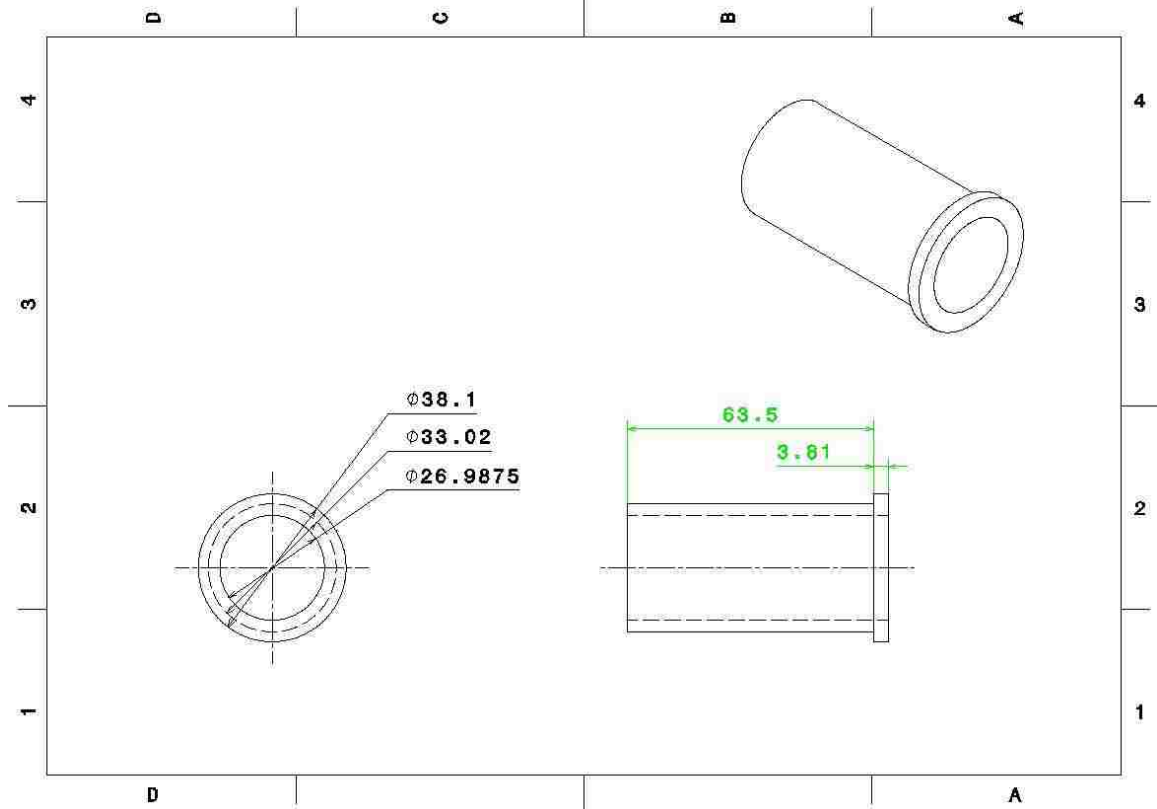
Outer Housing for the anvil support



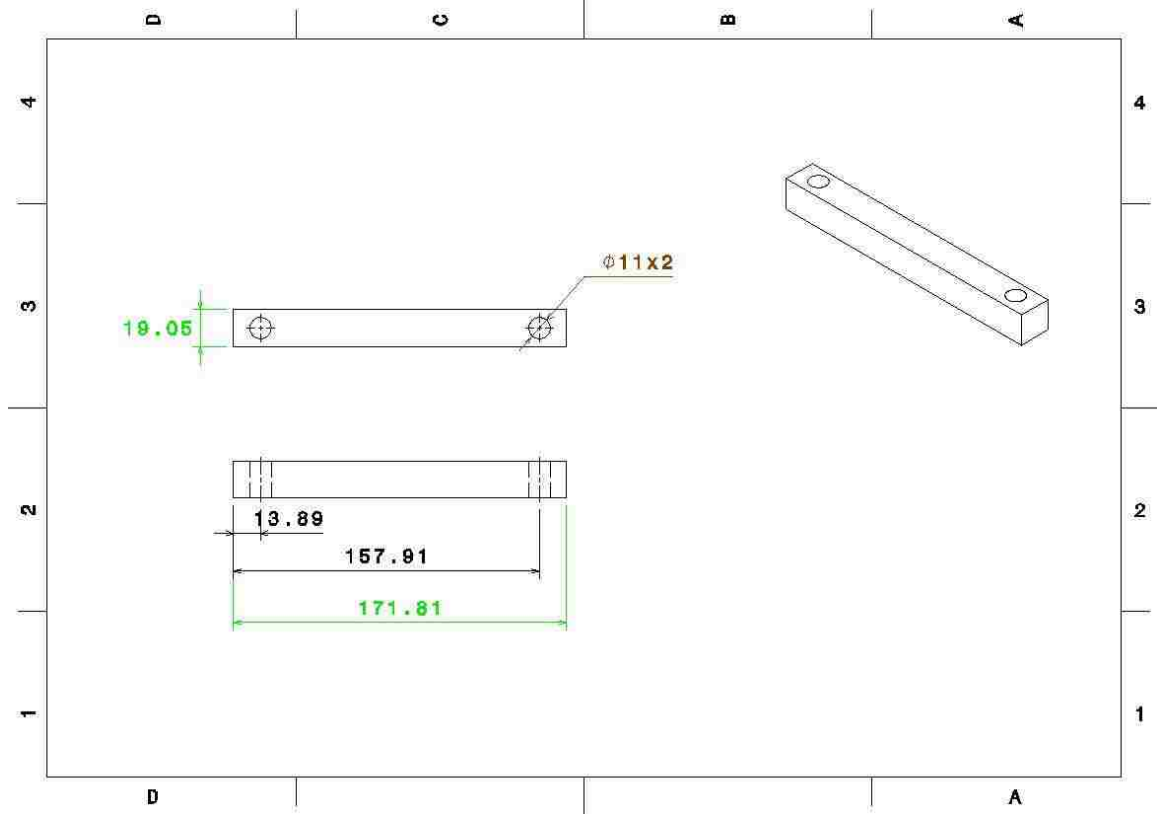
Bushing Housing for anvil support



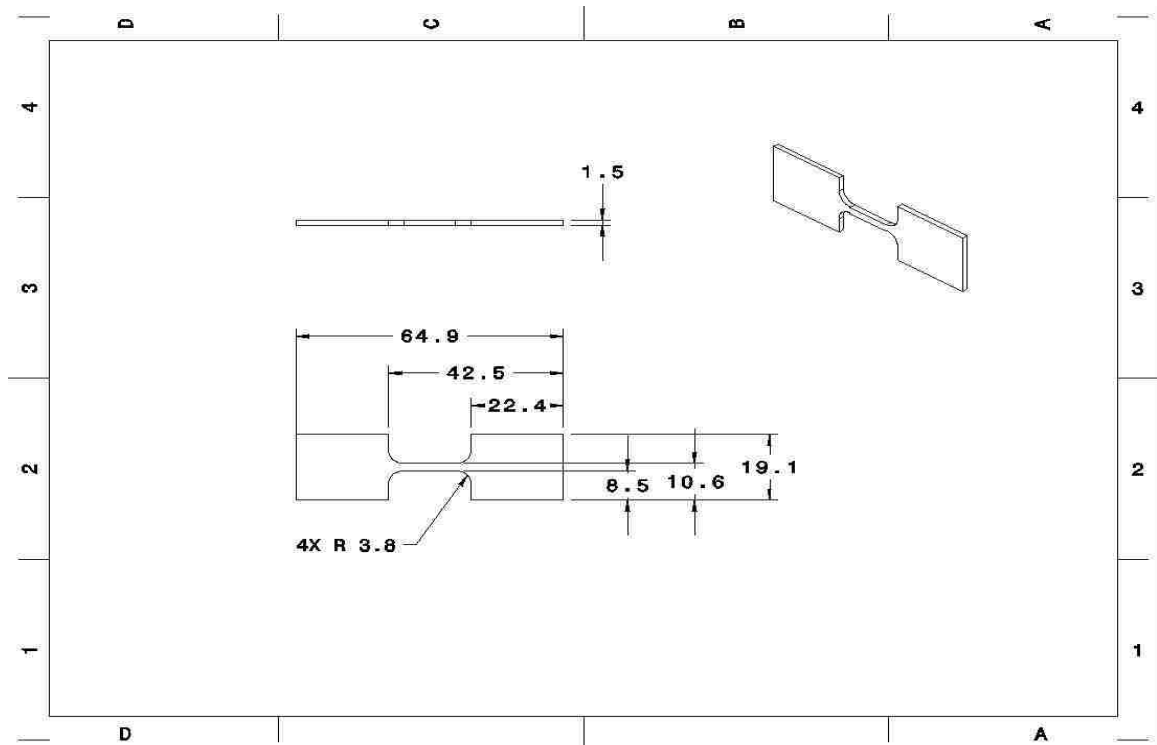
Teflon Bushing for anvil support



Base Clamping Bar



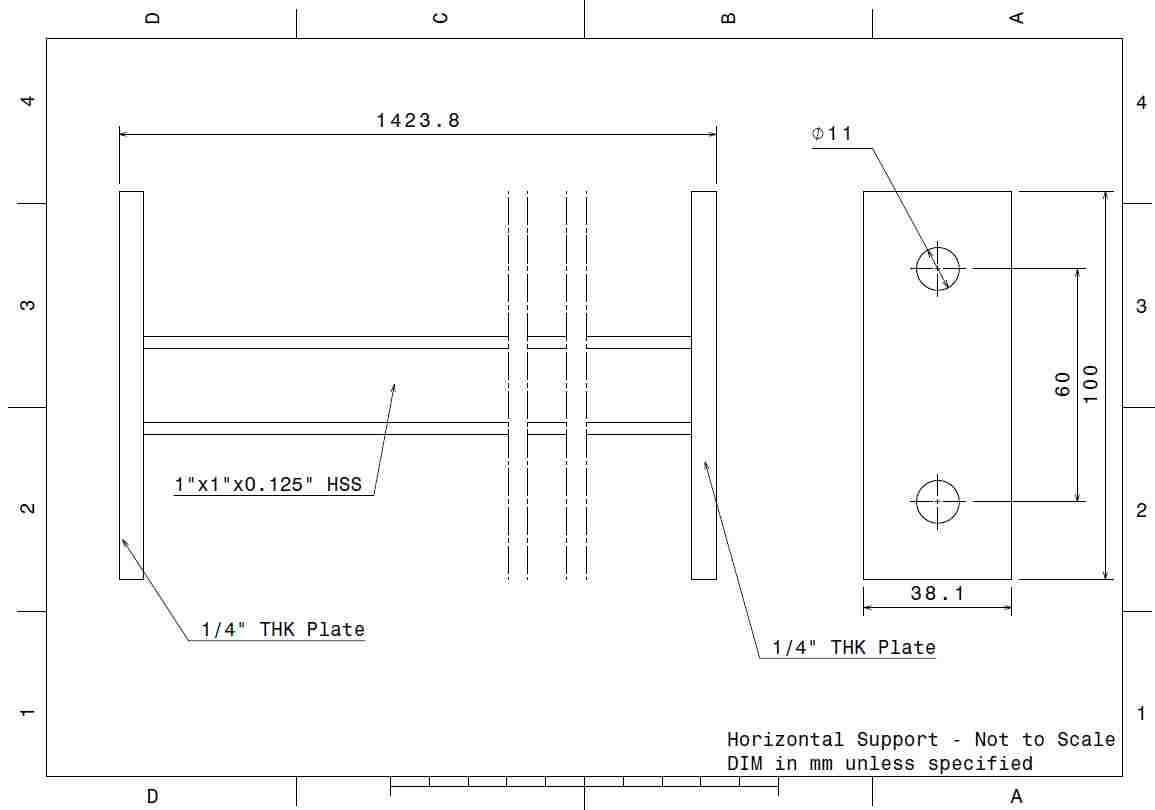
Specimen Drawing



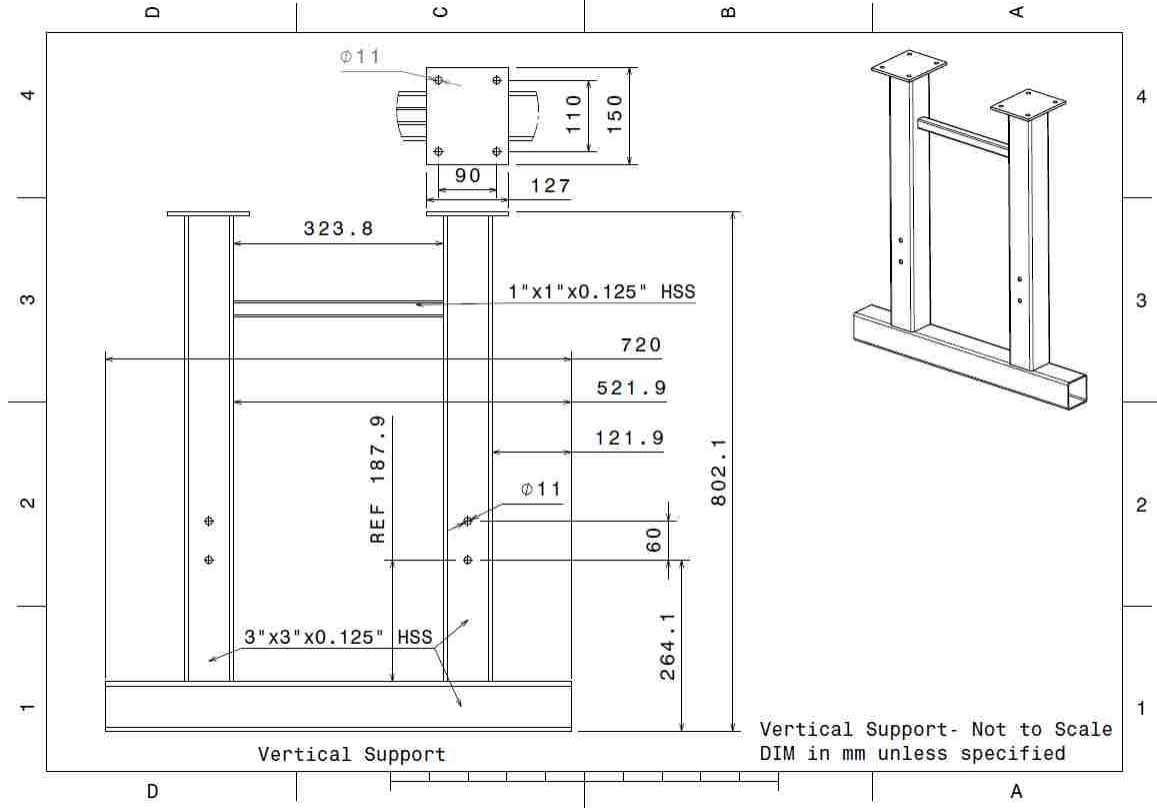
Assembly of the frame consists of:

- I-beam
- Horizontal support
- Vertical support

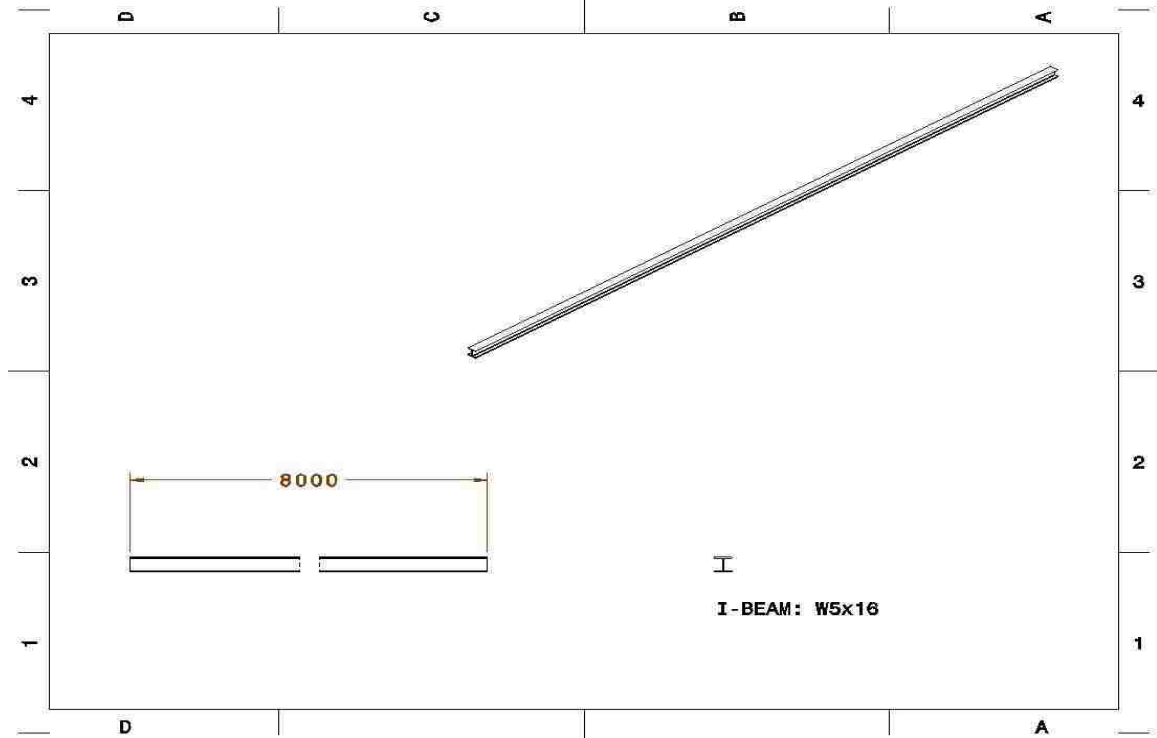
Horizontal support (Zanettin, Young, & Hussain, 2012)



Vertical Support (Zanettin, Young, & Hussain, 2012)



I-beam



Appendix C – MATLAB Data Processing Program

```
% University of Windsor
% Department of Mechanical and Materials Engineering
% SHPB Analysis Version 1.0
% June 2015

% Developed by: Kevin Young

clear all
close all

%


---


% Constant Values:

bar_dia = 19.05/1000;           % the diameter of the incident and
transmission bars (m)

Ro_bar = 7850;                 % Density of the bars (kg/m^3)
E_bar = 205e9;                 % Young's modulus of the bar (Pa)
sr_dig = 10e6;                 % Sample rate of the digitizer

%


---


% Calculated Values:

C_bar = sqrt(E_bar/Ro_bar);    % Elastic wave speed in the bars (m/s)
A_bar = pi*(bar_dia/2)^2;     % Area of bars (m^2)
A_spc = 0.0015*0.0021;       % Area of spceimin (m^2) (sheet
material)

%


---


% Input from Excel

[file_name,PathName] = uigetfile('*.xlsx','Select the Excel file');

data_inc = xlsread([PathName file_name],'B:B'); % Data for the
incident pulse
data_trans = xlsread([PathName file_name],'D:D'); % Data for the
transmitted pulse

x = size(data_inc);
data_points = 1:x; % Number of data
points sampled
```

```

%


---


% Convert voltages to microstrain

inc_pulse_originraw = ((data_inc./106).*2)./(10*2.09);
tra_pulse_originraw = ((data_trans./106).*2)./(10*2.09);

%


---


% Zero incident and transmitted waves

figure(1);
plot(data_points,inc_pulse_originraw);
grid on;

figure(2);
plot(data_points,tra_pulse_originraw);
grid on;

not_done = false;
while(not_done == false)

    offset_inc = input('Enter offset needed to zero the incident
wave:');
    offset_tra = input('Enter offset needed to zero the transmitted
wave:');

    inc_pulse_offset = (inc_pulse_originraw(:)+offset_inc);
    tra_pulse_offset = (tra_pulse_originraw(:)+offset_tra);

    figure(1);
    plot(data_points,inc_pulse_offset);

    figure(2);
    plot(data_points,tra_pulse_offset);

    not_done = input('Are the plots zeroed? true/false:');
end

%


---


% Filtering the incident and transmitted signals

% Initial filter values

Fpass = 250e3; % Passband frequency: Enter in Hz
the cutoff frequency you want
Ford = 2; % Filter order: must be a positive
integer scalar

```

```

not_done = false;
while(not_done == false)

    lpFilt = designfilt('lowpassiir','FilterOrder',Ford, ...
        'PassbandFrequency',Fpass, 'PassbandRipple',0.2, ...
        'SampleRate',sr_dig);

    inc_pulse_origin = filtfilt(lpFilt,inc_pulse_offset);
    tra_pulse_origin = filtfilt(lpFilt,tra_pulse_offset);

    %    figure(3),
    %    fvtool(lpFilt)

    figure(3),
    plot(data_points,inc_pulse_origin);
    grid on;

    figure(4),
    plot(data_points,tra_pulse_origin);
    grid on;

    not_done = input('Happy with the filtered signals? true/false:');

    if(not_done == true)
        break;
    end

    Fpass = input('Enter new passband frequency (in Hz):');
    Ford = input('Enter new filter order (must be a positive integer
scalar):');

end

%


---


% Finding the incident, reflected and transmitted pulse times using
force
% equilibrium

not_done = false;

while(not_done == false)

    beginc=input('please input the sample number that incident pulse
begins:');
    inc_begin=ceil(beginc)+1;
    inc_end=ceil(input('please input the sample number that incident
pulse ends:'))+1;
    ref_begin=ceil(input('please input the sample number that reflected
pulse begins:'))+1;

```

```

tra_begin=ceil(input('please input the sample number that
transmitted pulse begins:'))+1;

n0=inc_end-inc_begin+1;

for i=1:n0;
    t(i,1)=(i-1);
    inc_pulse(i,1)=inc_pulse_origin(inc_begin-1+i);
    ref_pulse(i,1)=inc_pulse_origin(ref_begin-1+i);
    tra_pulse(i,1)=tra_pulse_origin(tra_begin-1+i);

    F_inc(i,1)=(inc_pulse(i,1)+ref_pulse(i,1))*E_bar*A_bar;
    F_tra(i,1)=tra_pulse(i,1)*E_bar*A_bar;
end

figure(5)
plot(t,inc_pulse,'r'),hold on;
plot(t,-ref_pulse,'g'),hold on;
plot(t,tra_pulse,'b'),hold on;
axis tight;grid on;
title('Pulses zoom in','FontName','Cambria','FontSize',12);
xlabel('Sample Number','FontName','Cambria','FontSize',12);
ylabel('strain(\mu\epsilon)','FontName','Cambria','FontSize',12);
hold off;

figure(6)
plot(t,F_inc,'r.'),hold on;
plot(t,F_tra,'b'),hold on;
axis tight; grid on;
title('Force applied on the
specimen','FontName','Cambria','FontSize',12);
xlabel('Sample Number','FontName','Cambria','FontSize',12);
ylabel('Force(N)','FontName','Cambria','FontSize',12);
hold off;

not_done = input('Happy with force equilibrium? true/false:');

end

%


---


% Convert microstrain to strain

inc_pulse_strain = inc_pulse_origin./1e6;
tra_pulse_strain = tra_pulse_origin./1e6;

%


---


% Calculating the stress-strain curve's

for i=1:n0
    k1 = ref_begin + i -1;

```

```

k2 = tra_begin + i -1;
k3 = inc_begin + i -1;

ref_data(i,1) = inc_pulse_strain(k1);
ref_area(i,1) = trapz(ref_data);

trans_data(i,1) = tra_pulse_strain(k2);
trans_area(i,1) = trapz(trans_data);

inc_data(i,1) = inc_pulse_strain(k3);
inc_area(i,1) = trapz(inc_data);

end

for i=1:n0
    eng_strain(i,1) = -2*(C_bar/0.015)*ref_area(i,1);
    eng_stress(i,1) = E_bar*(A_bar/A_spc)*trans_data(i,1);

    eng_strain2(i,1) = (C_bar/0.015)*(inc_area(i,1)-ref_area(i,1)-
trans_area(i,1));
    eng_stress2(i,1) =
E_bar*((A_bar)/(2*A_spc))*(inc_data(i,1)+ref_data(i,1)+trans_data(i,1))
;

    true_strain(i,1) = log(1+eng_strain2(i,1)/10);
    true_stress(i,1) = eng_stress(i,1)*(1+eng_strain2(i,1)/10);

    strain_rate(i,1) = (C_bar/0.015)*(inc_data(i,1)-ref_data(i,1)-
trans_data(i,1));
    time(i,1) = t(i,1)/sr_dig;

end

figure(7)
plot(eng_strain/10,eng_stress);
hold on;
plot(eng_strain2/10,eng_stress, 'r');
title('Engineering Stress-Strain
Curve','FontName','Cambria','FontSize',12)
xlabel('Strain (mm/mm)','FontName','Cambria','FontSize',12)
ylabel('Stress (MPa)','FontName','Cambria','FontSize',12)
legend('Uniform strain','Average strain','Location','southeast')
grid on;

figure(8)
plot(true_strain,true_stress);
hold on;
plot(eng_strain2/10,eng_stress, 'r');
title('True Stress-Strain Curve','FontName','Cambria','FontSize',12)
xlabel('Strain (mm/mm)','FontName','Cambria','FontSize',12)
ylabel('Stress (MPa)','FontName','Cambria','FontSize',12)
legend('True stress-strain','engineering stress-
strain','Location','southeast')
grid on;

```

```

figure(9)
plot(time, strain_rate*1e6);
title('Strain Rate vs. Time', 'FontName', 'Cambria', 'FontSize', 12)
xlabel('Time (s)', 'FontName', 'Cambria', 'FontSize', 12)
ylabel('Strain Rate (1/s)', 'FontName', 'Cambria', 'FontSize', 12)
grid on;

figure(10)
plot(time, true_strain);
xlabel('Time (\mus)', 'FontName', 'Cambria', 'FontSize', 12)
ylabel('True Strain (%)', 'FontName', 'Cambria', 'FontSize', 12)
grid on;
click = 1;
while(click ~= 3)

    [x1,y1] = ginput(1);
    [x2,y2] = ginput(1);

    strainrate = (y2 - y1)/((x2 - x1))

    title('Press right mouse button to continue, any other to
redo', 'FontName', 'Cambria', 'FontSize', 12)
    [junkx,junky,click]=ginput(1);

end

not_done = false;

while(not_done == false)

    not_done = input('Do you want to save data? true/false:');

    if (not_done == false)
        break;
    end

    [FileName,PathName] = uinputfile({'*.xlsx'});

    xlswrite([PathName,FileName], {'eng strain'}, 1, 'A1');
    xlswrite([PathName,FileName], eng_strain, 1, 'A2');
    xlswrite([PathName,FileName], {'eng stress'}, 1, 'B1');
    xlswrite([PathName,FileName], eng_stress, 1, 'B2');
    xlswrite([PathName,FileName], {'true strain'}, 2, 'A1');
    xlswrite([PathName,FileName], true_strain, 2, 'A2');
    xlswrite([PathName,FileName], {'true stress'}, 2, 'B1');
    xlswrite([PathName,FileName], true_stress, 2, 'B2');
    xlswrite([PathName,FileName], {'strainrate'}, 2, 'C1');
    xlswrite([PathName,FileName], strainrate, 2, 'C2');
end

```

Vita Auctoris

NAME: Kevin Young

PLACE OF BIRTH: North Vancouver, B.C.

YEAR OF BIRTH: 1978

EDUCATION: Lord Tweedsmuir Senior Secondary, Surrey, B.C., 1996

BCIT, Dipl. Tech., Burnaby, B.C., 2000

University of Windsor, B.Sc., Windsor, ON, 2012

University of Windsor, M.A.Sc., Windsor, ON, 2015